ROLE OF CONDUCTIVITY SPATIAL STRUCTURE
IN DETERMINING THE LOCATIONS OF SPRITE INITIATION

A

DISSERTATION

Presented to the Faculty

of the University of Alaska Fairbanks

in Partial Fulfillment of the Requirements

for the Degree of

DOCTOR OF PHILOSOPHY

By

Fernanda de São Sabbas Tavares, M.S., B.S.

Fairbanks, Alaska

May 2003

UMI Number: 3092296

UMI®

UMI Microform 3092296
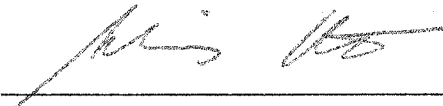
ROLE OF CONDUCTIVITY SPATIAL STRUCTURE

IN DETERMINING THE LOCATIONS OF SPRITE INITIATION

By

Fernanda de São Sabbas Tavares

RECOMMENDED:

_____

_____

_____

_____
Advisory Committee Chair

_____
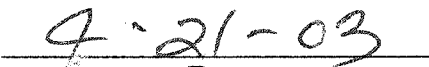Chair, Physics Department

APPROVED: _____
Dean, College of Science, Engineering and Mathematics

_____
Dean of Graduate School

_____
Date

ABSTRACT

Sprites are transient optical signatures of mesospheric electrical breakdown in response to lightning discharges. Multiple sprites are often observed to occur simultaneously, laterally displaced from the underlying causative cloud-to-ground (CG) lightning discharge. The causes of this lateral displacement are presently not understood. This dissertation investigates the role of neutral density perturbations in determining the locations of sprite initiation. The work was performed in three interrelated studies. (1) A detailed statistical study of the temporal-spatial relationships between sprites and the associated CG was performed for July 22, 1996. The distribution of sprite offsets relative to the underlying lightning had a mean of ~40 km. The distribution of sprite onset delays following the parent lightning had a mean of ~20-30 ms, consistent with theoretical estimates for the electron avalanche-to-streamer transition in the mesosphere. (2) A follow-up study for the same observations was performed to investigate the relationship of the sprites to convective activity in the underlying thunderstorm, using GOES-8 infrared imagery of cloud-top temperatures. The sprite generating thunderstorm was a Mesoscale Convective System (MCS). The maximum sprite and –CG production of the system were simultaneously reached at the time of maximum contiguous cloud cover of the coldest region, corresponding to the period of greatest convective activity of the system. Thunderstorm convective activity is a potential source of gravity waves and mesospheric turbulence. (3) Computer simulations of the temporal-spatial evolution of lightning-induced electric fields in a turbulent upper atmosphere were performed. The modeled turbulence in the simulations spanned the amplitude range 10% to 40% of the ambient background neutral density, with characteristic scale sizes of 2 km and 5 km, respectively. The results indicate that neutral density spatial structure, similar to observed turbulence in the mesosphere, facilitates electrical breakdown in isolated regions of density depletions at sprite initiation altitudes. These spatially distributed breakdown regions provide the seed electrons necessary for sprite generation, and may account for the observed sprite offsets.

DEDICATION

I dedicate this work to my family.

TABLE OF CONTENTS

LIST OF FIGURES

LIST OF TABLES

LIST OF APPENDICES

ACKNOWLEDGEMENTS

First of all I thank God for my existence, and for all He has been giving me throughout it.

I thank all my spiritual friends; they have been supporting my every single step!

I thank my parents for providing me with this wonderful tool, my body, which allows me to learn, to express and educate myself, during my experiences in this material world. I also thank them for giving me an excellent education with noble and strong principles.

Thanks to my advisor, who accepted the challenge of guiding me through this Ph.D. journey.

I am very grateful to all my wonderful friends spread throughout the world, for their wonderful support, always. Special thanks to the friends I met here in Fairbanks. Their presence brought sunshine to the difficult dark winter days, and provided dear opportunities to share my every joy. I hope I have given them at least a small part of the happiness they have given me.

Thanks to all fellow scientists who directly or indirectly contributed to the work developed. Special thanks to my committee members, Gene Wescott, Hans Nielsen and Mike Taylor.

I would like to thank the co-authors of the paper that forms Chapter 2, "Statistical analysis of space-time relationships between sprites and lightning" published in the *Journal of Atmospheric and Solar-Terrestrial Physics* [*São Sabbas et al.*, 2003a]. The contributions of the co-authors of this paper were as follows: Davis D. Sentman helped interpret the results and provided suggestions/corrections to the manuscript. Eugene M. Wescott provided useful guidance about the usage of the sprite triangulation software developed by Hans Stenbaek-Nielsen, and helpful discussions in the interpretation of the results. Osmar Pinto Jr. and Odim Mendes Jr. provided useful guidance regarding the treatment of the lightning data. Michael J. Taylor provided sprite images from a different

ground site used in the triangulation, and useful discussions in the interpretation of the results.

I would like to thank the co-author of the paper that forms Chapter 3, "Dynamical relationship of infrared cloudtop temperatures with occurrence rates of cloud-to-ground lightning and sprites" published in the *Geophysical Research Letters* [*São Sabbas et al.*, 2003b], Davis D. Sentman. He contributed by helping to write the computer programs used in manipulation of GOES images, by assisting with the data analysis, by helping to interpret the results, and by providing suggestions/corrections in the preparation of the manuscript.

I would like to thank CNPq, a Brazilian government agency dedicated to scientific and technological development, the U.S. Air Force, NASA, and the Geophysical Institute for their support.

"Returning from the empty grave, Jesus said to the frightened disciples: 'It is me, do not fear.' … 'Be encourage: I overcame the world!' Let us meditate, and, without fear, let us advance constructing with love so that love will respond to our sowing of hope, with a blossom of the peace and the happiness to the benefit of all."

Joanna de Ângelis

CHAPTER 1

INTRODUCTION

The mechanisms by which energy and momentum originating in solar processes are transferred downwards into and distributed within the Earth's Mesosphere-Thermosphere-Ionosphere (MTI) region, have been the subjects of studies over many decades and are relatively well understood. Beginning in the early 1980s, sources involving upward transfer and dissipation of mechanical energy from the neutral lower atmosphere into the MTI region were identified, in the form of atmospheric gravity waves. This form of energy input into the MTI region signaled that understanding the properties of near-earth space requires taking into account inputs from both above and below.

Recently, an additional form of energy input into the MTI region from below was discovered. This new electrical component was discovered by *Franz et al.* [1990] in low-light video images of lightning induced transient optical emissions of large scale in the middle/upper atmosphere above a thunderstorm in the central US. After it was determined that the emissions extended all the way to the ionosphere [*Sentman et al.*, 1995a,b], the events acquired the mechanism-neutral name of "sprites" (Figure 1.1).
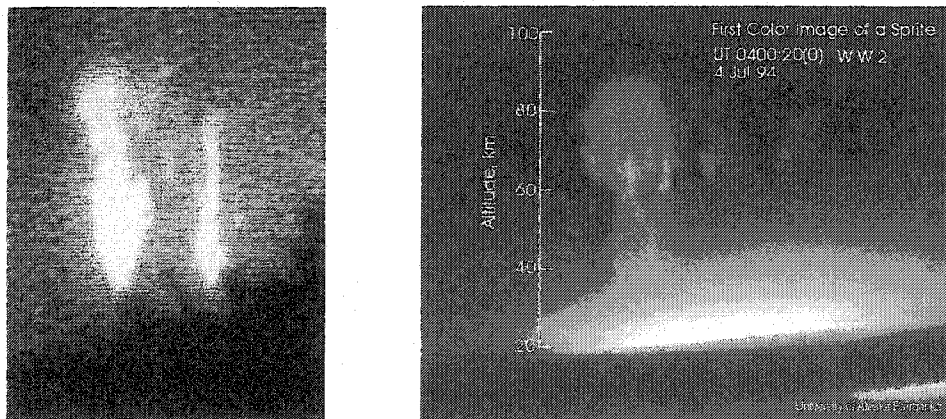
Figure 1.1 Sprites. On the left, first image of a sprite [*Franz et al.*, 1990]. On the right, first true color image of a sprite [*Sentman et al.*, 1995a].

1.1 SPRITE MORPHOLOGY

Sprites are predominantly red in color and the dominant emissions (Figure 1.2) are found to be from the first positive bands of N_2 [*Mende et al.*, 1995; *Hampton at al.*, 1996; *Heavner*, 2000a,b]. Evidence for ionization has been reported in the form of weak red N_2^+ Meinel emissions [*Bucsela et al.*, 1998; *Morrill et al.*, 1998] and transient blue N_2^+ 1NG emissions [*Armstrong et al.*, 1998; *Suszcynsky et al.*, 1998; *Takahashi et al.*, 1998; *Armstrong et al.*, 2000]. They are primarily associated with positive cloud-to-ground (+CG) lightning strokes [*Boccippio et al.*, 1995; *Lyons*, 1996; *São Sabbas et al.*, 2003a] and the most intense events possess a distinctive ELF-VLF radio signature [*Inan et al.*, 1995, 1996; *Dowden et al.*, 1996; *Reising et al.*, 1996]. The duration of a sprite can vary from a few milliseconds to a few hundred milliseconds. They were initially reported to reach terminal altitudes of ~35 km [*Franz et al.*, 1990], but subsequent dual-aircraft measurements revealed they extend from 40-90 km altitude and possess lateral dimensions of 5-30 km [*Sentman at al.*, 1995a,b]. More recent observations have shown that some sprites appear to extend down to the top of the clouds [*Siefring et al.*, 1999; *Pasko et al.*, 2002], and that their horizontal extent within the mesosphere ranges from ~10 m, for the small column sprites and fine structure within sprites [*Gerken et al.*, 2000], to ~40 km for fully developed single sprites [*Stenbaek-Nielsen et al.*, 2000], and a few hundred of km for sprite clusters.
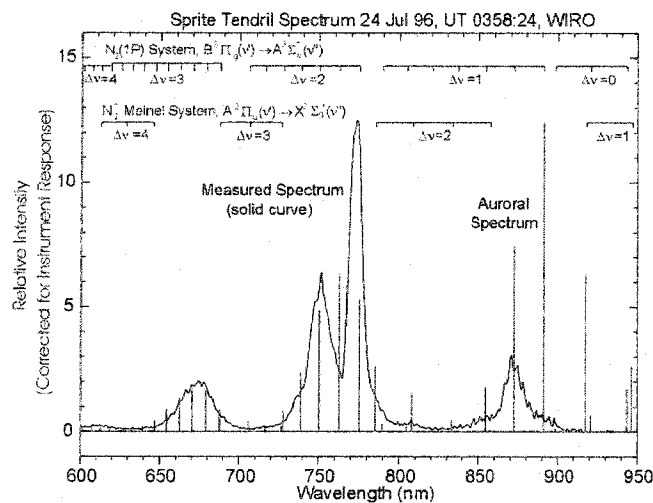
Figure 1.2 Sprite and aurora spectrum between 600 e 900 nm [*Hampton et al.*, 2000].

Following the *Franz et al.* [1990] discovery, other investigations quickly revealed that sprites are only one of a diverse set of lightning driven optical transients above thunderstorms. Other types of optical transients (Figure 1.3) that exhibit different structural properties and dynamical behavior include Blue Jets and Blue Starters [*Wescott et al.*, 1995a, 1996, 1998a], Elves, which are sub-ms optical enhancements of the ionosphere at an altitude of ~100 km [*Inan et al.*, 1997], Halos, which are disk shaped optical emission believed to be produced by the same physical process that generates sprites [*Barrington-Leigh et al.*, 2001; *Wescott et al.*, 2001], and various subspecies of these genres.
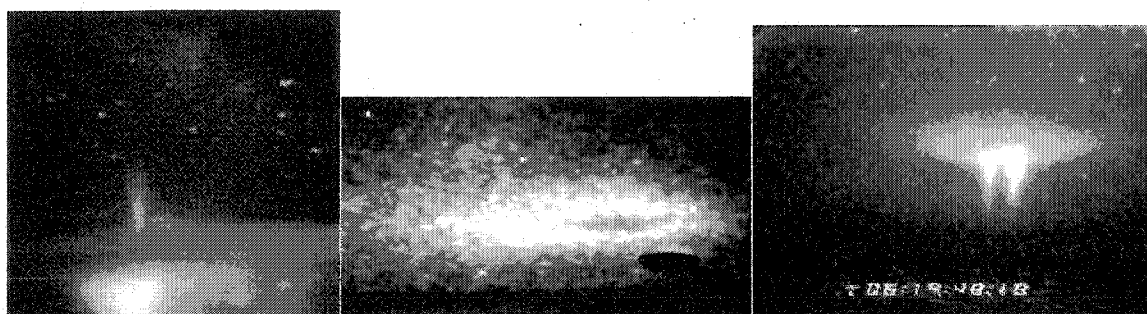
Figure 1.3 Blue jet (left), elve (center), sprite-halo (right). The blue jet was observed over central US during Sprites94 airplane campaign by UAF. The elve was observed by USU over the south of Balkans during the NASA Leonid-99 campaign. The sprite-halo was recorded over central US during the Sprites99 ground campaign by UAF.

In their totality, these events span the full vertical extent of the atmosphere from the tropopause (~18 km) to the base of the ionosphere (~100 km). Figure 1.4 illustrates, in correct vertical scale, the variety of optical transients that have been reported above thunderstorms. Sprites are by far the brightest, most spectacular, most common and most important of these phenomena for energy transfer processes, and this work focuses on them.
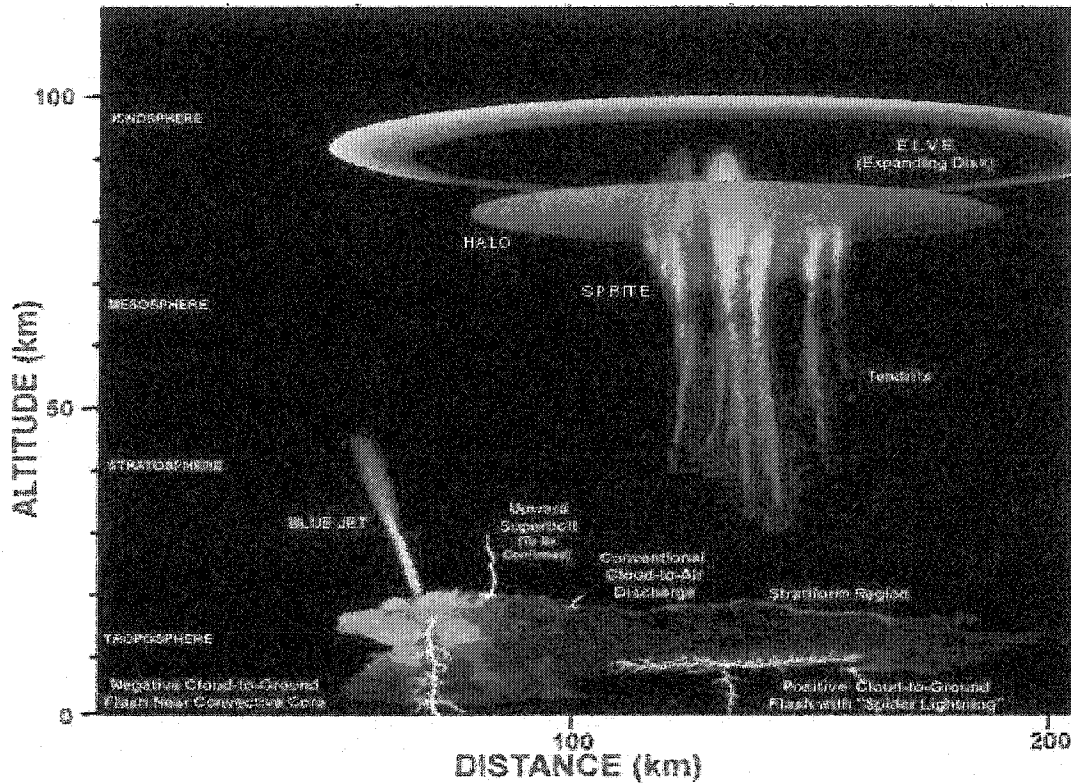
Figure 1.4 Lightning excited optical emissions in the upper atmosphere. Sprites and their associated tendrils, along with the closely related halos, are the brightest and most commonly observed of these transient structures. The other events generally do not occur in association with each other, and are shown together here to provide relative scale. (Adapted from *Lyons* [2000])

1.2 POSSIBLE IMPACT IN THE MTI SYSTEM

All lightning discharges deposit a certain amount of electrical energy into the MTI, which may be larger or smaller depending on the amount of charge they extinguish in the thunderstorm and on the duration and shape of the electric current of the discharge. Both electromagnetic radiation of the lightning currents and the quasi-electrostatic component of the field, generated by the charge extinction, are transmitted to the upper atmosphere, where they accelerate ambient free electrons. In this highly collisional medium, the accelerated electrons interact with the neutral atmosphere, predominantely composed of molecular nitrogen and oxygen, in a variety of ways. Elastic scattering is the dominant interaction leading to electron heating. For energies greater than excitational energies of its neutral collision partner, the scattering may be inelastic. At progressively

larger electron energies, rotational, vibrational, and electronic energy states may be excited in the neutral species, molecules may be dissociated, and if the electron energy exceeds the ionization potential of the neutral, ionization may occur. Optical emissions, the observable output of these complex interactions, are produced when the radiative lifetime of the excited or ionized states is shorter than the de-excitation time (quenching) by collisions or chemical interactions.

Photometric measurements of large sprites have determined that the optical energy in the flash may be as large as 50 kJ, but the optical component of such a discharge represents only a small fraction (<1%) of the total energy [*Heavner*, 2000a,b]. Gas discharge physics developed since the 1930s and subsequent kinetic models show that a substantial amount of energy is also deposited in excited electronic or nonradiating rotational and vibrational states of N_2 and O_2 [e.g., *Raizer*, 1991]. *Heavner* [2000a,b] has estimated that the total energy deposited in the mesosphere by a large sprite may be as large as 1 GJ, but this has been recently revised downward to 1-10 MJ [*Sentman et al.*, 2003]. Calculations of the Joule heating of neutrals associated with such large events indicate the overall effects are quite small (~0.02K), so that direct thermal effects on the neutral chemistry are expected to be marginal.

Vibrationally and electronically activated molecular states possess great potential to launch reaction chains or catalytic cycles by interaction with minor species that would not otherwise occur in the quiescent nighttime mesosphere. For example, in a model study involving several dozen atmospheric species, *Sentman et al.* [2000] reported estimated density enhancements by several orders of magnitude occur at 70 km in both negative ions CO_3^- and CO_4^- and hydrated positive ions $H^+(H_2O)_3$ and $H^+(H_2O)_2$ following a single sprite-producing lightning stroke. The effects are local and transient, persisting from 10s-1000s seconds. However, with an active thunderstorm producing several lightning discharges per second over several hours, the enhancements would be substantially greater. A related effect showing significant enhancements of NO, an important catalyst for ozone destruction, at altitudes 60-80 km above thunderstorms, was reported for both simulations and UARS HALOE observations by *Armstrong* [2001]

(Figure 1.5). In both studies, the principal activated species driving the electrochemical reactions are the electron impact-excited neutral $N_2(A^3\Sigma_u^+)$ and $O_2(a^1\Delta_g)$ electronic states.

Although most sprite measurements have been performed in the Midwest (central plains region) of the U.S., sprites are global phenomena. The global aspect of sprites was first identified in studies of video tapes from the Mesoscale Lightning Experiment (MLE) performed from the space shuttle [*Boeck et al.*, 1992]. Between 1989 and 1991, 17 sprites were recorded above thunderstorms distributed over Australia, Africa, South Pacific and South America. Aircraft observations over Central and South America [*Sentman et al.*, 1995c; *Wescott et al.*, 1995b], ground campaigns in Japan [*Fukunishi et al.*, 1999, 2001] Australia [*Dowden et al.*, 1996], more recent aircraft [*Taylor et al.*, 2000] and ground-based observations [*Neubert et al.*, 2001] over Europe, over Asia [*Su et al.*, 2002] and over Central America [*Pasko et al.*, 2002] have generally confirmed these results.
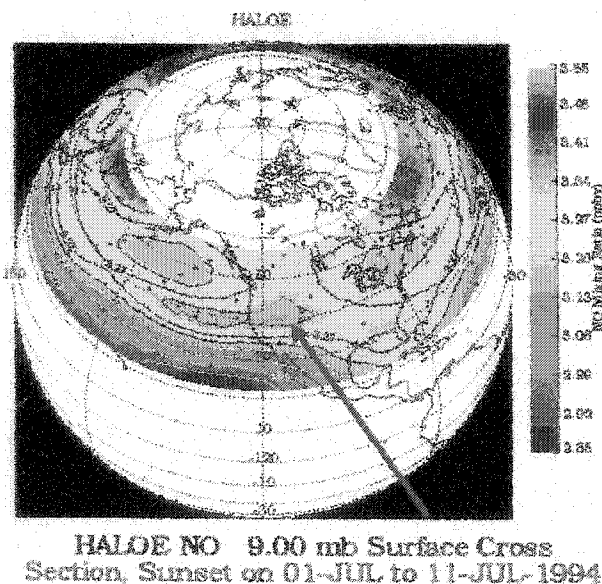
Figure 1.5 HALOE data. The figure shows a westward plume of NO at ~35 km (Courtesy, *Armstrong* [2001]).

1.3 CURRENT THEORIES

Observations of sprites provide possible opportunities to indirectly determine the associated electrical energy transferred from thunderstorms into the mesosphere. The principal energy transfer mechanism is believed to be the local acceleration of ambient electrons by large transient electric and electromagnetic fields associated with cloud-to-ground lightning. There are several current sprite theories: (1) Lightning-induced quasi-electrostatic heating of the neutral atmosphere [*Pasko et al.*, 1995, 1996, 1997b]; (2) Runaway electrons of MeV energies [*Bell et al.*, 1995; *Roussel-Dupré and Gurevich*, 1996; *Taranenko and Roussel-Dupré*, 1996; *Yukhimuk et al.*, 1998]; and (3) Lightning Electromagnetic Pulse (EMP)-induced breakdown [*Rowland et al.*, 1995; *Milikh et al.*, 1995; *Fernsler and Rowland*, 1996; *Rowland et al.*, 1996; *Cho and Rycroft*, 1998, 2001]. Recent models have incorporated key elements of these theories into a more general description constructed around mesospheric plasma streamers as a key element in the generation of sprites [*Pasko et al.*, 1998; *Raizer et al.*, 1998].

The streamer theory is based on the concept of the growth of a thin ionized channel (streamer) between electrodes; the streamer follows the positively charged trail left by the primary intensive avalanche. Electrons of numerous intensive avalanches are pulled into the trail by the field. These avalanches are created by new electrons created by photons close to this trail. Photons are emitted by atoms that the primary and secondary avalanche have excited [*Raizer*, 1991]. The streamer model (Figure 1.6) accounts for many sprite properties, including the elementary columnar form of the simplest structures termed "c-sprite" [*Wescott et al.*, 1998b], sprite ignition at ~75 km [*Stanley et al.*, 1999; *Stenbaek-Nielsen et al.*, 2000], the downward evolution and speed of development [*Stanley et al.*, 1999; *Stenbaek-Nielsen et al.*, 2000; *Moudry*, 2003], the estimated magnitude of the current (~20 A) flowing within the streamer column [*Cummer and Inan*, 1997], inferred channel electron densities of 10^5 cm^{-3} [*Dowden et al.*, 1996; *Groves et al.*, 1996 give an upper limit of 10^3-10^5 cm^{-3}], transverse thicknesses of ~50 m at 80 km and 10 m at 50 km [*Gerken et al.*, 2000], and ~100 ms duration of ionization in streamer columns evidenced by column reactivation [*Gerken et al.*, 2000; *Moudry et al.*, 2001].

Mesospheric Streamer (C-Sprite)

Halo

z~75 km   Ionization Patch   (Activated N₂, O₂ → Chemistry)

60 m

E₀~50 V/m   Plasma
N_e~10⁵

I~20 A   Streamer
τ~100 ms
(Activated N₂, O₂
→ Chemistry)

10 m   Streamer tip
V~10⁷ m/s   Electron Impact
Ionization

z~50 km   E   hν Upstream
~250 V/m   Photoionization
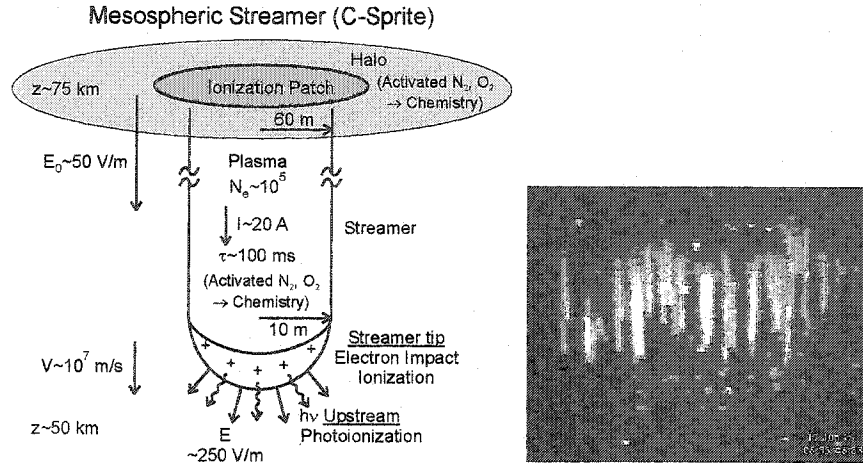
Figure 1.6

Most sprite models using a laminar atmospheric pressure and conductivity profile predict that sprites will occur directly above the lightning discharge where the electric field is strongest. In contrast to the predictions of these models, most sprites are observed to be laterally displaced from the underlying lightning source by several tens km [*Wescott et al.*, 1998b, 2001; *São Sabbas et al.*, 2003a]. Several alternative mechanisms have been previously proposed to account for the observed offset of sprites relative to the underlying lightning.

Valdivia et al. [1997] attributed the offsets and multiple ignition sites to spatial structure in the lightning electromagnetic field, using a fractal model for intracloud lightning as the source. The resultant radiation fields were spatially complex and produced multiple breakdown locations in a simple laminar mesospheric medium. However, high-speed (1000 fps) imaging observations of sprites [*Stenbaek-Nielsen et al.*, 2000] show that they originate as one or more isolated, individual streamers (Figure 1.7) that may emerge from a smooth background of weak optical emissions [*Moudry*, 2003]. The smooth background emissions are interpreted to be electron impact excited N2 1PG and cannot be accounted for by the *Valdivia et al.* [1997] model.
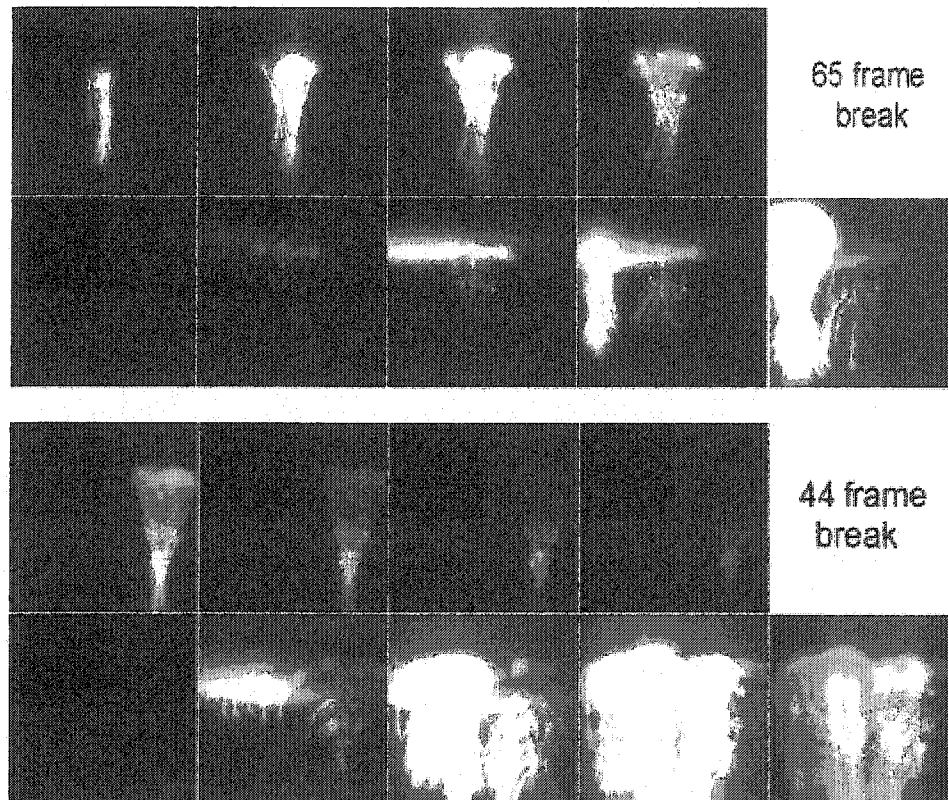
Figure 1.7 High-speed (1000 fps) sequences of sprites [*Stenbaek-Nielsen et al.*, 2000].

Rowland et al. [1996] proposed that the generation of multiple breakdown ionization regions above a lightning discharge could be due to the interaction of lightning electromagnetic fields with gravity waves in the mesosphere. They modeled the interaction of electromagnetic pultses generated by horizontal and vertical lightning discharges with a horizontal sine wave variation in the neutral density, attributing the spatial variations found in the ionization to its sensitivity to the neutral density. Likewise, *Pasko et al.* [1997a] proposed that gravity waves launched by a large area MCC can lead to modulation of the mesospheric neutral density of the order of tens of percent. cylindrically shaped in the vertical direction, similar to those associated with sprites. They further suggested that the several hour delay generally observed between the onset of a thunderstorm and sprites may be a consequence of the time for the gravity wave travel to the mesosphere, such that the appearance of sprites and their spatial structure may be related to gravity waves. One of the implications of the *Pasko et al.* [1997a]

results is that only large MCCs can produce mesospheric density modifications large enough to facilitate the production of sprites, whereas recent observations reveal that prolific sprite activity may occur above smaller thunderstorms [*Moudry et al.*, 1997; *Fukunish et al.*, 1999; *Neubert et al.*, 2000; *Taylor et al.*, 2000; *Su et al.*, 2002].

Meteor effects on the upper atmosphere have also been proposed to account for the offsets. *Symbalisty et al.* [2000] and *Wescott et al.* [2001] proposed that micro-meteor influxes could create an ionization/dust trail which, when exposed to the transient electric fields of a lightning discharge, could initiate a sprite. *Zabotin and Wright* [2001] further provide a detailed discussion of electrostatic field amplification and corona breakdown from microspires on dust surfaces in meteor trails.

The effects described above may be classified as being of two different types: (1) Perturbations in the dielectric due to effects in gas dynamical parameters, such as local neutral, ion and electron density perturbations, as well as temperature perturbations, with consequent focusing and enhancement of the electric field in the inhomogeneous conductivity background. (2) Effects of particulates such as micro-meteors, and dust or ice particles in general, where corona sites on microspires may provide seed electrons to initiate sprites. In principle, both types of effects might occur. It is presently unknown which of these two classes of effects is the more important.

1.4 SCOPE OF DISSERTATION

Sprites are the optically observable component of air electric breakdown in the mesospheric region of the atmosphere due to electric fields generated by underlying lightning discharges. Specifying the mechanisms by which the breakdown occurs requires a description of the lightning radiation and electrostatic fields, and the interaction of these fields with the dielectric of the upper atmosphere. The simultaneous appearance of spatially distributed, multiple breakdown sites suggests the presence of spatial structure in this region or/and in the electromagnetic/electrostatic fields that interact with the mesosphere. Models of both kinds have previously been proposed.

The conditions that determine the specific locations where sprite ignition occurs may depend on several interrelated factors. These include the nature of the underlying lightning discharge, i.e., if it is a CG or intracloud, the existence of spatial structure and its characteristics in the medium where breakdown occurs, and whether the lightning and mesospheric inhomogeneities share a common source, e.g., the underlying thunderstorm.

In this thesis, interrelationships among lightning, convective storm dynamics, conductivity inhomogeneities in the mesosphere and sprites were investigated to help clarify the respective roles they play determining the locations of sprite ignition. The principal goals of the thesis were: (1) To determine the spatial and temporal relationships between sprites and lightning. (2) To characterize the convective activity associated with sprite producing lightning based on infrared satellite images of the associated thunderstorm. (3) To investigate the role played by conductivity inhomogeneities in the mesosphere/lower ionosphere in determining specific locations where electric breakdown, which may lead to sprite ignition, occurs.

The dissertation is organized in five chapters. Chapter 1 is the Introduction. Chapter 2 presents results of a detailed statistical analysis of the temporal and spatial association of sprites with lightning. In this chapter the distribution of the extent of spatial displacement of sprites from their parent lightning is documented. Both temporal and spatial criteria were used for the first time to select the parent +CG in a statistical study of this type. The distribution of time intervals between sprites and parent +CGs with a peak between 10-20 ms, presented in this chapter, may characterize the time scale for the development of an individual electron avalanche into a streamer between ~70-85 km altitude. The distribution of the distance between sprites and parent +CGs suggests that the characteristics of the local mesosphere, such as inhomogeneous conductivity, may play a significant role in determining where and how many sprites occur in association with a lightning discharge. These and other results of this study are published in the *Journal of Atmospherics and Solar Terrestrial Physics* [*São Sabbas et al.*, 2003a].

Chapter 3 investigates the dynamical relationship between the occurrence rates of cloud-to-ground lightning and sprites, and convective activity of the associated

thunderstorm as revealed in infrared cloudtop temperatures (T_c) from satellite imagery. Here the thunderstorm generating the sprites and lightning analyzed in the previous chapter were investigated in detail to ascertain the relationship of lightning and sprites to the convective regions of the storm where gravity wave generation would maximize. The maximum sprite and –CG production of the system occurred when the contiguous cloud cover of the coldest region with T_c < -52° C reached its maximum area. This work, the first of its kind, revealed a tighter correlation between the total –CG activity and sprite activity during the convective development of a thunderstorm than was previously known. These and other results of this study are published in the *Geophysical Research Letters* [*São Sabbas et al.*, 2003b].

Chapter 4 presents results of an investigation of the effects of conductivity inhomogeneities in the mesosphere/lower ionosphere on determining sprite ignition locations. Self-consistent simulations of the quasi-electrostatic field generated by lightning were performed using neutral density, electron density and ion conductivity profiles appropriate to midlatitude nighttime conditions. The evaluation of the interaction of only the quasi-electrostatic component of the field with the conductive medium was based on the fact that the time scale of sprite generation, of the order of   to 10s of   , is much longer than the characteristic time scale of electromagnetic processes in the mesosphere, of the order of 10s to 100s of μs. The simulations included nonlinear modifications to the conductivity from changes in ionization, attachment and electron heating, and were carried out until the termination of the underlying lightning discharge. The objective was to verify where and under what conditions electric breakdown would occur, given the parameter space explored in the simulations. The production of sprites involves the nonlinear physics of streamer and is not part of the objectives of this dissertation. The simulations verified that spatial perturbations in the conductivity lead to electric breakdown in isolated patches of reduced neutral density, where sprite ignition may occur.

Chapter 5 summarizes the main results of this dissertation and presents the conclusions.

CHAPTER 2

STATISTICAL ANALYSIS OF SPACE-TIME RELATIONSHIPS BETWEEN SPRITES AND LIGHTNING [1]

2.1 MOTIVATION

Boccippio et al. [1995] first established that a +CG lightning precedes most sprites by approximately 20-30 ms. In their study, totals of 42 and 55 sprites observed in July 12 and September 7, 1994, respectively, were analyzed. Approximately 86% and 82% of the sprites each night, respectively, were preceded by a +CG recorded by the National Lightning Detection Network (NLDN), and 95% and 78% were preceded by a Q-burst (large excitation of the normal modes of the Earth-Ionosphere cavity in the Extremely Low Frequency (ELF) Schumann resonance band), recorded by an ELF sensor. Subsequent studies have reported results that are generally consistent with these observations [*Lyons*, 1996; *Cummer and Inan*, 1997; *Bell et al.*, 1998].

Based on observations showing evidence that sprites are strongly associated with positive cloud-to-ground lightning, several mechanisms have been proposed to explain the sprite generation process [*Boccippio et al.* 1995; *Pasko et al.*, 1997b, *Bell et al.*, 1995; *Roussel-Dupré and Gurevich*, 1996; *Taranenko and Roussel-Dupré*, 1996]. A widely accepted model [*Pasko et al.*, 1997b] uses a quasi-electrostatic approach in which a transient electric field generated by a +CG is the dominant trigger mechanism for sprites. Because of the higher altitude of the positive charge center inside the thunderstorm assumed in this model and the higher incidence of continuing current among +CGs when compared to other types of lightning, the charge moment (total charge removed x altitude) of +CGs is on average greater than other types of discharges, making +CGs more effective at generating sprites than other types of lightning. However, the model does not rule out occasional -CGs and intracloud discharges (ICs) with a large enough

---

[1] São Sabbas, F. T., D.D. Sentman, E.M. Wescott, O. Pinto Júnior, O. Mendes Júnior and M. J. Taylor, Statistical analysis of space-time relationships between sprites and lightning, *J. Atmos. Solar-Terr. Phys.*, 65(5), pp. 523-533, 2003.

charge moment to generate a breakdown electric field in the mesosphere and produce a sprite.

Using an extensive set of low-light TV data from the summer of 1996, *São Sabbas* [1999a,b] analyzed 746 sprites from 7 different nights and found that only 65% of sprites were associated with +CG recorded by the NLDN, suggesting that other types of lightning besides +CGs could be generating sprites. About 11% of sprites were found to be immediately preceded by a -CG, and 24% of sprites were not associated with a CG registered by the NLDN. At the time this study was performed no association between sprites and -CG had been reported. In an independent study, *Barrington-Leigh at al.* [1999] subsequently reported observations of 2 sprites that had a -CG VLF signature associated with them. Those results support *São Sabbas* [1999a,b] suggestion that +CGs are not the only type of lightning that can generate sprites.

This chapter reports results of a detailed statistical study of the space-time association of sprites with positive and negative CGs [*São Sabbas et al.,* 2003a]. In most previous studies of the association of sprites with lightning, sprites were assumed to be centered above the causative +CGs, which were identified based on timing proximity [*Lyons*, 1996; *Cummer and Inan*, 1997; *Bell et al.*, 1998]. *Lyons* [1996] and *Wescott et al.* [1998b; 2001] have triangulated the location of sprites showing that they are actually laterally displaced from the +CGs. *Lyons* [1996], using 7 events, found an average displacement ~42km, and *Wescott et al.* [1998b; 2001], using 20 events, found an average displacement ~25km. In the present study the association of sprites with ±CGs preceding the sprites was investigated based on time and distance. The distribution of distances, and time differences between the parent +CG and the sprite, and the peak current distribution of the sprite-associated +CGs were calculated. The results obtained here were compared with four previous observational studies.

2.2 OBSERVATIONS

A set of 40 sprite events recorded on July 22, 1996, during the Sprites96 Campaign, conducted in the central United States, was analyzed. The location of cloud-to-ground lightning discharges of the sprite producing thunderstorm, recorded by the NLDN between 00:00 and 14:00 UT, are shown in Figure 2.1 together with locations of CGs from other thunderstorms. Sprites were documented above the Mesoscale Convective Storm (MCS) over Kansas.
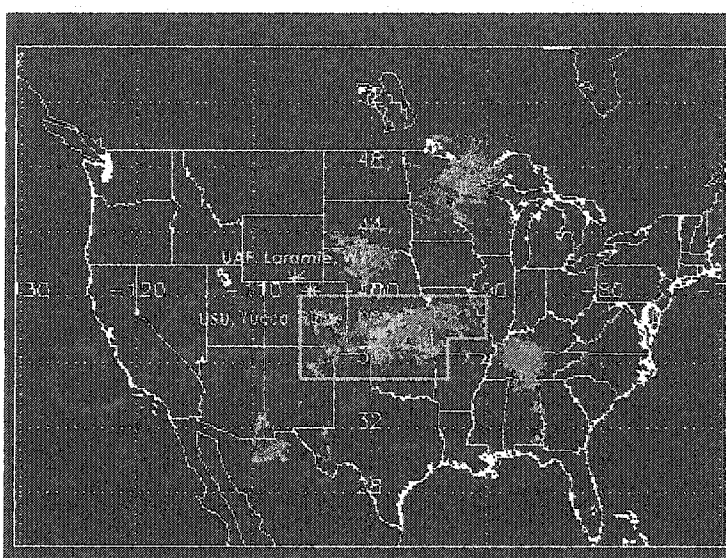
Figure 2.1. Map of United States showing location of CGs. The +CGs (red), -CGs (blue) and +CGs possibly associated with sprites (green), occurred between 0 and 14 UT, on July 22, 1996. The lightning from the sprite producing storm is within the green rectangular region. Yellow asterisks indicate the locations of the two ground observation sites.

The location of the sprites was triangulated, with an accuracy of a few to several tens of km, from images simultaneously obtained by University of Alaska (UAF) and Utah State University (USU) located at different ground optical sites. *Wescott et al.* [2001] provides a good description of the triangulations techniques used here. Simultaneously recorded sprites were easily identified by comparing their time and visual characteristics in the images recorded by UAF and USU. The UAF observations were made from the Wyoming Infra-Red Observatory (WIRO, 41.098° N, 105.997° E, 2.943

km alt.), on Jelm Mountain, Wyoming, using an unfiltered intensified (~600-800 nm BW) CCD video camera with ~ 17° FOV operating at 30 frames/sec (fps). A GPS clock was coupled to the camera system to provide time stamped images (TV fields) with a resolution of ~16.7 ms (1 field), and an absolute scan line accuracy of 1 μs. The GPS time stamped onto the image (t_{field}) corresponded to the very last scan line of each field, and was used as the sprite time (t_{sprite}).

The USU observations were obtained from Yucca Ridge Field Station (YRFS, 40.669° N, 104.939° E, 1.6 km alt.), located 20 km northeast of Ft. Collins, Colorado. Sprites were recorded at 25 frames/sec (fps) using an Isocon camera with ~22° field-of-view (FOV). The camera was fitted with a 665 nm interference filter to image sprites in the N_2 first positive system, and each video field was uniquely time stamped using a crystal clock oscillator with a drift of ~2 s/day assumed to be linear. The clock was set manually at the start of each night to an accuracy of better than 1 sec [see *Armstrong et al.*, 1998 for details].

The lightning information was provided by the NLDN [*Cummins et al.*, 1998a, 1998b]. Broadband electric field data (between ~200 Hz and ~200 kHz) recorded from the Langmuir Laboratory, New Mexico [*Stanley, et al.*, 2000], were examined to look for Very Low Frequency (VLF) signatures (3-30 kHz) of CGs flashes in the cases for which NLDN did not record a lightning signature.

2.3 IDENTIFICATION OF SPRITE INDEPENDENT EVENTS

Initially, 47 sprites recorded from both ground sites were visually identified and triangulated. To be identified as an independent event, a sprite had to have occurred with a time separation of at least 1 video field (~16.7 ms) and be spatially distinct from any sprite occurring in the previous field. The spatial displacement requirement prevented counting a re-brightening or the continuity of previous processes as distinct events. Individual events could be single "sprite units" [*Sentman et al.*, 1995a] or what was

defined as "sprite spatial groups," i.e., a group of units that occurred simultaneously, within a single video field (e.g. Figure 2.9).

This preliminary definition, based solely on video images, proved not to be completely unambiguous in the case of complex events when a single lightning discharge generates consecutive sprites. Hence, a statistics based on both the time interval between a sprite and its nearest preceding (parent) +CG, and on triangulation was constructed according to the following procedure. The parent CG candidates, positive or negative, were initially screened by requiring the CG to have occurred in a space-time vicinity of the sprite defined as a square region of 400 km on a side, centered on the sprite, and within a one second window preceding the sprite. Cloud-to-ground lightning registered by NLDN, occurring closest in time preceding the sprite and closest in space, were selected as being the parent CG. NLDN uncertainty in time is 1 μs and in location is 0.5 km [*Cummins et al.*, 1998a]. For CGs with a VLF signature and no NLDN signature, only the time criterion was applied. Negative CGs were selected only if neither the NLDN nor the Broad band electric field sensor recorded a positive CG. To calculate the time interval between sprites and parent +CGs ($\Delta t = t_{sprite} - t_{lightning}$) the GPS time tag of the video field (t_{field}) in which the sprite first appeared was used as t_{sprite} (Figure 2.2).
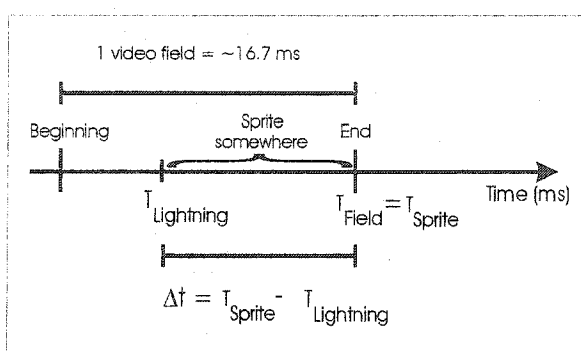
Figure 2.2 Diagram showing how Δt can be < 16.7 ms. The lightning occurs before the sprite and the GPS time stamped at the end of the field is assigned as t_{sprite}. Due to causality the sprite must have occurred some time after the lightning but before the end of the video field.

In the video systems used in this study the time stamp on each image field refers to the end of the video field. Each video field has a duration of ~16.7 ms, so the start of

the image is at t_{field} −16.7 ms and the end is at t_{field}. When a sprite is present in a field, t_{sprite} is assumed to be t_{field}, which is the maximum time at which the sprite could have occurred. The sprite could have occurred at any instant in the interval t_{field} -16.7 ms to t_{field}, hence 16.7 ms is the experimental error in t_{sprite}. In the cases when the parent lightning occurs within the interval of the video field containing the sprite, $t_{lightning}$ provides a minimum time at which the sprite could have occurred, and Δt (t_{sprite} - $t_{lightning}$) will be less than 16.7 ms, since causality requires the sprite to have occurred at some instant of time after $t_{lightning}$ and before t_{field}. The sprite must be constrained to this interval. Hence when the parent lightning occurred within the sprite video field $\Delta t < 16.7$ ms, the uncertainty in the sprite time is equal to Δt in these cases. If the actual times of sprites are statistically distributed uniformly $0 \leq \Delta t \leq 16.7$ ms, the mean uncertainty is 8.5 ms. A conservative estimate of 10 ms is adopted for the statistical uncertainty.

Figure 2.3 shows the distribution of time intervals between sprites and parent +CGs. The first bin ($0 \leq \Delta t < 10$ ms) and part of the second bin ($10 \leq \Delta t < 20$ ms) represent the cases in which the parent lightning occurs within the interval of the video field containing the sprite, discussed in the previous paragraph. The time-interval distribution peaks around 10-20 milliseconds and has a mean value of 30 ms (20 ms if the 2 outlying events are excluded). This distribution agrees with *Bell et al.*, [1998] results.
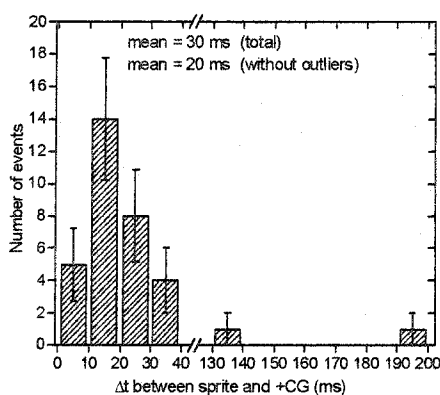
Figure 2.3 Distribution of the time difference ($\Delta t = t_{sprite}$ - $t_{lightning}$) between the sprite and parent +CG. The flashes were binned in intervals of 10 ms. The error bars are the statistical (standard) errors, i.e. the square root of the number of events in each bin. The horizontal error (not shown) is the estimated statistics uncertainty of 10 ms.

Bell et al., [1998] suggested that the longest delays observed in their study were associated with small sprites for which horizontal intracloud discharges removed the amount of charge necessary to generate them. Furthermore, Δt would vary from 0-15 ms for the larger events to 100 ms to the smallest events. The sprites analyzed here were grouped in three categories with respect to visual size and brightness: small, medium and large. The three groups were statistically consistent with each other (graph not shown). No consistent visual distinction between sprites with short and long Δt; was observed, in fact, the two events with largest Δt (outliers) were very bright (large) sprites. The results suggest that the time delay between lightning and sprites characterizes the time scale of the duration of the physical process (or processes) that is responsible for the sprite initiation, and takes place once the transient electric field is established in the mesosphere. This process is discussed in recent models based on streamer physics [*Pasko et al.*, 1998; *Raizer et al.*, 1998] that explain in detail how the fine structure observed in high-speed [*Stanley et al.*, 1999; *Stenbaek-Nielsen et al.*, 2000] and telescopic [*Gerken et al.*, 2000] images of sprites develop.

The process that originates a streamer can be triggered from an avalanche initiated by a single electron. The avalanche creates a local charge separation, and the streamer develops when the electric field of the space charge equals the external transient electric field in the mesosphere generated by the CG. *Pasko et al.* [1998] have modeled the characteristic time of this process as $t_z = z_s/v_d$, where $z_s = (1/\alpha) \ln(4\pi\varepsilon_0 r_s^2 E_k/e)$ is the distance over which the avalanche generates a space charge field comparable to the ambient electric field, taken to be the breakdown field (E_k). Here, $\alpha = (v_i - v_a)/v_d$, where v_i is the ionization rate, v_a is the electron attachment rate, v_d is the electron drift speed, and the space charge is assumed to be concentrated in a sphere of radius $\sim r_s$. Figure 1 of *Pasko et al.* [1998] shows the altitude profile of the modeled t_z. The distribution of Δt between the sprite and parent +CG shown in Figure 3 is consistent with the characteristic time scale for the development of an individual electron avalanche into a streamer between $\sim$70-85 km altitude modeled by *Pasko et al.* [1998].

Figure 2.4 shows the distribution of distances (Δs) between the triangulated nadir point (latitude and longitude) of sprite events and the location of parent +CGs. The distances between sprite events and parent +CGs were calculated for the +CGs detected by the NLDN only. When the sprite events were "spatial groups" an average nadir point was calculated using the triangulated nadir points of each "sprite unit." The distribution displayed in Figure 2.4 shows that approximately two thirds of sprites occurred within ~50 km from the parent +CG, in agreement with Lyons [1996] and Wescott et al. [1998b, 2001]. The maximum distance observed was ~82 km. Since "spider" discharges extending for ~100 km have been previously observed [Lyons, 1996], it is possible for sprites to occur with Δs = ~82 km. All +CGs in the present study had Δs consistent with previous results, and no further spatial selection criteria were applied to identify independent events.
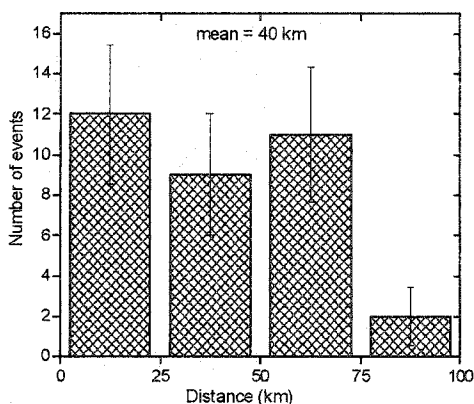
Figure 2.4 Distribution of the triangulated distances between sprites and parent +CG. The events were binned in intervals of 25 km, and the "error bars" are the statistical (standard) errors. The horizontal error (not shown) is the estimated mean uncertainty of the triangulated distances, 10 km.

The time intervals versus the distance (Figure 2.5) were also plotted and there was no statistically significant correlation between the two quantities, i.e. sprites further away from the +CG do not appear to have longer delays.
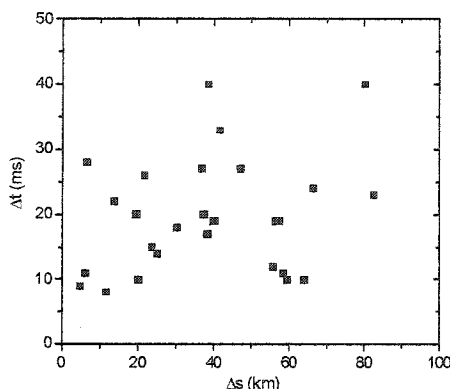
Figure 2.5 Time interval between sprites and associated +CGs versus the distance. The two outliers, one with Δt=140 ms and Δs=51 km, and the other with Δt=197 ms and Δs=75 km, are not shown. The errors associated with the data points (not shown) are the estimated mean uncertainties of Δt, 10 ms, and Δs, 10 km.

Most sprites (~95 +5/-15 %) that were associated with +CGs occurred within 40 ms after the parent +CG, where the uncertainties are the estimated standard errors. Only two events occurred with a Δt greater than 40 ms after the +CG. Given the large time interval that those sprites had from their parent +CG (140 and 197 ms) it is possible that closer +CGs had occurred but were not registered by either NLDN or the Broadband electric field sensor.

Except for the two outlying events, the analysis of Figure 2.3 suggests 40 ms as an effective upper limit for the delay between the parent +CG flash and the sprites observed during this night. The 40 ms delay exceeds the experimental error of ~16.7 ms by a factor of ~2.5 and the statistical uncertainty by a factor of 4, and is therefore a robust result. Based on this result, consecutive sprites that had a minimum time separation of ~16.7 ms from each other and a maximum time interval of 40 ms from the parent CG were grouped into a "sprite time group," similar to the manner in which individual strokes are grouped into flashes [*Cummins et al.*, 1998a, 1998b]. The individual "sprite units" [*Sentman et al.*, 1995a] or "sprite spatial groups" were called "sprite time units." Seven sprites that did not have a +CG registered by any system, and which had been initially considered to be independent events were reclassified to be sprite time units

forming a sprite time group. The hypothesis used here is that if the electron avalanche can take up to 40 ms to develop into a streamer in a particular location, multiple sprite time units could be produced by the same CG at different locations, with a varying duration for the streamer development, probably influenced by the local mesospheric characteristics, within a maximum Δt of 40 ms from the CG. The total number of sprite events was thereby reduced from 47 to 40, 7 events being sprite time groups with 2 sprite time units each.

The definition of what an independent sprite event might be has been extensively but informally discussed within the sprite community; the topic has not yet been approached in the scientific literature. There is no established definition of "independent sprite event." This is an important issue since any analysis of the temporal and spatial relationship between sprites and lightning based on observational data is affected by how and if sprites are grouped into independent events, i.e., by the definition used. For the sprites occurring on July 22, 1996, analyzed in this paper, the maximum Δt observed, excluding the 2 outliers, was 40 ms. However this could be a particularity of this specific night, resulting from a combination of the characteristics of the thunderstorm, lightning activity and local mesospheric conditions. For example, applying the same selection criteria for parent +CGs (closest in time preceding the sprite and closest in space), a preliminary analysis of 69 triangulated sprites from July 24, 1996, resulted in only $58\pm9\%$ sprites occurring within 40 ms after the parent +CG (not shown). That illustrates the necessity of a detailed statistical study of a large data set of triangulated sprites with GPS timing from a variety of storms and locations to establish a definition of independent sprite event with bounded variances that can be widely adopted.

2.4 SPRITE ASSOCIATION WITH LIGHTNING AND COMPARISON WITH OTHER STUDIES

Within the redefined data set of 40 sprite events, about 73±13% of the sprites were associated with a +CG recorded by the NLDN, where in this and the following percentages the quoted uncertainty is the statistical (standard) error. This percentage increased to 82±14 % when VLF signatures for +CGs not detected by the NLDN were considered. NLDN has detection efficiency around 90% for -CGs [*Cummins et al.*, 1998a]. The detection efficiency of +CGs has not been documented, but may be assumed to be similar to this. The 10% change in the number of sprites associated with +CGs when VLF data is considered supports this assumption.

The percentage of sprites associated with lightning calculated in this work was compared with values reported by *Boccippio et al.* [1995], *Lyons* [1996] and *São Sabbas* [1999a]. *Boccippio et al.* [1995] compared the time of occurrence of sprites, recorded in GPS time-stamped low-light-level video images, with the time of lightning discharges from the associated thunderstorms recorded by the National Lightning Detection Network (NLDN), as well as with electromagnetic "Q-bursts" events. The ELF data was time-tagged with an internal PC clock that drifted ~13 s/day. The drift was assumed to be linear. An algorithm generated by comparing the recorded onset times with the GPS-timed sprite events corrected the drift. The sprites occurred above thunderstorms over the central U.S. and were observed from Yucca Ridge. The identification of the parent +CGs of the sprites was based mainly on timing. Sprite locations were not triangulated, and the spatial requirement was that NLDN and/or ELF signatures must have originated from the same thunderstorm that generated the sprites.

Lyons [1996] studied 36 sprites recorded in GPS time stamped images from Yucca Ridge, during a 2 hr interval. The sprites occurred above a Mesoscale Convective System (MCS) over Nebraska on August 6, 1994. *Lyons* [1996] reported that 94% of sprites were preceded by +CGs registered by the NLDN. Seven sprites were triangulated

and the location of the other sprites was estimated based on the location of the parent +CGs, which was identified based on timing.

São Sabbas [1999a] analyzed 746 sprites from 7 different nights in 1996, recorded from Yucca Ridge by Utah State University. The sprites occurred above thunderstorms over the central U.S. on July 6, 7, 11, 19, 21, 22 and 24, 1996, and were imaged using the same system describe in the section 2. To compensate for the time uncertainty of this system, a selection window with Δt of 360 ms before the sprite and 60 ms (3 fields at 25 fps) afterwards was adopted in identifying the parent +CG. Sprites were not triangulated in this study, so to be considered a possible parent the +CG had to be inside the field of view of the camera. With this approach several +CGs that were not associated with sprites may have been incorrectly tagged as the possible parents of sprites. Nevertheless, only $65\pm3\%$ of the sprites were associated with a +CG signature registered by the NLDN. The same criteria were used to look for a possible association of sprites with -CGs when there was no +CG. Table 2.1 summarizes these results.

Table 2.1 Comparison of Reports of the Percentage of Sprites Associated with +CGs

Study	Dates	Report	Total number of sprites	Percentage of sprites with +CGs detected by the NLDN
1	July 12, 1994	Boccippio et al., 1995	42	$86\pm14\%$
2	September 7, 1994	Boccippio et al., 1995	55	$82\pm12\%$
3	August 6, 1994	Lyons, 1996	36	$94\pm16\%$
4	July 6, 7, 11, 19, 21, 22, 24, 1996	São Sabbas, 1999a	746	$65\pm3\%$
5	July 22, 1996	This study	40	$73\pm13\%$

The definitions of sprite independent event utilized for studies 1 to 3 were not available, in study 4 all sprite time units were considered to be independent events. The statistical uncertainties of these percentages were estimated using $\Delta x = x/(N\sqrt{x})$, where x is the number of events relative to the percentage (x/N) and N is the total number of events, and are included in Table 2.1. These results, including the estimated uncertainties, are plotted in Figure 6. The figure also shows the Least Upper Bound

(LUB) and the Greatest Lower Bound (GLB) of the uncertainties for studies 1, 2, 3 and 5. When these uncertainties are taken into account, studies 1, 2, 3 and 5 are statistically consistent among themselves within the region bounded by the LUB and GLB. Report number 4 however is statistically distinct from the other reports, since its error bars do not fall within their LUB and GLB. The low percentage (65±3%) of sprites associated with +CGs was obtained using a large time selection window, and a data set on average 17 times larger than the data sets utilized in the other studies. Even adjusting upwards by 10% to approximately compensate for the 90% detection efficiency of NLDN, 25±2% of sprites remains without +CGs. *São Sabbas* [1999a] suggested that –CGs and intracloud discharges were generating the sprites without +CGs that could not be explained by NLDN detection efficiency.
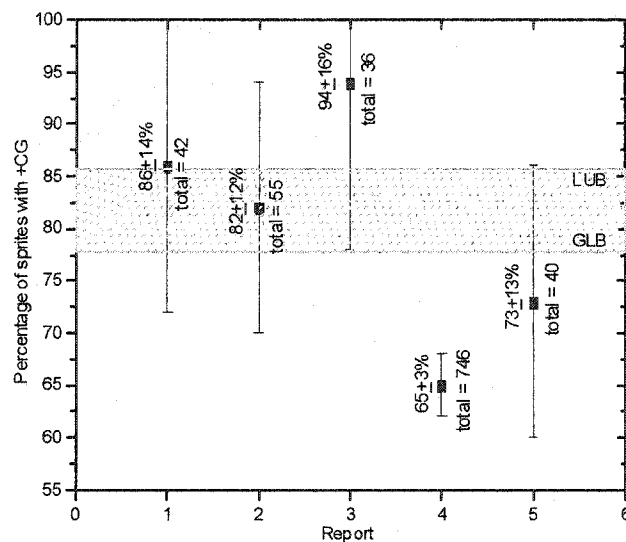
Figure 2.6. Comparison between the statistical studies. The percentages of sprites associated with +CGs were calculated using NLDN data. The region between the Least Upper Bound (LUB) and the Greatest Lower Bound (GLB) is highlighted.

Table 2.2 shows the percentage of positive and negative lightning relative to the total lightning (positive + negative) for the sprite producing thunderstorm of July 22,

1996 analyzed here, together with percentages for other nights analyzed by *São Sabbas* [1999a,b]. The table also shows the number of sprites observed and duration of the sprite production period for comparison. All storms had small percentages of +CGs (from 7.3% to 17.0%), showing that the production of a large percentage of +CGs by the thunderstorm is neither a necessary condition for sprite occurrence nor a determining factor for the number of sprites produced.

Table 2.2 Lightning and Sprite Related Data [*São Sabbas*, 1999a]

July, 1996	Percentage of +CGs relative to total	Percentage of -CGs relative to total	Total number of CGs	Number of sprites	Duration of sprite period
6	10.9% (2652)	89.1% (21740)	24392	36	2 h 34 m
7	14.1% (1367)	85.9% (8318)	9685	88	4 h 22 m
11	10.7% (1928)	89.3% (16129)	18057	38	1 h 32 m
19	7.3% (1086)	92.7% (13714)	14800	83	3 h 05 m
21	17.0% (1504)	83.0% (7327)	8831	212	3 h 27 m
22	10.9% (4412)	89.1% (36193)	40605	84	4 h 07 m
24	9.0% (5088)	89.0% (51446)	56534	205	5 h 20 m

Figure 2.7 shows a relationship between the onset of sprite production and growth in the rate of occurrence of the storm's +CG for all peak current ranges. Of the seven days in 1996 studied by *São Sabbas* [1999a,b], July 21, 1996, is the only day for which the onset of the sprite occurrence might have been observed, since the observations for this day started before lightning activity. In all other days, lightning activity had already commenced before observations began. On July 21, 1996, sprites were observed to commence after a continuous growth in the occurrence rate of storm's CGs, for all peak currents ranges. All other days had similar growths and peaks in the +CG occurrence rate of storm's +CG before the beginning of the observation period (not shown).
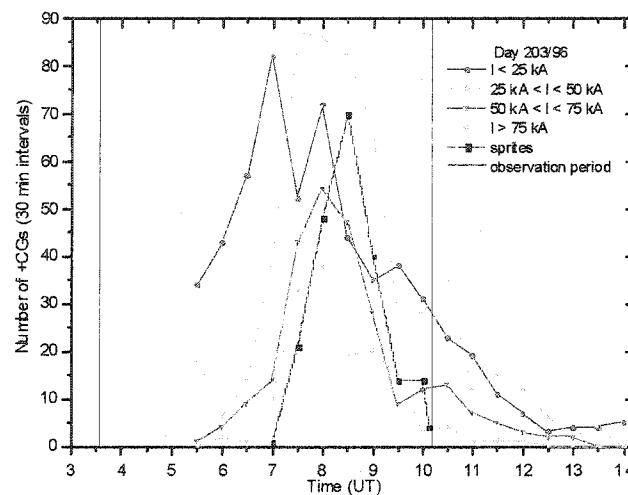
Figure 2.7 30-min +CG rate for different peak current ranges. The data is for day 203/96 [*São Sabbas*, 1999a,b]. The vertical black line delimitate the observation period. Sprites started to occur at 6:40 UT.

2.5 NEGATIVE SPRITES AND SPRITES WITHOUT A CG

Approximately 27±8% of sprites did not have a parent +CG recorded by the NLDN, and 17±7% had neither NLDN nor VLF signatures. Two of the seven sprite events that had neither a NLDN nor VLF +CG signature were preceded by a -CG (Figure 2.8a and Figure 2.9a). Figure 2.8 shows three consecutive independent sprite events. The time separation between the first and second events is 50 ms, and between the second and third is 117 ms. The first event (Figure 2.8a) was preceded by a negative CG with $\Delta t = 9$ ms. This flash was not registered by the NLDN, but it was registered by the New Mexico Tech VLF system. Due to its small Δt it is very likely that this –CG, in fact, generated the sprite. The second sprite (Figure 2.8b), considered as an independent event here (occurred 59 ms from the –CG associated with the first sprite), was not associated with any detected CG, positive or negative.

(a)   (b)   (c)
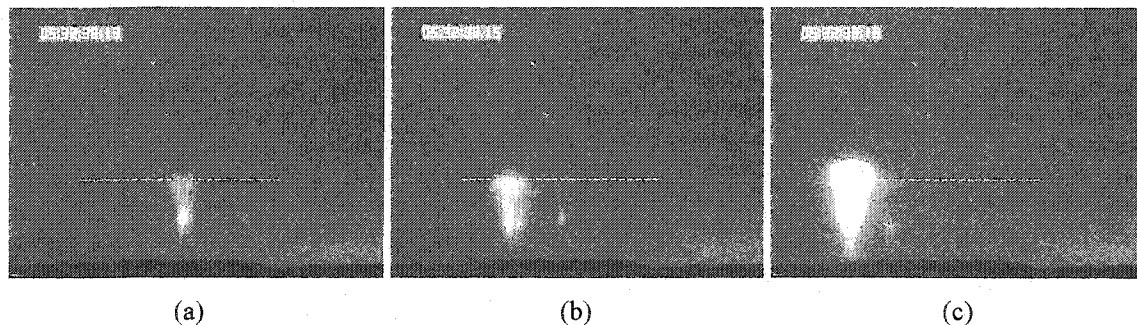
Figure 2.8 Three consecutive independent sprite events. The time separation is 50 ms (a and b) and 117 ms (b and c), respectively. The first sprite (a) was preceded by a –CG recorded by the Broad band electric field sensor (no NLDN), Δt=9 ms. The second sprite (b) had no CG signature associated with it in either NLDN or VLF, and the third (c) was preceded by 48 kA +CG recorded by both systems, Δt=17 ms and Δs=78 km. The images shown were obtained by UAF

The third event (Figure 2.8c) had both NLDN and VLF +CG signatures preceding it by 17 ms. The +CG had a peak current of 48 kA and occurred ~78 km from the sprite. The discharge had a slow tail in VLF that lasted ~0.5 ms. It was followed, ~4 ms afterwards, by a slow energetic field change, possibly due to the sprite, that lasted ~1 ms (not shown). The "positive sprite" (Figure 2.8c) was the brightest of these three consecutive events, but there were other "positive sprites" that occurred during the night of the study that were much smaller and dimmer than the possible "negative event" displayed in Figure 2.9a. The variation of brightness of the sprites with respect to underlying lightning characteristics is not yet well understood.

The second sprite preceded by a -CG detected in this study is shown in Figure 2.9a, together with a "positive sprite" (Figure 2.9b) for comparison of visual characteristics. The -CG was recorded by the NLDN and VLF system 146 ms before the sprite, had a peak current of 22 kA and occurred at a distance of ~201 km from the event. Because of the large Δt and distance between this sprite and the –CG, it is possible that both NLDN and VLF systems missed a +CG (or –CG) that would have a better association with this event. The units of this sprite, shown in Figure 9a, were slightly brighter and larger than the units of the positive sprite of Figure 9b. The sprite in Figure

9b was preceded by a +CG with a Δt equal to 28 ms. The +CG peak current was 47 kA and it occurred ~9 km from the sprite.

(a)   (b)
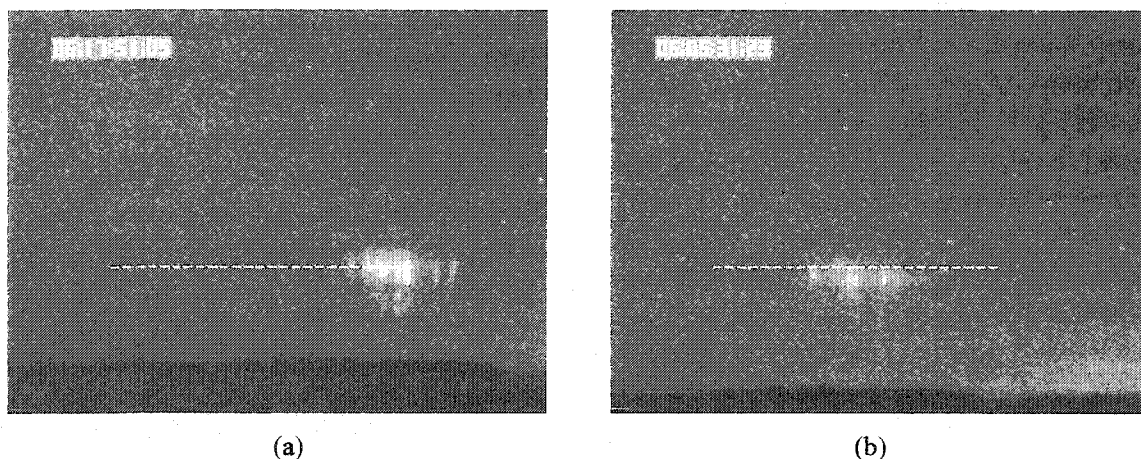
Figure 2.9 Comparison between negative and positive sprites. The first image (a) shows a sprite preceded by a 22 kA -CG recorded by both NLDN and VLF systems, Δt=146 ms and Δs=201 ms. The second (b) shows a similar type of sprite event that was preceded by a 47 kA +CG, Δt=28 ms and Δs=9 km. The images shown were obtained by UAF.

None of the sprites without +CGs had any particular characteristics that would visually distinguish them from the positive sprites. An upward-downward difference in the branch orientation might conceivably be expected for sprites generated by lightning of different polarities. However this difference was not expected to appear in a 16.7 ms integration image; it is more likely to show on 1 ms images from high-speed cameras (e.g., *Stanley et al.*, [1999]; *Stenbaek-Nielsen et al.*, [2000]). Comparatively, the percentage of "bright" and "small" events was about the same for positive and negative sprites.

There are two possible interpretations for the sprites without a +CG. The first is that they were preceded by positive strokes undetected by either the NLDN or the VLF systems. An alternate interpretation is that other types of lightning besides +CGs, e.g., negative CGs and intracloud discharges, may also generate sprites. This interpretation is supported by the *São Sabbas* [1999a, b] studies, and is not ruled out by *Pasko et al.*

[1997b] quasi-electrostatic model, or the *Pasko et al.* [1998] and *Raizer et al.* [1998] streamer models. Sprites generated by other types of lightning besides +CGs would represent a smaller portion of the total, such as may have been observed here. Furthermore, according to *Dejnakarintra and Park* [1974], and *Baginski et al.* [1996], vertical intracloud discharges that annihilate positive charge at the top of the clouds and negative charges at the bottom can both generate large electric fields in the upper atmosphere, also supporting this interpretation.

2.6 PEAK CURRENT DISTRIBUTION OF PARENT +CGS

Figure 2.10 shows the peak current distribution of the sprite's associated +CG. The distribution exhibits a maximum for peak current between 40-50 kA. Five out of the 29 (17±7%) +CG flashes preceding sprites had high peak currents (> 75 kA). The average peak current of 60 kA in the present study agrees with the 52 kA reported by *Bell et al.* [1998], and supports results showing that the peak currents of +CGs producing sprites span a large range of values.
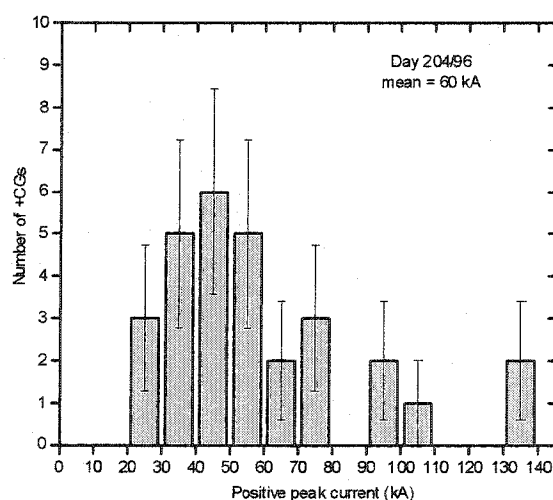
Figure 2.10 Peak current distribution of the parent +CG flashes. The +CGs are binned in intervals of 10 kA. Error bars are the statistical errors.

Figure 2.11a shows that the peak current distribution of sprite's associated +CGs in the 7 storms studied in *São Sabbas* [1999a,b] also has a maximum around 40-50 kA, and is statistically consistent with the one reported here (Figure 2.10). Both distributions are different from the distribution for all +CGs in the 7 storms (Figure 2.11b), which peaked at 10-20 kA and had a mean value of 27 kA. This difference in distributions is one of the principal characteristics that appear to distinguish the lightning population associated with sprites from those not associated with sprites. The peak current distribution of the -CG candidates found in the *São Sabbas* [1999a] studies and the totality of -CGs of the storm are quite similar to each other; both are centered at 10-20 kA (not shown).

(a) (b)
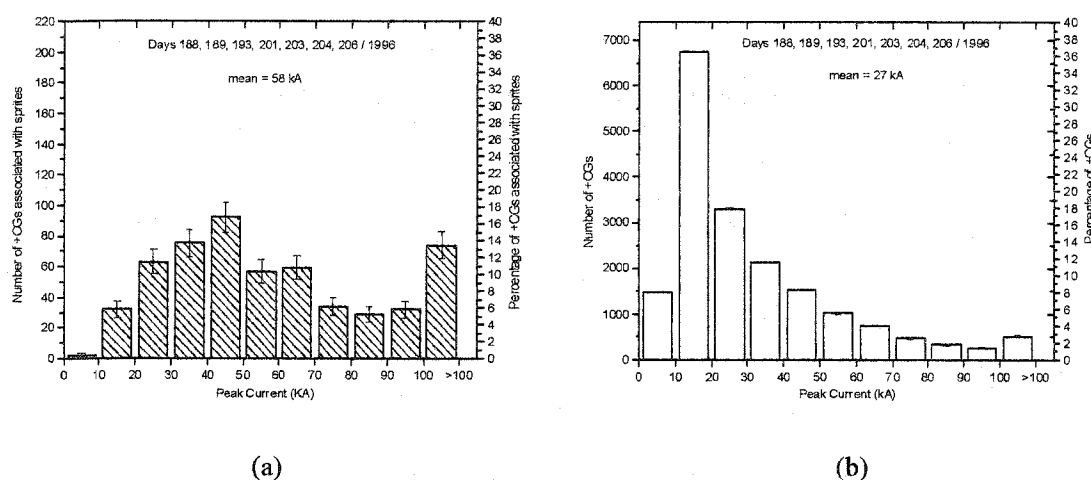
Figure 2.11. Percentage distribution of the peak currents. The figure shows +CGs associated with sprites (a), and (b) the totality of +CGs of the storm [*São Sabbas et al.*, 1999a]. The last column, in both figures, is the percentage of all +CGs with peak current greater than 100 kA.

2.7 SUMMARY OF RESULTS

A detailed statistical analysis of the space-time relationships between sprites and the associated lightning characteristics has been performed. The results of this study can be summarized as follows:

1. A set of 40 sprite events from the Sprites96 campaign was analyzed. Seven of the events (17%) did not have a parent +CG registered by either NLDN or VLF sensors. Images of these events revealed no particular visual characteristics that distinguished them from positive sprites, and such differences are not expected at 16.7 ms integration. Two of the sprites without +CGs were preceded by a –CG, one of them was very likely to be associated with the -CG, which was registered by the VLF system 9 ms before the sprite.

2. No correlation between the apparent visual size and brightness of sprites, and time delays from the associated +CGs was found. No correlation was found between the size or brightness of sprites and the time interval or distance from their parent lightning, i.e. smaller/dimmer sprites or sprites further away from the associated +CG did not have longer time delays from the parent +CG then the bulk of the sprite population.

3. The distribution of time intervals between sprites and parent +CGs showed a peak between 10-20 ms with a mean of 30 ms (20 ms excluding the outliers). The results suggest that this distribution characterizes the time scale for the development of an individual electron avalanche into a streamer between ~70-85 km altitude, as given in the *Pasko et al.* [1998] model. Most sprites occurred within 40ms from the parent +CGs, suggesting this time interval as upper limit for the characteristic time delay between the +CG flash and the sprites observed during this night.

4. The distribution of the distance between sprites and parent +CGs showed that sprites have the tendency to occur within 50 km lateral displacement from the CG,

consistent with results previously reported by *Wescott et al.* [1998, 2001] and *Lyons* [1996].

5. The peak current distribution of +CGs associated with sprites exhibited a larger mean and standard deviation than the distribution of all positives in the storm. It had a maximum between 40-50 kA and a mean of 58 kA, compared to a 10-20 kA maximum and 27 kA mean of the distribution for all positives.

This is the first statistical study to use both GPS timing for images and triangulated positions of sprites, where both temporal and spatial criteria are used to select the parent +CG. Additional statistical studies utilizing large data sets (>100 sprites) over numerous storms distributed globally are necessary to arrive at a tightly parameterized definition of "sprite independent event."

CHAPTER 3

DYNAMICAL RELATIONSHIP OF INFRARED CLOUDTOP TEMPERATURES WITH OCCURRENCE RATES OF CLOUD-TO-GROUND LIGHTNING AND SPRITES [2]

3.1 MOTIVATION

In the Midwest United States, most sprite observations have been made during the May-August summer thunderstorm season, where Mesoscale Convective Complexes (MCC) are somewhat common occurrences [*Lyons*, 1996]. MCCs are a particular type of Mesoscale Convective Systems (MCS). They are meteorological systems with strong convective activity, dimensions between 250 and 2500 km and duration greater than or equal to 6 hr (meso-α scale definition [*Maddox*, 1980]). MCCs were defined based upon physical characteristics observed in enhanced, infrared (IR) satellite images of meteorological systems [*Maddox*, 1980]. Table 3.1 presents the definition criteria.

Table 3.1 Mesoscale Convective Complex (MCC) definition [*Maddox*, 1980]

Size:	A – Cloud shield with continuously low IR temperature ≤ -32° C, area ≥ 100,000 km² B – Interior cold cloud region with temperature ≤ -52° C, area ≥ 50,000 km²
Initiation:	Size definitions A and B are first satisfied
Duration:	Size definitions A and B must be met for a period ≥ 6 h
Max. extent:	Contiguous cold cloud shield (IR temperature ≤ -32° C) reaches maximum size
Shape:	Eccentricity (minor axis/major axis) ≥ 0.7 at time of maximum extent
Termination:	Size definitions A and B no longer satisfied

In addition to the central US, MCCs are common in oceanic and continental tropical regions, especially in the intertropical convergence zone (ITCZ), and over South America [*Conforte*, 1997]. In South America, the MCCs are, on average, about 60% larger in area and persist over longer intervals than similar systems in the US [*Velasco*

---

[2] São Sabbas, F. T., D.D. Sentman, Dynamical relationship of infrared cloudtop temperatures with occurrence rates of cloud-to-ground lightning and sprites, *Geophys. Res. Lett.*, **30**, pp 40-1 to 40-2, 2003.

and Fritsch, 1987], thus making this region the most active in the Western Hemisphere. Sprite observations over different regions of the globe, for example Peru [*Sentman et al.*, 1995c; *Moudry et al.*, 1997], Europe [*Neubert et al.*, 2001; *Taylor*, 2000], and Japan [*Fukunishi et al.*, 2001], reveal that sprites can also be generated over small thunderstorms, suggesting that the type and size of thunderstorms that generate sprites may depend on local meteorological characteristics. Hence, the MCC and/or large size requirements may not be sufficient for assessing the potential for thunderstorms to produce sprites and other optical effects on the upper atmosphere.

This Chapter describes the cloud-top temperature (T_c) characteristics, obtained from infrared GOES-8 satellite images, and the inter-relationships with associated lightning and sprite activity of the July 22, 1996, thunderstorm [*São Sabbas et al.*, 2003b]. The meteorological system was classified according to the *Maddox* [1980] definition. The analysis examined the occurrence rate and location of sprites and lightning with respect to the thunderstorm features and temporal development. The study establishes the base of a robust methodology based on satellite imagery that could be used in investigations of planetary sprite production.

3.2 DATA SET

GOES-8 geosynchronous satellite 10-12 μm IR images of the North America sector over the period 0015-1545 UT containing the meteorological system that produced the sprites on July 22, 1996, was used. The data was provided by the National Climatic Data Center (NCDC), Asheville, North Carolina. The images were stored in as 10 bit McIdas area files, with a spatial resolution of approximately 4 km, temperature resolution 0.1 K, sampled at 30 min intervals. Some of them presented bad scan lines that were corrected using simple linear interpolation. The part of the image corresponding to the sprite-producing MCC and environs (Figure 3.1a) was isolated, remapped to an isometric latitude and longitude grid, and the pixel count values of the remapped region of interest were converted to temperature using the procedures of *Weinreb et al.* [2001] for further

comparison with lightning and sprites. First the count values where converted to radiance using equation 1:

$$R = (X - b)/m \qquad (1)$$

where R is radiance ($mW/[m^2\text{-}sr\text{-}cm^{-1}]$) and X is the image count value. The coefficients $m = 5.2285$ and $b = 15.6854$ are the scaling slope and intercept, respectively.

Radiance was converted to effective temperature using the inverse of the Planck function as follows:

$$T_{eff} = \frac{(c_2 \cdot v)}{\ln[1 + (c_1 \cdot v^3)/R]} \qquad (2)$$

where T_{eff} is effective temperature (K), and R is radiance. The coefficients $v = 934.30$ (cm^{-1}), $c_1 = 1.191066 \times 10^{-5}$ [$mW/(m^2\text{-}sr\text{-}cm^{-4})$], and $c_2 = 1.438833$ (K/cm^{-1}) are the central wavenumber of the channel and the two radiation constants, respectively. The constants c_1 and c_2 are invariant, but v depends on the spectral characteristics of the channel, in this case the 10-12 μm channel.

The effective temperature was converted to actual temperature T ($^{\circ}$C) using the following equation:

$$T = (\alpha + \beta \cdot T_{eff}) - 273 \qquad (3)$$

where $\alpha = -0.322585$ and $\beta = 1.001271$ are two conversion coefficients. (All expressions and coefficients described above are from *Weinreb et al.* [2001].)

Temperature (C)

(a)   (b)
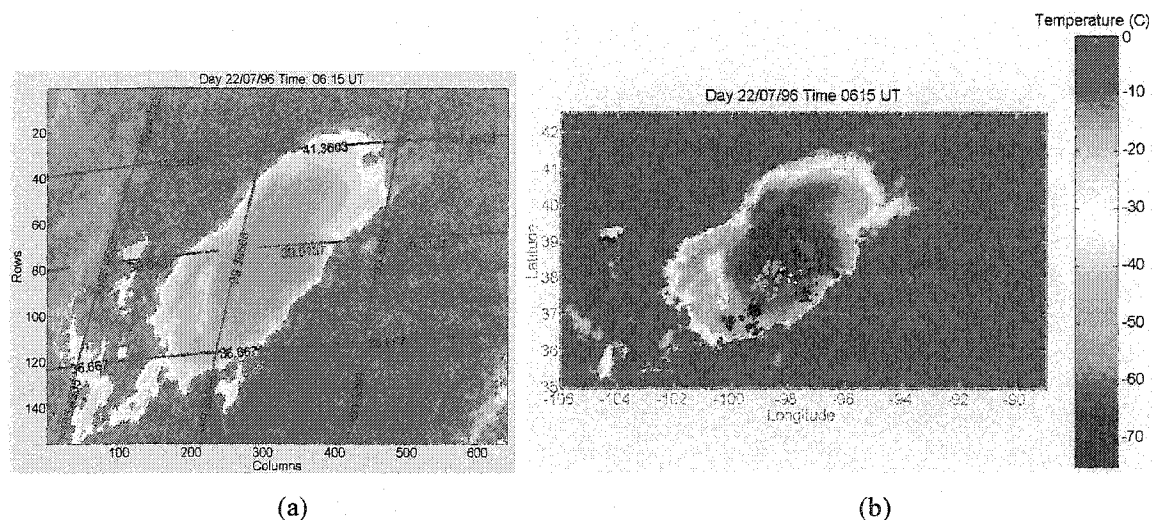
Figure 3.1 IR images of the sprite producing thunderstorm of 22 July 1996. The image was recorder by the GOES-8 satellite at 06:15 UT. Panel (a) is the raw data utilized, i.e., the satellite view. Panel (b) is a cloudtop temperature (T_c) map as a function of latitude and longitude. The map also shows the location of +CGs (pink crosses), –CGs (black dots), sprites (green circles), and +CGs associated with sprites (white circles). The CGs and sprites plotted on this map occurred with ± 15 min from the image time. A similar map showing the association of lightning with cloudtop temperatures has been previously presented by *Lyons* [2000].

Figure 3.1b shows the resulting color-coded temperature map as a function of latitude and longitude (lat/lon) for 0615 UT. To enhance the contrast of the temperature range of the thunderstorm, pixels with temperature above $0°$ C (land area) were set to $0°$ C, represented by a reddish-brown in the color scale used. On these maps were also plotted the location of +/-CGs detected by the NLDN and triangulated locations of sprites that occurred within +/- 15 min of the image, e.g. from 0600- 0630 UT in Figure 3.1.

3.3 ANALYSIS

The lat/lon of the lightning flashes and triangulated positions of sprites were matched to the lat/lon matrices of the images and the pixels with the associated temperatures of the correspondent cloudtop region were identified in the temperature map. For each 30 min image histograms of lightning flashes and sprites versus temperature were assembled. Comparison of the histograms with the lat/lon maps of T_c

showing the locations of +/-CGs shows that, as the storm grows, compact regions of very cold cloudtops develop and the lightning discharges, -CGs more than +CGs, had the tendency to concentrate on those regions. Not all regions with very cold cloudtops exhibited lightning activity, even though cold cloudtops are strong evidence of vigorous convection. Generally, one expects that charge separation, hence lightning, follows convection, leading to an intensification of the lightning activity associated with cold cloudtops.

The histograms were combined into temperature-time diagrams (Figure 3.2) that reveal the evolution of T_c associated with lightning and sprites over the lifetime of the storm. There is some minor smearing in the histograms from samples obtained near sharp temperature gradients, due to the thunderstorm movement northeastward at a rate of several tens of km between the 30 min image intervals. This motion corresponded to several pixels in the IR images, but the overall effect is minor.

Figure 3.2a shows that, throughout the lifetime of the thunderstorm, the –CG occurrence rate increases in association with decreasing T_c during the growing phase, reaches a maximum associated with the coldest T_c (-72° C $\leq T_c \leq -69^{\circ}$ C) that lasts for ~2 h, and then decreases in association with increasing T_c during the decay phase of the storm. The +CG rate (Figure 3.2b) remains associated with approximately constant T_c (-72° C $\leq T_c \leq -69^{\circ}$ C) during the growth of the thunderstorm and also decreases with increasing T_c during the decay phase. The +CGs produced during the growth phase occur in association with the same T_c range that –CGs are associated with during the maximum production.

The sprite observation period was 0323-0856 UT, and sprites were recorded from 0428 UT to 0829 UT. Figure 3.2c shows that during the period of most intense sprite activity, between 0545 UT and 0615 UT, sprites concentrated over regions with $T_c \geq -70^{\circ}$ C, in particular -65° C $\leq T_c \leq -63^{\circ}$ C (0615 UT). The peak in sprite activity (from 0545 UT to 0615 UT) occurred during the period when the -CGs occurrence rate reached a maximum associated with minimum T_c (-72° C $\leq T_c \leq -69^{\circ}$ C). Even though sprites are predominantly generated by +CGs [*Boccipio et al.*, 1995; *Lyons*, 1996, *Cummer and*

Inan, 1997; *Bell et al.*, 1998; *São Sabbas*, 2002a], this result shows that the total −CG activity is tightly correlated with sprite activity. Whether the total −CG activity plays a role in determining the sprite occurrence rate, or this result reflects a particular characteristic of the specific thunderstorm studied, is presently unknown.

(a)   (b)

(c)   (d)
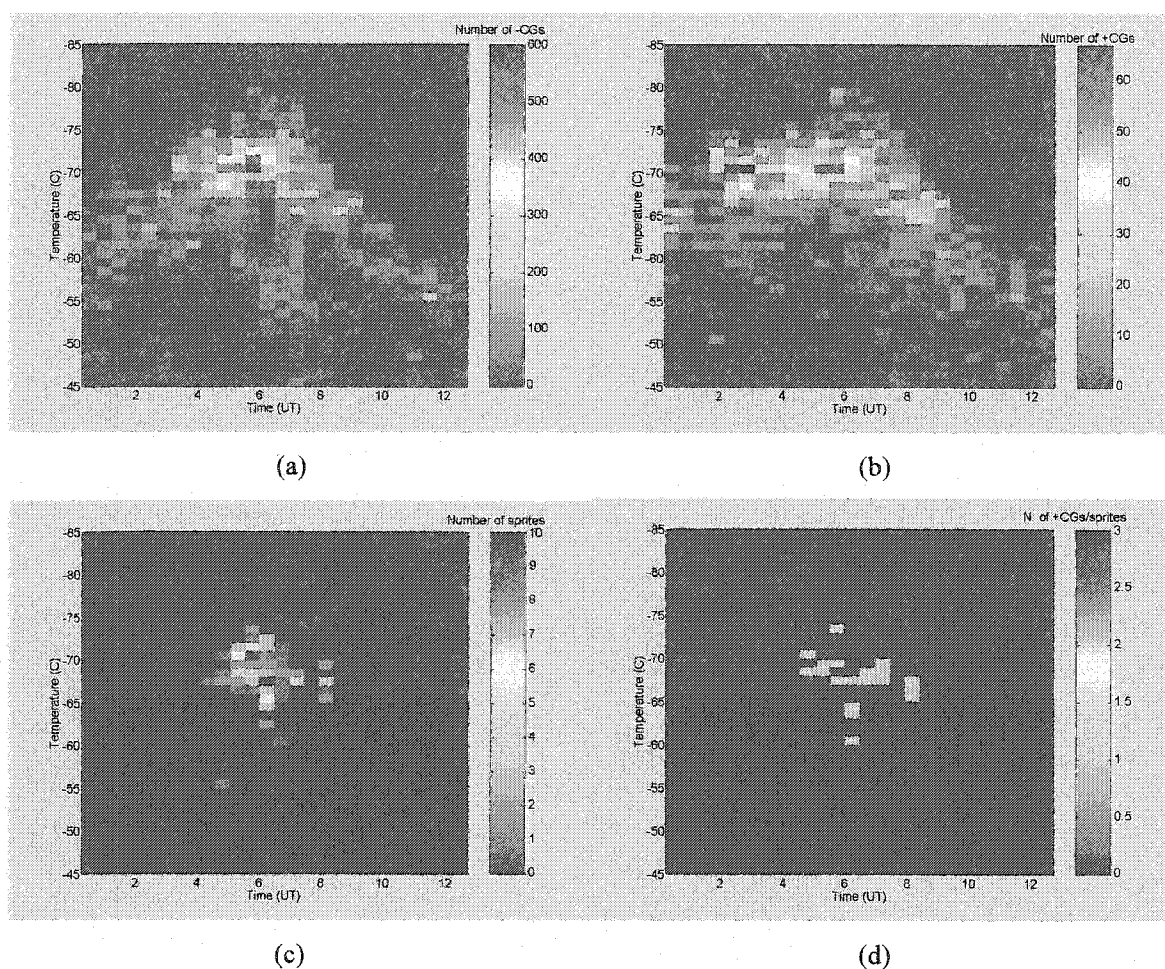
Figure 3.2 Cloudtop temperatures, lightning and sprites. Temporal development of the relationship between GOES-8 IR cloudtop temperatures and the occurrence rate of lightning discharges and sprites throughout the lifetime of the thunderstorm. Each pixel is 30 min by 1^0 C, such that each column is the temperature histogram of number of lightning (or sprites). The thunderstorm growth phase is 0015 − 0545 UT. Panel (a) is the temperature-time diagram for −CGs, (b) is for +CGs, (c) is for sprites, and (d) is for sprite producing +CGs.

The rate of occurrence of sprite generating +CGs remains associated with approximately constant T_c (Figure 3.2d), following the behavior of the total +CGs rate (Figure 3.2d). The difference is that the distribution of the sprite-generating +CGs (Figure

3.2d) is centered between $-67°$ and $-69°$ C, about 2-3° C warmer than for +CGs taken as a whole (Figure 3.2b). The bulk of +CGs of the storm tend to occur in the strong convective regions associated with the coldest cloudtop temperatures, while sprite producing lightning tend to occur in warmer stratiform regions.

The development of the thunderstorm area is shown in the last row of Figure 3.3 together with the sprite, +CG, -CG and total +/-CG occurrence rates during the lifetime of the thunderstorm. The sprite producing storm is "born" between 0045 and 0115 UT, as a result of the coalescence of two relatively small thunder cells (not shown). At 0115 UT it satisfies the Maddox initiation criteria for MCCs (cf. Table 3.1). The storm grows until 0545 UT when the region with contiguous cloudtop with $T \leq -52°$ C reaches the maximum area of $\sim140\times10^3$ km^2, after which the storm starts to decay, even as the total area of the thunderstorm, as defined by the warmer $T_c \leq -32°$ C, continues to expand. The maximum extent (cf. Table 3.1) of the storm $\sim2.32\times10^5$ km^2 is reached at 0745 UT. The eccentricity of the storm at this point is less than 0.7, so this MCS cannot be classified as an MCC according to the Maddox criteria (cf. Table 3.1). The MCS terminates at 1015 UT.

The ~9 hr lifetime of the system studied here is lower than the 14.3 hr mean MCCs duration reported by *Goodman and MacGorman* [1986] in a study of 10 MCCs over the Midwest US. During these ~9 hr a total of 40605 cloud-to-ground flashes were produced, of which 10.9% (4412) were +CGs and 89.1% (36193) were -CGs. The average flash rate of 75.2 min^{-1} was more than 2 times greater than the maximum 32.7 min^{-1} average flash rate reported by *Goodman and MacGorman* [1986].
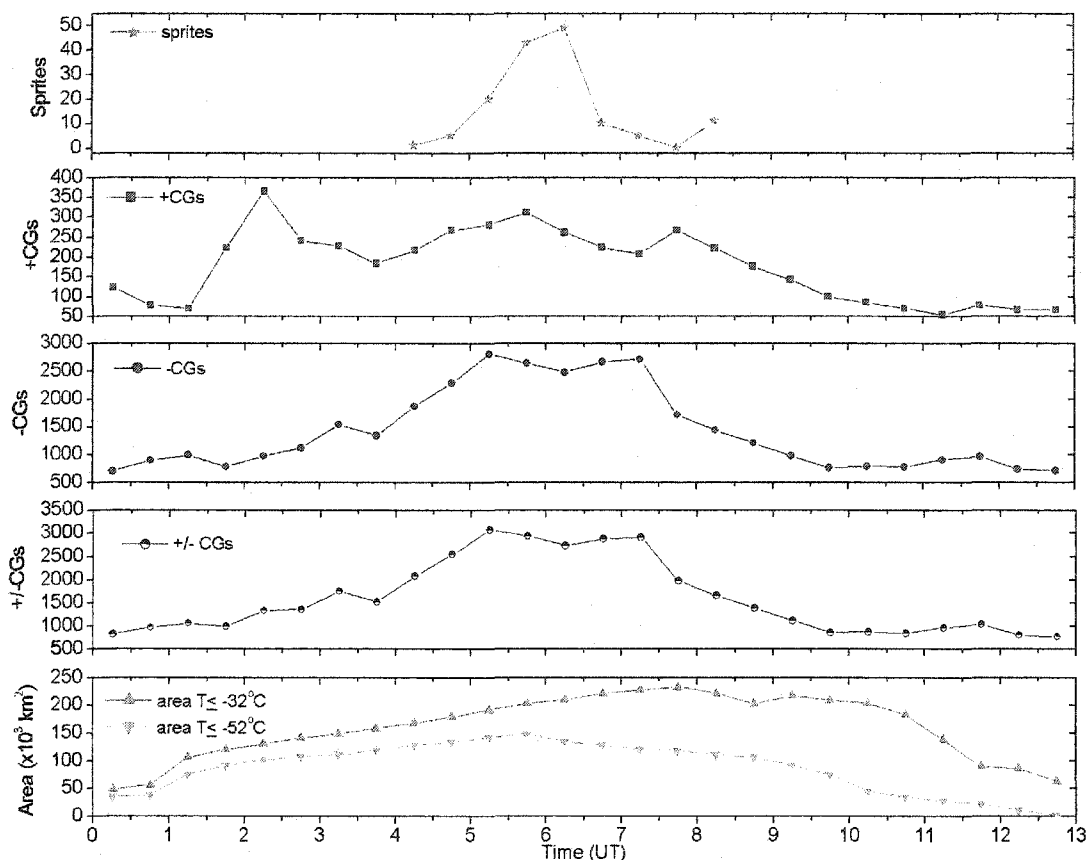
Figure 3.3. Temporal development of thunderstorm parameters. The first row shows sprite rate, the second row shows +CG rate, the third row shows -CG rate, and the last row shows contiguous area of cloud cover with $T_c \leq -32°$ C and $T_c \leq -52°$ C, during the thunderstorm lifetime. All rates were calculated using 30 min intervals.

Figure 3.3 shows that the maximum production of sprites, from 0545 UT to 0615 UT, occurs at the time of maximum area of the region of $T \leq -52°$ C, spanning the transition between growing and decaying phases of the MCS. The same behavior also occurs for the −CG (third row) and total (+/-) CG (fourth row) occurrence rate. The +CG rate (second row) remains high during this period (>170 flashes/30 min), with a relative maximum, but its absolute maximum occurs at 0215 UT, approximately 1 hr after merging of the two cells that originate the MCS. The total +/-CG occurrence rate peaks ~2hr before maximum extent, agreeing with the 2.6 hr reported by *Goodman and MacGorman* [1986]. By the time of maximum extent of the storm (cf. Table 3.1) the total

+/-CG occurrence rate starts to decrease. *Goodman and MacGorman* [1986] suggest that this occurs because the convective precipitation regions are replaced by widespread stratiform precipitation.

3.4 SUMMARY OF RESULTS

The sprite producing system centered on Kansas the night of 21/22 July 1996 was an MCS that originated from the merging of two thunderstorm cells between 0045 UT and 0115 UT. The total lifetime of the system was ~9h. The MCS moved northeastward and reached a maximum extent of ~2.3×10^5 km^2 at 0745 UT, approximately 6 hr after its initiation. The maximum sprite and –CG production of the system were simultaneously achieved at the time of maximum contiguous cloud cover of the coldest region with $T_c \leq$ -52° C, ~ 2 hr before the system reached its maximum extent. The –CG rate increased during the growth phase of the thunderstorm in association with decreasing T_c, it reached a maximum associated with the coldest T_c (-72° C $\leq T_c \leq$ -69° C), and then, in the decay phase of the MCS, it decreased in association with increasing T_c. This suggests that the total –CG activity and dynamical development of the thunderstorm may be more tightly correlated with sprite activity than has previously been reported. The +CG rate remained high during the sprite-recording period (above 170 flashes/30 min), and remained associated with approximately constant T_c (-72° C $\leq T_c \leq$ -69° C, same as -CGs) while the system was growing, subsequently decreasing with increasing T_c during the decay phase. Sprite-generating +CGs occurred in regions about 2-3° C warmer than the bulk population of +CGs.

The techniques reported here to correlate sprite occurrence with the spatial and temporal topology of cloudtop temperatures are the initial steps towards developing a robust methodology based on satellite imagery that could be used to study sprite-generating thunderstorms wherever they might occur in the world. The present analysis was for a single storm. To be most useful and to bound the variance of the results, additional studies would need to be made across many thunderstorms and a variety of latitudes, longitudes and seasons. Candidate regions and satellites suitable for such

studies include South America (GOES-8; *Velasco and Fritsch* [1987]), equatorial and Southern mid-latitude Africa (Meteosat-7; *Fuellekrug et al.* [2001]) and South-, Southeast Asia, and the Malay Archipelago (GMS-5 and InSat; *Sentman and São Sabbas*, [2001]).

CHAPTER 4

CONDUCTIVITY INHOMOGENEITES AS A DETERMINING FACTOR FOR SPRITE INITIATION AND LOCATION

4.1 MOTIVATION

When a sufficiently strong electric field is applied to a nonconducting medium, like air, the medium becomes conducting. This transformation is defined as electric breakdown and is generally accompanied by a flash [*Raizer*, 1991]. Sprites are the "flashes" observed when the mesosphere breaks down under the influence of the electric field produced by lightning discharges. Most sprites occur in groups of several units [*Sentman et al.* 1995a] laterally displaced from the underlying lightning source by several tens of km [*Wescott et al.*, 1998b, 2001; *São Sabbas et al.*, 2003a]. A computed distribution of lateral offsets based on triangulated observations is presented in Figure 2.4. This distribution cannot be explained by any of the current sprite models based on laminar atmospheric density and conductivity profiles. These models predict that breakdown and therefore sprites will occur directly above the generating cloud-to-ground lightning discharge, in contrast to what is observed.

The quasi-electrostatic field induced in the atmosphere by lightning discharges is strongly dependent on the ambient conductivity, and vice-versa. In the presence of an electric field greater than ~ 0.05 % of the breakdown field substantial electron heating occurs, which results in a local modification of the electrical conductivity. Under these conditions Ohm's law relating current density J to the electric field becomes nonlinear, $J = \sigma(E)E$. In a laminar atmosphere, all parameters describing the gas are a function only of altitude, and the field maximizes directly above the region where the charge has been removed. If the atmospheric conductivity is spatially structured, the resultant electric field reflects the structure, exhibiting local maximums above the breakdown threshold in regions that are laterally displaced from the underling lightning.

The atmospheric conductivity has an ion and an electron component. The nighttime electron component is negligible below ~60 km, where the atmosphere is basically neutral, and becomes dominant above that altitude [*Pasko et al.*, 1997b]. Spatial structure in the neutral density affects both the ion and electron component of the conductivity. The ion component is directly affected, since in the highly collisional environment below ~100 km altitude, the effects of the magnetic field are negligible and the massive ions move with the neutrals. Figure 4.1 shows an atmospheric conductivity profile between ~20 km and ~75 km altitude, mainly due to ions, above an isolated thunderstorm with heavy precipitation, experimentally measured by *Holzworth et al.* [1985]. Figure 4.1 also shows conductivity measurements reported by *Maynard et al.* [1981].
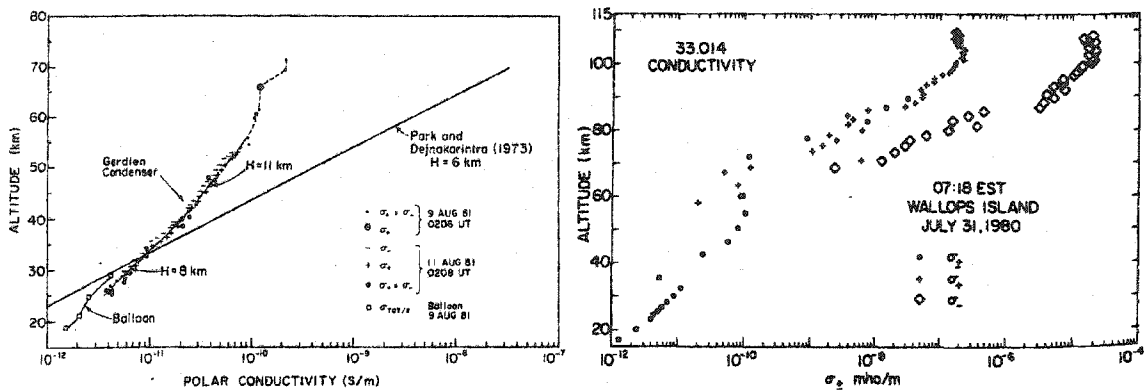
Figure 4.1 Gerdien condensers conductivity measurements from two rocket experiments. The left panel is from *Holzworth et al.* [1985] and the right panel is after *Maynard et al.* [1981].

The electron component of the conductivity (Equation (4.1)) is indirectly affected through changes in the electron mobility due to inhomogeneities in the electron-neutral collision frequency, which depends on the particle number density.

$$\sigma_e = e\mu_e n_e = \frac{e^2 n_e}{m v_m}, \qquad v_m = N\, v_{th}\, \sigma_c\, (1 - <\cos\theta>), \tag{4.1}$$

where e is the electron charge, m is the electron mass, $\mu_e = e/m v_m$ is the mobility, n_e is the electron density, v_m is the effective collision frequency for momentum transfer, N is the

density of the gas, v_{th} is the thermal velocity (velocity of random motion), σ_c is the cross section of elastic collisions and $<\cos\,\theta>$ is the mean cosine of the scattering angle. For isotropic scattering $<\cos\,\theta> = 0$, and $v_m = N\,v_{th}\,\sigma_c = v_c$, where v_c is the electron collision frequency.

Inhomogeneities in the ion density directly affect the ion component of the conductivity and inhomogeneities in the electron density directly affect the electron component. Inhomogeneities in the electron temperature indirectly affect the electron component of the conductivity through changes in the electron-neutral collision frequency and therefore electron mobility. In order to investigate the effects of an inhomogeneous atmospheric conductivity profile on the sprite generating electric field in the mesosphere, computer simulations of the temporal-spatial evolution of the lightning induced field were performed.

The simulations followed the quasi-electrostatic formulation of *Pasko et al.* [1997b], where the time evolution of the electric field and conductivity are calculated in a self-consistent manner. The nonlinear problem was solved within a region of 90 km distance from the discharge and up to 90 km altitude. Both a laminar and perturbed atmospheric conductivity, due to neutral density inhomogeneities, were used. Random density inhomogeneities were superimposed on the laminar profile to address the general problem independent of particularities of the source of the perturbation, which are outside the scope of this dissertation. Several thunderstorm charge configurations were used for the lightning discharge. Here, the results of the perturbed case are compared to the laminar case, and the latter is compared to the results of *Pasko et al.* [1997b]. The objective was to investigate whether a perturbed atmospheric conductivity background could account for the multiple occurrences of sprites and their lateral displacement from the generating lightning.

4.2 CHARACTERIZATION OF NEUTRAL DENSITY SPATIAL STRUCTURE

Common sources of small scale (<10 km) perturbation in the neutral density of the upper atmosphere are gravity waves and locally generated turbulence. Turbulence in the mesosphere is generally associated with two mechanisms, wind shear instability and breaking gravity waves. Gravity waves transport energy and momentum from the troposphere into the middle and upper atmosphere. They are pressure waves that propagate upward with amplitudes that increase with the inverse square of the density, in the absence of dissipation, in order to conserve their kinetic energy. They affect the temperature structure, the spatial distribution of mixing ratios of the atmospheric gases and the background wind field of this region [*Alexander*, 1996]. Gravity waves are capable of major forcing in the general circulation of the middle atmosphere [*Tsuda and Nishida*, 2000].

Hines [1960] first considered the generation and propagation of gravity waves into the mesospheric region, and estimated a 10% fluctuation at 90 km, and 50-100% fluctuations at 115 km. *Pierce and Coroniti* [1966] considered a mechanism by which gravity waves could be generated specifically by thunderstorms, and *Stull* [1976] extended these ideas to effects from thunderstorm penetration of the tropopause. The gravity waves occur with a wide variety of spatial spectral ranges, from quasi-monochromatic wave trains, to small-scale turbulence structures arising from wave breaking. *Fritts* [1984] reviewed gravity wave saturation in the middle atmosphere, and *Walterscheid and Schubert* [1990] reviewed the processes leading to overturning and gravity waves and creation of turbulence. More recent observations described latter in this section are used to characterize the turbulence model in the simulations.

If the amplitude of a gravity wave grows large enough that the temperature perturbation becomes superadiabatic, the wave becomes unstable and "breaks" [*Brasseur and Solomon*, 1986]. Atmospheric conditions strongly affect the wave propagation. For instance, when the wave phase speed equals that of the zonal background wind the wave

is absorbed. The level at which this occurs is referred to as the critical level. The wave can also be reflected at the altitude where its frequency equals the buoyancy, or Brunt-Väissälä, frequency [*Brasseur and Solomon*, 1986].

Observations verify that gravity waves are generated both by surface winds interacting with orographic features and by thunderstorms, and may penetrate to mesopause altitudes. *Larsen et al.* [1982] have observed gravity waves generated by thunderstorms using a radar. Perturbations in OH nightglow due to gravity waves have been reported [e.g., *Krassovsky*, 1972; *Taylor and Hapgood*, 1988; *Taylor et al.*, 1991; *Turnbull and Lowe*, 1991, and references therein]. *Matthews et al.* [1993] reported vertical displacements 2-3 km in the neutral density at 95 km, corresponding to density variations of 20-30%. Small-scale structures in OH airglow images, attributed to gravity wave modulation, have been reported by *Hecht et al.* [1997] and *Hecht et al.* [2000], and breaking action has been interpreted using the 3-D simulation results of *Fritts et al.* [1997].

The analysis of the latitude/longitude cloudtop temperature map of the thunderstorm generating the sprites studied in this work, described in Chapter 3, revealed the complex temporal dynamics of the spatial structure of the top of the thundercloud, associated with the convective activity inside the thunderstorm. Thunderstorm convective activity is a source of short period gravity waves. To date, however, in only a few studies has the source of specific gravity wave features observed in the nightglow been precisely identified [*Taylor and Hapgood*, 1988, *Medeiros*, 2001; *Sentman et al.*, 2003]. A good example of gravity wave effects on the mesosphere is shown in Figure 4.2. The circular wave pattern was observed in OH simultaneously with sprites above a thunderstorm [*Sentman et al.*, 2003]. The patterns in the OH emissions were probably related to gravity waves. The waves and the sprites are likely to have been produced by the same thunderstorm.
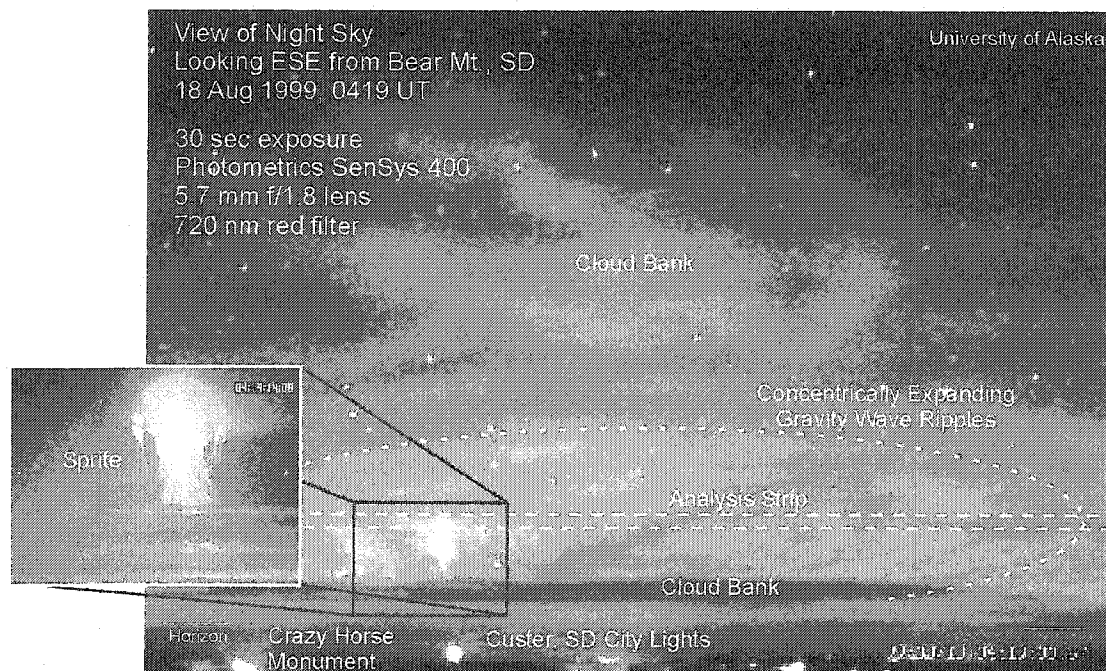
Figure 4.2 Circular wave pattern observed in OH probably due to gravity waves. The pattern was observed above a sprite-producing thunderstorm. The sprite on the main image is shown in the inset in more detail as recorded by a separate ICCD camera. The image was recorded using 25 sec time exposure with a NIR filter during the Sprites99 campaign [*Sentman et al*, 2003].

Small scale breaking of gravity waves has also been observed in OH airglow [*Yamada et al.*, 2001]. Figure 4.3 from *Yamada et al.* [2001] shows an example of gravity wave breaking of ~27 km dominant wavelength to turbulent scale sizes <10 km. The basic photochemistry of this region is reviewed by *Sentman et al.*, [2003] and *Liu and Swenson* [2003]. At lower altitudes, gravity wave perturbations have been observed in stratospheric CO_2 medium infrared emissions [e.g., *Dewan et al.*, 1998; *Picard et al.*, 1998].
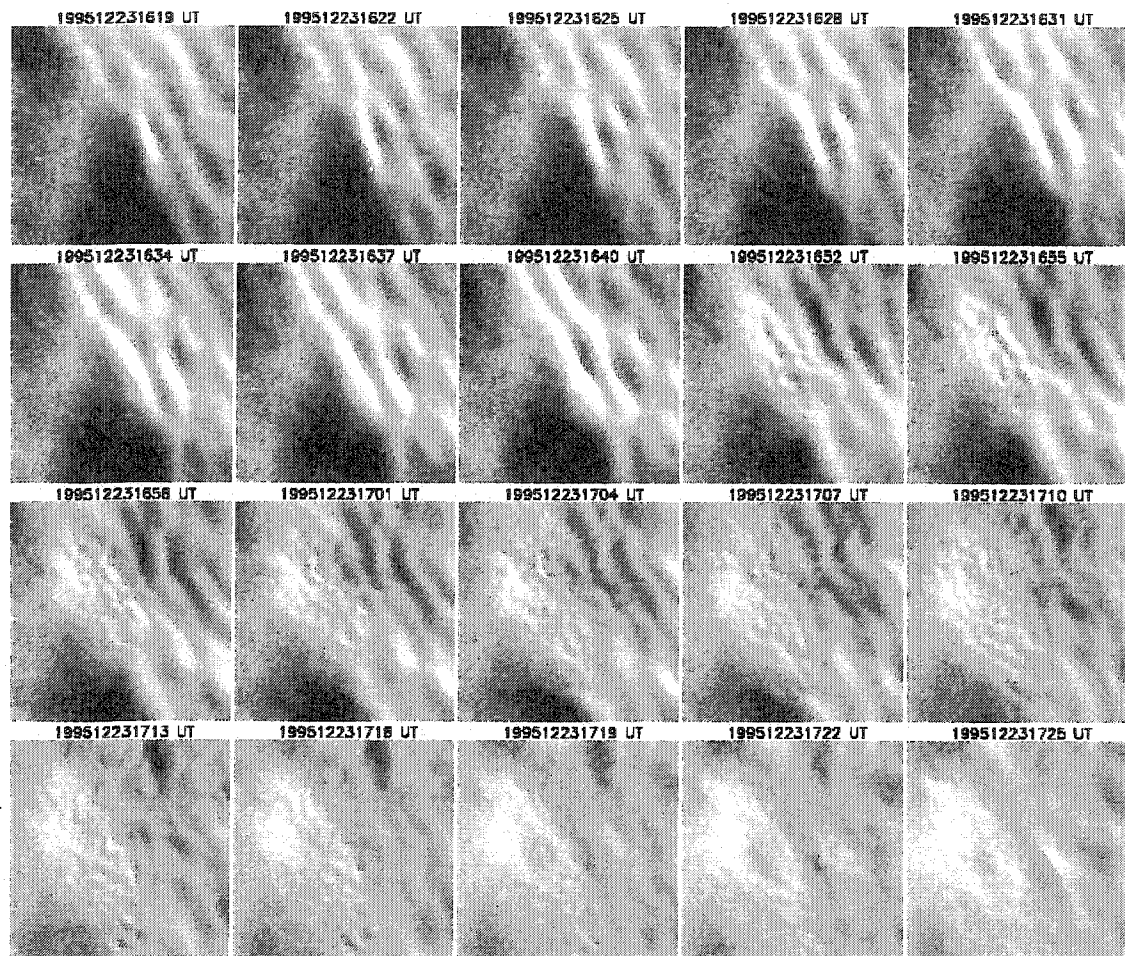
Figure 4.3 Time sequence of OH airglow images. The sequence span the period of 1619-1725 UT on December 23, 1995. The last four digits at top of each image give universal time. The image area is approximately 180 x 180 km at 87 km [*Yamada et al.*, 2001].

Lübken et al. [2002] performed rocket measurements in northern Norway and Sweden to investigate the possible relationship between polar mesosphere summer echoes (PMSC) and neutral air turbulence. It was found that there was a significant amount of turbulence at the mesopause, but it was uncorrelated with the occurrence of PMSCs. Figure 4.4 from *Lübken et al.* [2002] shows a range of spatial inhomogeneities in the temperature of the polar mesosphere. The vertical temperature profiles across the mesopause were obtained during the rocket flights. The measured root-mean-square

(rms) turbulence levels ranged from 5-20 K about the mean. In adiabatic processes, fluctuations in the temperature are related to fluctuations in the neutral density by

$$\frac{dT}{T} = (\gamma - 1)\frac{dn}{n} = \frac{2}{5}\frac{dn}{n},$$ (4.2)

where $\gamma = 7/5$ is the specific heat ratio for a diatomic gas. However, one of the conclusions of *Lübken et al.* [2002] was that the turbulence was not adiabatic. The turbulence extended across a vertical layer of thickness 5-10 km centered on the mesopause at ~85 km. No information was provided about horizontal turbulence, i.e., whether the turbulence was isotropic.

Other studies have revealed the occurrence of mesospheric bores [*Dewan and Picard*, 1998, 2001] and overturning or convective roll cells near the mesosphere [*Larsen et al.*, 2003]. These types of perturbations possess long horizontal extensions, and are qualitatively different from the turbulence cited in previous studies. Thus, the temperature/density of the mesosphere in the region of the mesopause appears to posses a variety of inhomogeneous structures that are highly variable over a wide variety of latitudes and local times, with amplitudes up to several tens percent, and scale sizes that range from a few- to a few-tens of km.
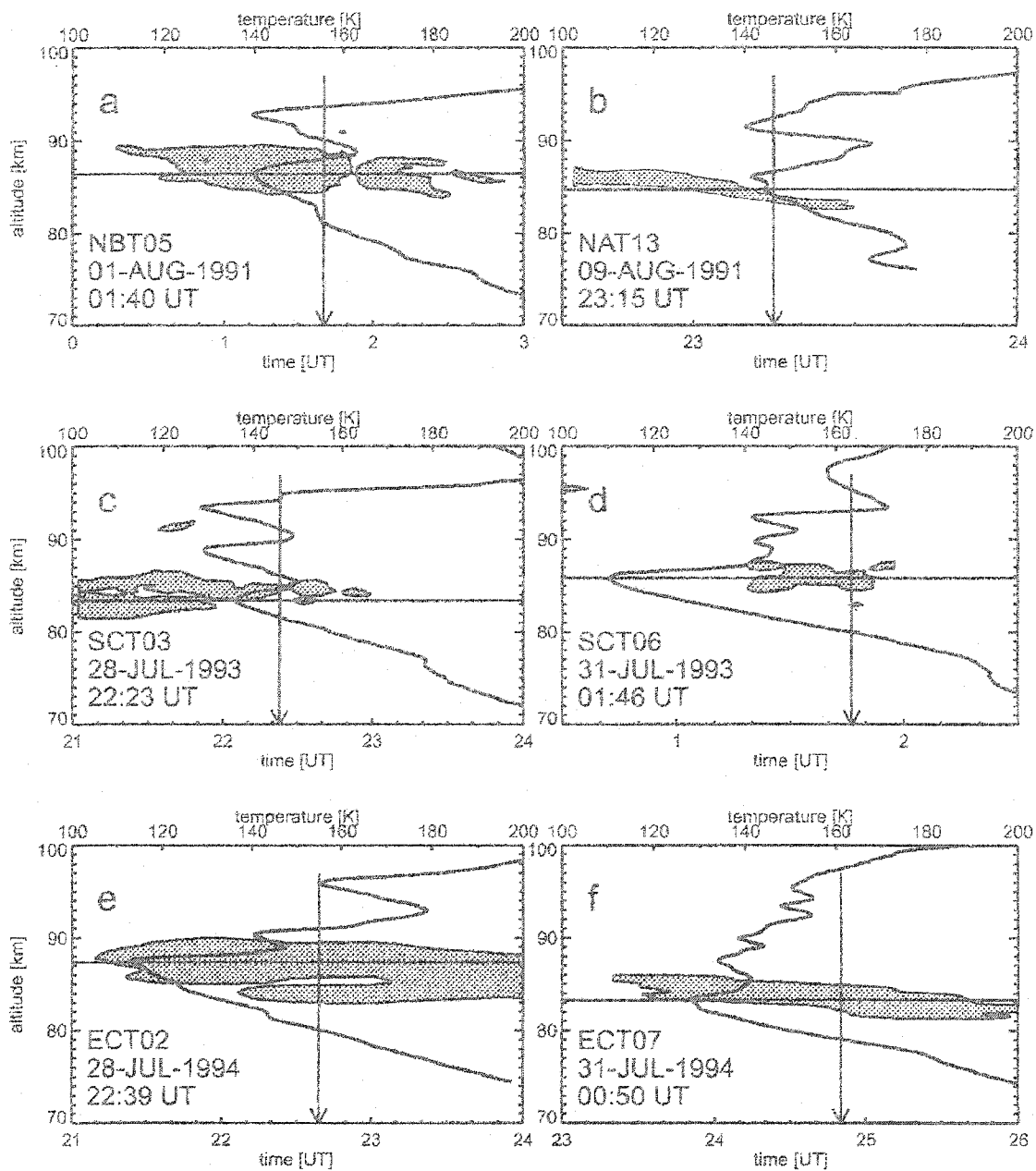
Figure 4.4 Vertical temperature profiles in the vicinity of the polar summer mesopause. The panels illustrate vertical structure in this region; the shaded areas are polar mesosphere summer echoes [*Lübken et al.*, 2002].

4.3 BACKGROUND PHYSICS FORMULATION

During the development of a thunderstorm, strong updrafts and downdrafts take place inside the clouds. These drafts generate charge separation in the ice particles and water droplets that form the clouds, through collisional (and other not well understood) processes that have a complicated dependence on the local temperature. These charged particles form the complex charge structure of thunderstorms, generally approximated as an "inverted dipole," with the positive charge center lying above the negative. Simultaneously, polarization charges of opposite polarity are induced in the surrounding atmosphere due to the finite vertical conductivity gradient, shielding the thunderstorm electric field at high altitudes (Figure 4.5).
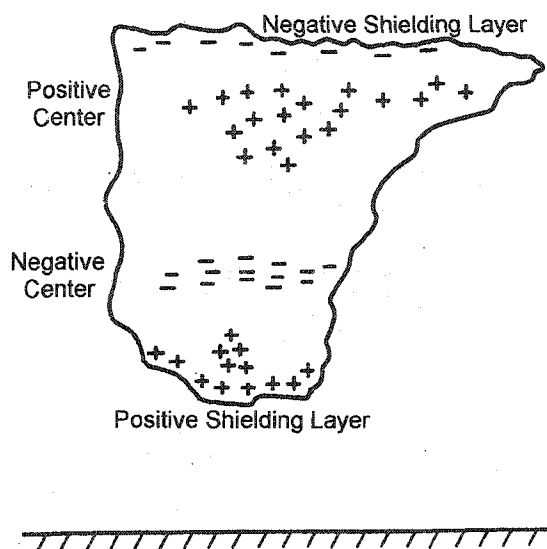
Figure 4.5 Inverted dipole model of thunderstorm. (Adapted from *Pinto Jr. and Pinto* [1996])

When a lightning discharge occurs, it produces a transient electric field that has a rapidly varying component of short duration, an electromagnetic pulse (EMP) produced by the return stroke current, and a slowly varying component with long duration, i.e., the quasi-electrostatic field produced by the removal of the thundercloud charge. The EMP propagates at speeds close to the speed of light, passing too quickly through the mesosphere to produce an appreciable effect in the highly collisional environment. They

are, however, the source of elves (Figure 1.3, center), outwardly expanding ring shaped optical emissions excited in the ionosphere at ~100 km [*Fukunishi et al.*, 1996a,b].

It has been shown that the quasi-electrostatic approximation is adequate to account for the characteristics of sprites [*Pasko et al.*, 1997b]. The quasi-electrostatic approximation involves assuming the electric field can be written solely in terms of a scalar potential function $\mathbf{E} = -\nabla \varphi$, where electric displacement effects are ignored. Conduction currents are related to the electric field via Ohm's law $\mathbf{J} = \sigma \mathbf{E}$, where the conductivity σ is assumed to be a scalar quantity. The simulations involved solving the coupled Gauss law

$$\nabla \cdot \mathbf{E} = \frac{(\rho_0 + \rho_1)}{\varepsilon_0} \tag{4.3}$$

and the continuity equation

$$\frac{\partial(\rho_0 + \rho_1)}{\partial t} + \nabla \cdot (\mathbf{J}_0 + \mathbf{J}_1) = 0, \tag{4.4}$$

where the subscripts 0 and 1 indicate the source, or thunderstorm, and induced, or atmospheric quantities, respectively.

The quasi-electrostatic component of the field may generate sprites at the locations where it exceeds the breakdown threshold [*Pasko et al.*, 1997b]

$$E_k = 3.2 \times 10^6 \frac{N_0}{N} \text{ V/m}, \tag{4.5}$$

where E_k is the characteristic air breakdown field, N_0 is the neutral density on the ground and N is the density profile. E_k (Figure 4.6) is determined by the relation between creation and removal of electrons, i.e. ionization, attachment, and less effectively, recombination. Electron impact ionization is the most important charge generation mechanism in a gas discharge. Other less effective ionization mechanisms are photoionization, which provide seed electrons that start avalanches in streamer propagation, ionization by resonance-

excited species, and associative ionization [*Raizer*, 1991]. The rate of impact ionization in the absence of losses is characterized by the ionization frequency v_i (Equation (4.6))
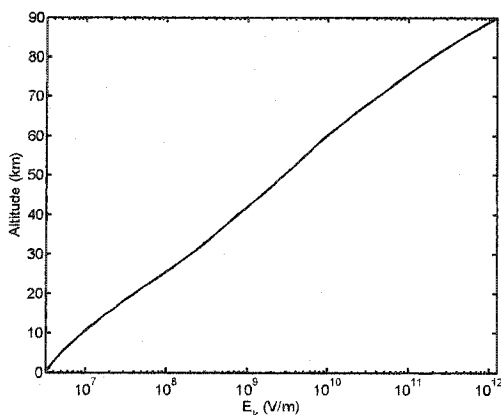
Figure 4.6 Breakdown electric field as a function of altitude.

$$\left.\frac{dn_e}{dt}\right|_i = v_i n_e, \qquad v_i = N\frac{\int n(\varepsilon)v\sigma_i(\varepsilon)d\varepsilon}{\int n(\varepsilon)d\varepsilon}, \tag{4.6}$$

where $n(\varepsilon)$ is the electron energy distribution function (density normalized), $\sigma_i(\varepsilon)$ is the ionization cross section of gas species in ground state and v is the velocity of the electron. The electron impact cross sections for the two major constituents of the atmosphere, molecular nitrogen (~78%) and molecular oxygen (~22%), are shown in Figure 4.7.
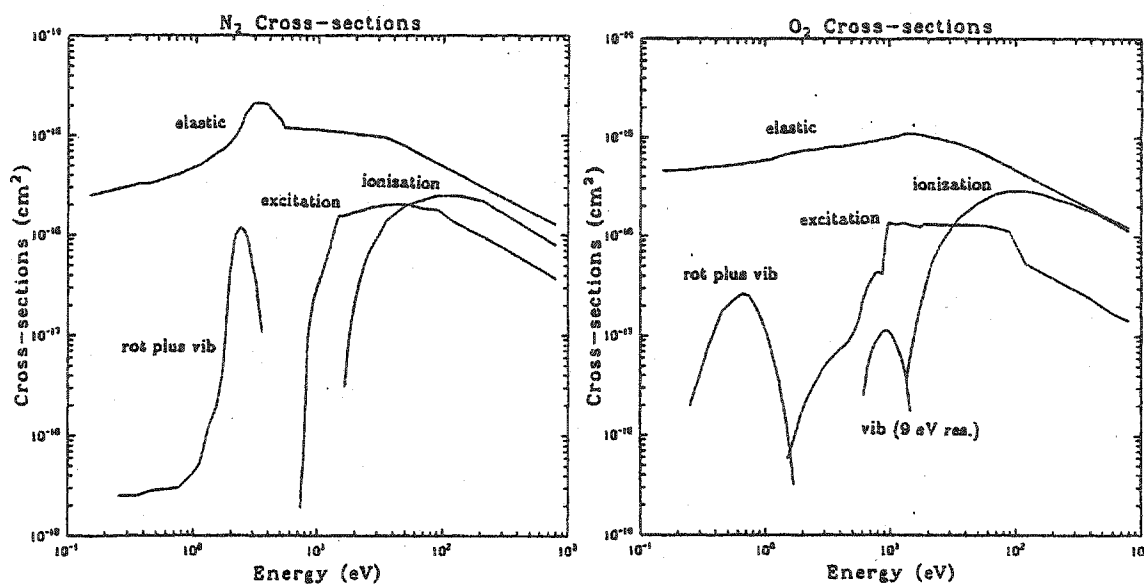
Figure 4.7 Cross sections of N_2 (left), and O_2 (right) as a function of energy. [*Lummerzheim*, 1987]

The recombination rate in a plasma without electronegative components, and in the absence of an electric field, follows

$$\frac{dn_e}{dt}\bigg|_r = -\beta n_e n_+ , \qquad n_e = \frac{n_e^0}{1+\beta n_e^0 t}, \tag{4.7}$$

where β is the electron-ion recombination coefficient, n_+ is the density of positive ions, and n_e^0 is the initial electron density. Recombination is a less effective electron removal mechanism than attachment, since it is proportional to the electron density squared [*Raizer*, 1991], and will not be considered in this work.

In the mesosphere, attachment is the main loss mechanism for electrons. Molecular oxygen, the second major constituent of the atmosphere, is a major sink of electrons in the mesosphere, since the dominant attachment reactions in this region are dissociative attachment of O_2 and a three-body reaction involving O_2:

$$e^- + O_2 \rightarrow O + O^- \tag{4.8}$$

$$e^- + O_2 + M \rightarrow O_2^- + M . \tag{4.9}$$

The total change in electron density is then given by

$$\frac{dn_e}{dt} = (v_i - v_a)n_e, \tag{4.10}$$

where v_a is the attachment frequency. Experimentally, what one actually measures in a dc electric field are the ionization and attachment coefficients, α and a respectively, which are the ionization/attachment per unit length along the field ($\alpha = v_i/v$, $a = v_a/v$, c.f. *Raizer* [1991]).

As mentioned previously, the mesosphere and lower ionosphere are weakly ionized collisional media. In such a collisional regime, the conductivity, electron mobility, electron density, ionization and attachment frequencies, depend nonlinearly on the electric field. The *Pasko et al.* [1997b] quasi-electrostatic model for sprite production treats the nonlinear effects using a self-consistent calculation of the conductivity and electric field. The heating of the local electrons strongly modifies the conductivity above ~60 km where the electron component of the conductivity is dominant; below that altitude the changes in the conductivity are negligible since the ions are not significantly heated by the electric field. *Pasko et al.* [1997b] takes into account the effects of the electric field on the conductivity through changes in the mobility μ_e due to heating and changes in the electron density n_e due to ionization and attachment processes. The simulations performed in this study follows the *Pasko et al.* [1997b] self-consistent formulation as described in the next section.

4.4 DESCRIPTION OF THE SIMULATIONS

The objective of the simulations was to investigate whether inhomogeneities in the atmospheric conductivity can be the cause of multiple sprites occurring due to a single lightning stroke, and possessing lateral displacement from the generating discharge. The simulations followed the spatial-temporal evolution of the lightning induced quasi-electrostatic field ($\mathbf{E} = -\nabla\phi$) in a laminar and perturbed atmosphere. It was terminated when all the thundercloud charge associated with the lightning was

discharged. The simulations involved solving Equations (4.3) and (4.4) rewritten as a function of the potential

$$\nabla^2 \phi = -\frac{\rho_{tot}}{\varepsilon_0}, \quad \rho_{tot} = \rho_0 + \rho_I \tag{4.11}$$

$$\frac{\partial \rho_{tot}}{\partial t} = \nabla \sigma \cdot \nabla \phi - \frac{\sigma \rho_{tot}}{\varepsilon_0} \tag{4.12}$$

The problem was solved in two dimensions (2-D) using cylindrical geometry (r, z) with axial symmetry (Figure 4.8). The computation domain was a square region of 90 km with grid elements, dr and dz of 1 km. The time steps, Δt, were taken to be one half the shortest relaxation time ($\tau = \varepsilon_0/\sigma$) of the system, which occurs at 90 km altitude, i.e., $\Delta t = \tau_{90\ km}/2$.
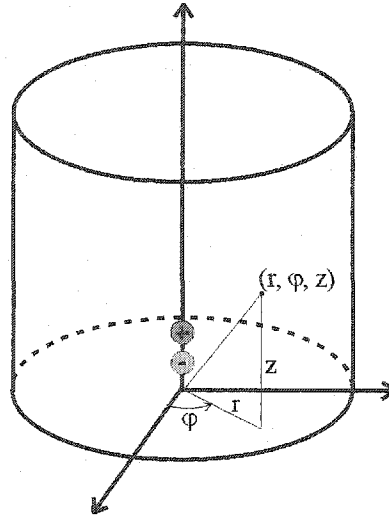
Figure 4.8 Coordinate system used in the simulations. Boundary condition is $\partial \phi/\partial r = 0$ at all boundaries.

In cylindrical coordinates Poisson's equation is

$$\nabla^2 \phi = \frac{\partial^2}{\partial^2 z} \phi + \left(\frac{\partial^2}{\partial r^2} + \frac{1}{r} \frac{\partial}{\partial r} \right) \phi = -\frac{\rho_{tot}}{\varepsilon_0} \tag{4.13}$$

The radial and vertical differential operators were discretized into matrix operators using second order forms from *Abramowitz and Stegun* [1962], so that Poisson's equation may be written

$$\mathbf{L}_z \varphi + \varphi \mathbf{L}_r = -\frac{1}{\varepsilon_0} \rho_{tot} . \qquad (4.14)$$

Here the vertical component of the Laplacian ($\mathbf{L}_z$) is a left matrix operator and the radial component ($\mathbf{L}_r$) is a right matrix operator. Letting $\mathbf{X} = \varphi$, $\mathbf{A} = \mathbf{L}_z$, $\mathbf{B} = \mathbf{L}_r$, and $\mathbf{C} = -(1/\varepsilon_0)\rho_{tot}$ be the respective parameter matrices and matrix operators, the matrix form of the Poisson's equation may be written in the standard form for Sylvester's equation

$$\mathbf{AX} + \mathbf{XB} = \mathbf{C} . \qquad (4.15)$$

The boundary conditions were set in the first and last rows of the matrix operators. The ground ($z = 0$ km) and ionospheric ($z = 90$ km) boundaries were assumed to be perfect conductors and Dirichlet's boundary condition ($\partial \varphi / \partial r = 0$) was applied, making the electric field perpendicular to these boundaries. Neumann's boundary condition ($\partial \varphi / \partial r = 0$) was applied along the z-axis ($r = 0$ km) and at the cylindrical boundary ($r = 90$ km), making the field parallel to the boundary (i.e., vertical). The cylindrical boundary condition can in principle be set as $\partial \varphi / \partial z = 0$ or as $\partial \varphi / \partial r = 0$. Both of these conditions lead to unphysical modifications near to the boundary, but the spatial-temporal evolution of the electric field does not depend significantly on the edge fields since the boundary is far enough from the charge source. *Pasko et al.* [1997b] have set the cylindrical boundary at $r = 60$ km in his simulations, as a trade off between computer resources available at the time and the accuracy, and showed that these boundary conditions lead to an error of $< 10\%$ on the magnitude of the field at $r = 50$ km and $z = 10$ km.

Poisson's equation in the form of Sylvester's equation (4.15) was solved at each time step using the method of Schur decomposition [*Bartels and Stewart*, 1972]. The

other equations were discretized using the method of first finite differences [*Fletcher*, 1990].

The thunderstorm charge centers were modeled as Gaussians having the total charge (Q_+), center altitude (z_+), and 1/e widths (z_a and r_a) as free parameters (Equation (4.16)). The charge centers were placed along the z-axis.

$$\rho_0 = \rho_+ + \rho_-, \quad \rho_\pm = \frac{Q_\pm}{V} \exp\left[-\left(\frac{z - z_\pm}{z_a} \right)^2 + \left(\frac{r}{r_a} \right)^2 \right] \tag{4.16}$$

where ρ_+ and ρ_- are the positive and negative charge densities respectively and V is the normalization parameter applied to yield a total charge equal $Q_\pm$.

The laminar neutral density profile (Figure 4.9) was obtained from the MSIS-E-90 model for 22 July, 1996, latitude 37.5° N, longitude 99.0° W, and 6 UT as input parameters. This configuration approximately corresponds to the location of the sprite producing region of the thunderstorm studied, during the period of high lightning and sprite activity studied in Chapters 2 and 3.
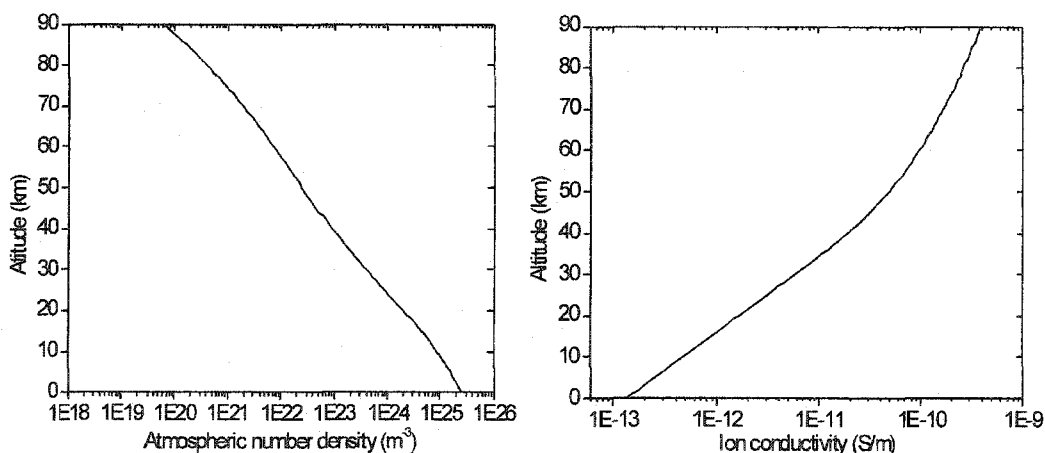
Figure 4.9 Neutral density (left) and ion conductivity (right) profiles. The neutral density was obtained from the MSIS-E-90 model for input parameters date = July 22, 1996, lat. = 37.5° N, lon. = 99.0° W, and time = 6 UT. The ion conductivity was modeled after *Holzworth et al.* [1985].

The laminar conductivity profile (Figure 4.11) was calculated as a sum of the ion and electron components. The ion component (Figure 4.9) was adapted from *Holzworth et al.*, [1985] and the electron component was calculated using

$$\sigma_e = e n_e \mu_e. \tag{4.17}$$

The electron density profile of the bottom of the nighttime ionospheric D/E region (Figure 4.11) used in the calculation of the electron component of the conductivity was modeled after Chapman's theory

$$n_{e,Chap} = n_{e,\max} e^{\left[0.5*\left(1-Z-e^{-Z}\right)\right]}, \qquad Z = \frac{z - z_{\max}}{H_0}, \tag{4.18}$$

where $n_{e,max}$ is the maximum electron density, z_{max} is the altitude of maximum electron density, and H_0 is the scale height of the layer. All those quantities are free parameters that may be adjusted to model a wide variety of profiles.

The altitude of maximum electron density was set as 100 km. The other two free parameters were carefully chosen (Table 4.1) in order to construct a conductivity profile that would best fit the midlatitude conductivity profile measured by *Maynard et al.* [1981] (Figure 4.1), without inducing electric breakdown when a 50 C positive charge center was completely discharged. This laminar conductivity profile (σ_A) and thunderstorm charge configuration $Q_\pm = \pm 50$ C constituted the control case against which all other cases spanning the explored parameter space were compared. The right panel of Figure 4.10 shows a comparison between the conductivity data ($\sigma_{Maynard}$), the control conductivity (σ_A), a conductivity profile calculated using the electron distribution provided by the IRI model (σ_{IRI}) for the same input parameters used in the MSIS-E-90 model, and a conductivity profile using the same H_0 and z_{max} as σ_A and $n_{e,max} = 2 \times 10^9$ m^{-3} (σ_{2e9}), extracted from Rees [1989]. The left panel of Figure 4.10 shows the electron density profile used to calculate the electron component of the conductivities σ_A, σ_{IRI}, σ_{2e9}. This figure illustrates the large variability of electron density and conductivity that may occur in the atmosphere.
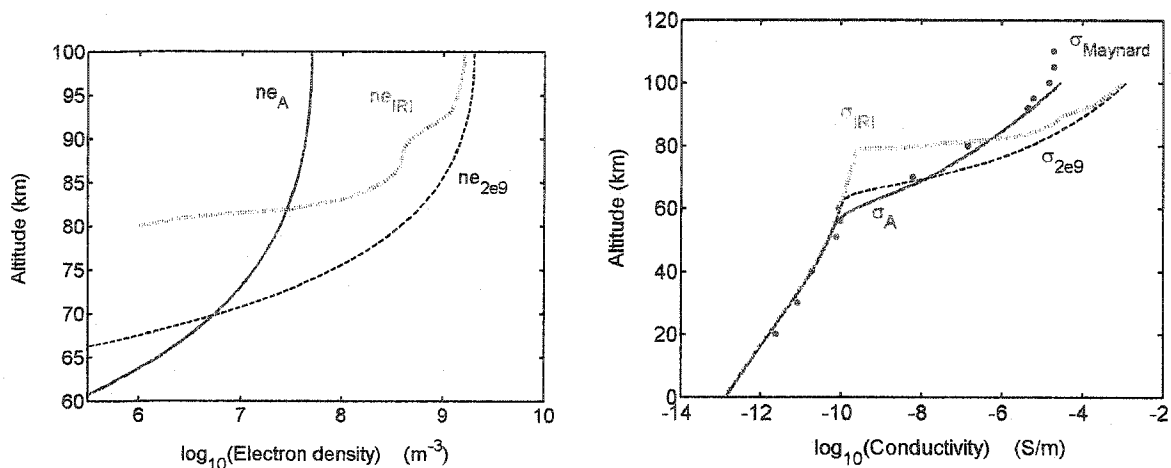
Figure 4.10 Comparison of several electron densities (left) and conductivities. $\sigma_{Maynard}$ is the conductivity data extracted from *Maynard et al.* [1981]. σ_A is the control conductivity, σ_{IRI} is a conductivity profile calculated using the electron distribution provided by the IRI model σ_{IRI}, and σ_{2e9} is a conductivity profile calculated using the same H_0 and z_{max} as σ_A and $n_{e,max} = 2 \times 10^9$ m^{-3}. n_{eA}, n_{eIRI}, and n_{e2e9} the electron density profiles used to calculate σ_A, σ_{IRI}, σ_{2e9}.

4.4.1 PRE-LIGHTNING CONFIGURATION

The first step in the simulations was to calculate the electric field and induced charge in the laminar atmosphere due to the presence of the thunderstorm, before the lightning discharge, i.e., the pre-lightning configuration. Since the time scale of thunderstorm development, of the order of hours, is much larger than the electric relaxation time over all altitudes, in the pre-lightning configuration the atmosphere would have relaxed over all altitudes. The relaxation time decreases with altitude, therefore the top of the system relaxes first and the relaxation level moves downwards with time, i.e., the so called "moving capacitor model" of *Greifinger and Greifinger* [1976]. In these simulations, due to computational limitations, the atmosphere was allowed to relax only down to 50 km altitude. The simulations are therefore valid for altitudes above 50 km.

Also due to the long charge build up time, no self-consistent formulation was applied in this part of the simulations. It was assumed that the thunderstorm charges build up slowly enough that the dipolar electric field maintains a linear relationship with the

conductivity, no ionization or attachment is produced and the electrons are not heated. The electron mobility was calculated using the linear expression in Equation (4.22).

Several parameter regimes were selected to provide a variety of atmospheric conditions under which sprites may occur. Two laminar conductivity profiles, the control conductivity and a variation of that with reduced $n_{e,max}$ (σ_B), were used. The values chosen for the free parameters of Equation (4.18) generating the electron density profiles used to calculate of the conductivities are shown in Table 4.1. The table also shows the resulting maximum ambient conductivity, at 90 km, and the resulting time step. Figure 4.11 shows the electron density profiles calculated using the parameters in Table 4.1 and the conductivity profiles σ_A and σ_B together with the conductivity data $\sigma_{Maynard}$.

Table 4.1 Parameters related to laminar ambient conductivity profiles

Profiles	$n_{e,max}$ (m^{-3})	z_{max} (km)	H_0 (km)	σ_{max} (S/m)	$\Delta t = 0.5*\tau_{90km}$ (s)
σ_A	5×10^7	100	15	3.72×10^{-6}	1.19×10^{-6}
σ_B	1×10^7	100	15	4.45×10^{-7}	5.94×10^{-6}
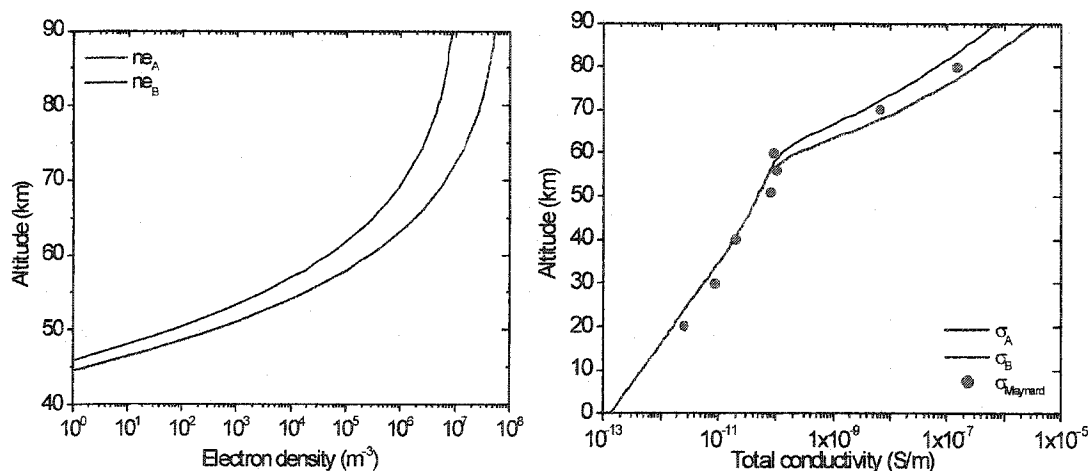
Figure 4.11 Electron densities (left) and conductivities (right) used in the simulations.

For each conductivity profile, three charge configurations ($Q_\pm = \pm 50$ C, $Q_\pm = \pm 100$ C and $Q_\pm = \pm 200$ C) were used to model thunderstorm charge centers. Table 4.2 shows the values utilized for the free parameters of Equation (4.16) determining the

charge density of the thunderstorm. In order to consistently compare results due to different thunderstorm charges, the location of the charge centers and their relative sizes were kept constant; only the total charge amount was varied.

Table 4.2 Charge related parameters

Q_+ (C)	z_+ (km)	r/z_{a+} (km)	Q_- (C)	z_- (km)	r/z_{a-} (km)
50	10	3	-50	5	3
100	10	3	-100	5	3
200	10	3	-200	5	3

A total of six laminar pre-lightning configurations were evaluated. The pre-lightning atmospheric induced charge density (ρ_I), and total electric field (E_{tot}) of the control case ($Q_\pm$ 50 C, first line of Table 4.2, and conductivity σ_A) are shown in Figure 4.12 together with the thunderstorm (ρ_0) and total charge densities (ρ_{tot}), and electric field components (E_r and E_z).

σ$_A$ laminar (Q =50 C)   ρ$_0$ ρ$_1$ ρ$_{tot}$

80

60

40

20

0

E$_r$ E$_z$ E$_{tot}$

80

Altitude (km)   60

40

20

0
  0   20   40   60   80   0   20   40   60   80   0   20   40   60   80
   Radial distance (km)   Radial distance (km)   Radial distance (km)

-1   -0.5   0   0.5   1   -1   -0.5   0   0.5   1
   Charge (C)   x 10^{-12} Electric field (V/m)   x 10^4
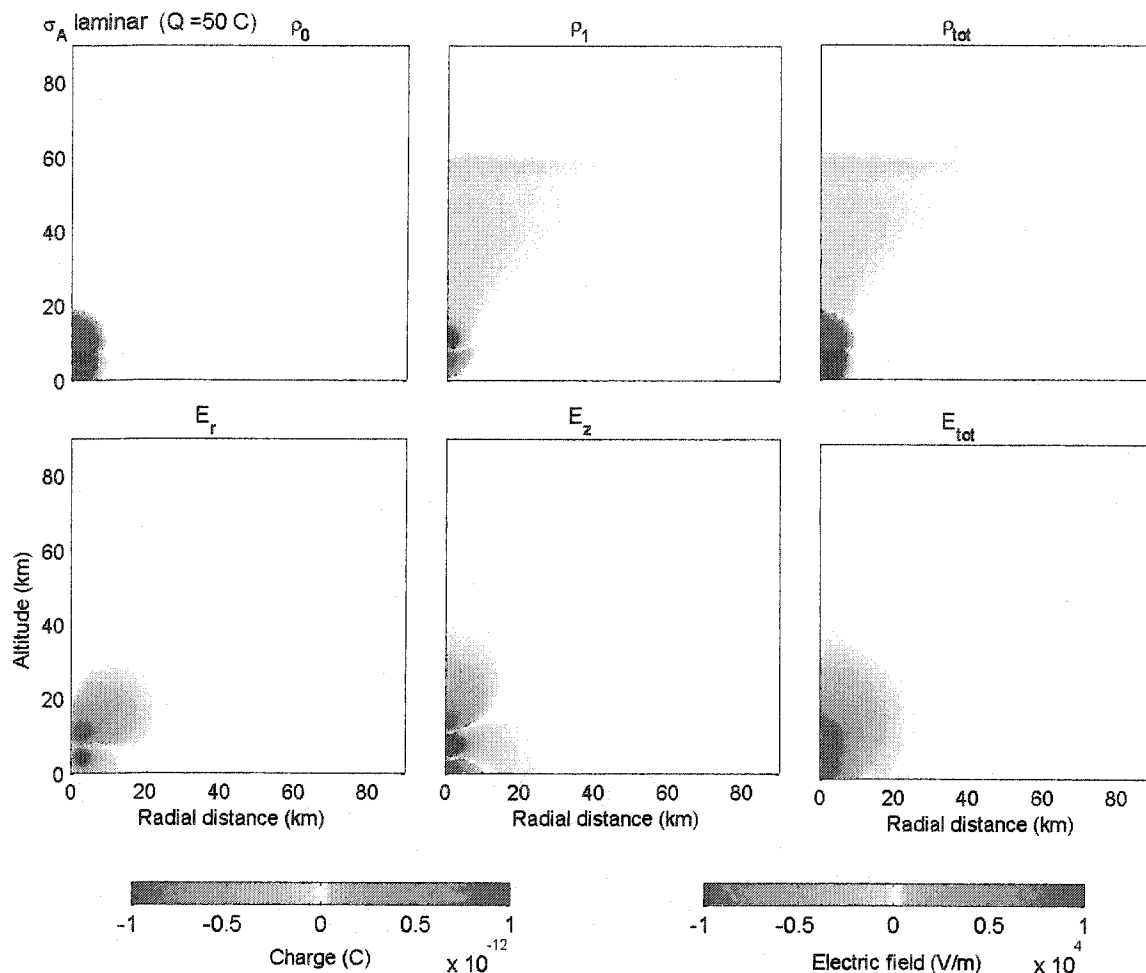
Figure 4.12 Pre-lightning configuration of total charge density for the control case. The first line shows the thundercloud charge density (ρ_0), the charge density induced in the atmosphere (ρ_1), and total charge density (ρ_{tot}), respectively. The second row shows the E_r and E_z components of the electric field, as well as the total field (E_{tot}), respectively. Note that ρ_0, and ρ_1 and ρ_{tot} are saturated below 20 km.

The perturbed, or inhomogeneous, pre-lightning configurations were generated by superimposing six different perturbation patterns of varying amplitude and scale size onto the neutral density profile. The perturbations were mapped to the relevant density dependent quantities (μ_e, n_e, σ, E_{tot}) according to expressions given in Section 4.4.2, previously evaluated for the laminar pre-lightning configuration of the control case. Since the atmosphere has relaxed down to 50 km in the pre-lightning scenario, the electric field is almost totally excluded above that altitude (Figure 4.12) and $E/E_k \sim 0$. Therefore,

superimposing the perturbation patterns on the already calculated laminar pre-lightning configuration produces the same perturbed pre-lightning configurations as if they were initially calculated with the perturbation patterns.

A simple isotropic model characterized by a Gaussian amplitude probability distribution generated by a spatially low pass filtered random number field (Equation (4.19)) was adopted to create smooth perturbation patterns

$$\Delta_{pert}(z,r) = A_{pert} r_{pert}(z,r) \exp[-(z - z_{0,pert})^2 / a_{pert}^2],$$
(4.19)

where A_{pert} is the amplitude of the average perturbation, r_{pert} (z, r) is an uniform random pattern generated to yield a specified standard deviation and isotropic scale size. The exponential factor centers the random pattern at altitude $z_{0,pert}$ with characteristic layer thickness a_{pert}. To generate the random pattern r_{pert} (z, r) of specified scale size $size_{pert}$, a matrix was created and initialized with independent identically distributed white (Gaussian) noise. It was then convolved with a 2-D isotropic Gaussian of width $size_{pert}$, and scaled according to the specified standard deviation.

The perturbation pattern was then superimposed on the ambient background profile by multiplication to produce the spatially structure density field

$$N(z,r) = N_0(z,r)[1 + \Delta_{pert}(z,r)].$$
(4.20)

This perturbation model is sufficiently flexible to permit investigation of the effects of turbulence on sprite initiation over a wide variety of turbulent conditions.

Table 4.3 shows input values for the parameters used in generating the perturbation. Figure 4.13 shows, as an example, the perturbation pattern used for $A_{pert} = 0.3$ and $size_{pert} = 2$ km, as well as the resulting density, mobility and conductivity.

Table 4.3 Parameters related to neutral density perturbations

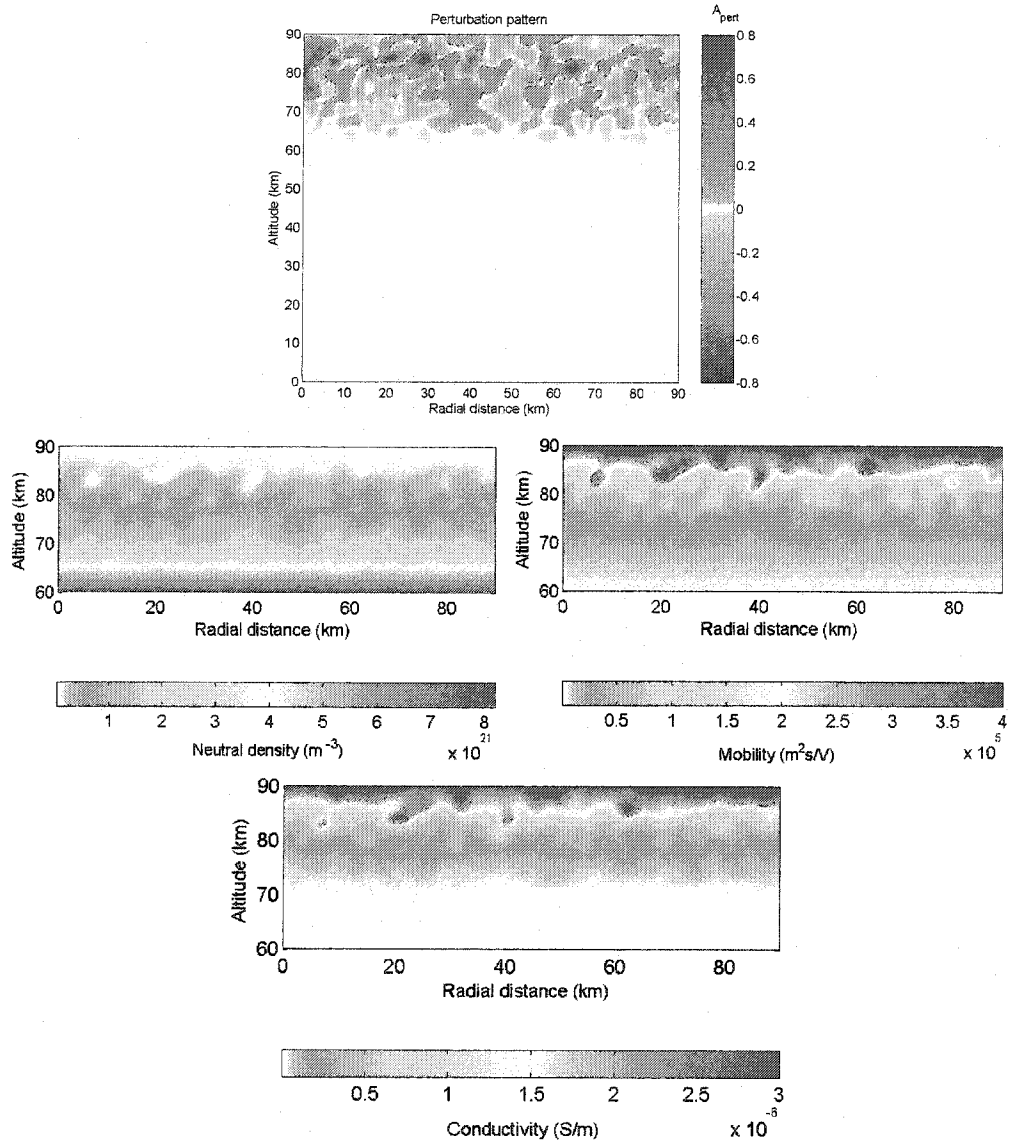| cases	A_{pert}		$size_{pert}$ (km)		$z_{0,pert}$ (km)	a_{pert} (km)
	input	actual	input	actual		
1	0.1	0.0985	2	2.0132	80	10
2	0.2	0.1993	2	2.0397	80	10
3	0.2	0.2065	5	5.0285	80	10
4	0.3	0.2931	2	2.0457	80	10
5	0.3	0.2959	5	5.1943	80	10
6	0.4	0.3971	2	2.0475	80	10
7	0.4	0.3875	5	5.1338	80	10

Figure 4.13 Perturbation pattern and perturbed density, mobility and conductivity. Input parameters are $A_{pert} = 0.3$ and $size_{pert} = 2$ km.

4.4.2 SPACE-TIME EVOLUTION OF LIGHTNING INDUCED ELECTRIC FIELD

After the pre-lightning condition was determined, either laminar or inhomogeneous, a cloud-to-ground discharge of 1 ms (t_{light}) was simulated by removing the charge of the positive/negative charge center adopting the same functional form used by *Pasko et al.* [1997b]

$$\rho_0 = \rho_\mp + \rho_\pm \left[1 - \frac{\tanh(t / t_{light})}{\tanh(1)} \right], \ t \le t_{light}. \tag{4.21}$$

The functional variation for charge removal models the discharge process. The specific form is not critical for the physics of the phenomena modeled [*Pasko et al.*, 1997b], as long as it is monotonically decreasing. The form used here has a characteristic duration of ~300 μs in agreement with observations for positive lightning [*Uman*, 1987].

In these simulations (nonlinear regime) the electric field and conductivity were calculated in a self-consistent manner, after the model of *Pasko et al.* [1997b]. The electron component of the conductivity (Equation (4.17)) was recalculated at each time step to take into account changes in the electron mobility due to heating [*Pasko et al.*, 1997b]

$$\mu_e \ \frac{1}{N} \ 10^{\sum_0^2 a_i x^i}$$

$$\nu_i = \left(\frac{N}{N_0}\right) 10^{\sum_0^3 a_i x^i}, \quad \text{for } \frac{EN_0}{N} \geq 1.122 \times 10^6 \text{ V/m} \tag{4.23}$$

$$\nu_i = 0, \quad \text{for } \frac{EN_0}{N} < 1.122 \times 10^6 \text{ V/m}$$

where $x = \log_{10}\left(\frac{EN_0}{N}\right)$, $a_0 = -624.68$, $a_1 = 249.60$, $a_2 = -32.878$, and $a_3 = 1.4546$.

These ionization rates compare favorably with those given by *Papadopoulos et al.* [1993], and with swarm data [*Dutton*, 1975].

The attachment frequency was calculated using [*Barrington-Leigh et al.*, 2000]:

$$\nu_a = \left(\frac{N}{N_0}\right) 10^{\sum_0^4 a_i x^i}, \quad \frac{EN_0}{N} \geq 3.162 \times 10^5 \text{ V/m} \tag{4.24}$$

$$\nu_a = 0, \quad \text{for } \frac{EN_0}{N} < 3.162 \times 10^5 \text{ V/m}$$

where $x = \log_{10}\left(\frac{EN_0}{N}\right)$, $a_0 = -3567.0$, $a_1 = 1992.68$, $a_2 = -416.601$, $a_3 = 38.7290$, and $a_4 = -1.35113$.

The expressions given above are based on experimental data and on kinetic simulations [*Pasko et al.*, 1997b, and references therein]. Figure 4.14 graphically shows the dependence of the μ_e, ν_i and ν_a on EN_0/N. The self-consistent formulation of this model has the same limitations described in *Pasko et al.* [1997b], and are only valid for $EN_0/N < 1.6 \times 10^7$ V/m, or $E/E_k < 5$. For fields above this value the electron energy approaches the ionization energy and the ionization process becomes nonstationary [*Pasko et al.*, 1997b; *Papadopoulos et al.*, 1993, and references therein]. In this work, $E/E_k < 5$ for all cases studied. A second limitation is that the model is not valid for time scales less than the time required for the establishment of the stationary electron distribution function [*Pasko et al.*, 1997b], estimated as 10μs for an altitude range of 80-90 km [*Taranenko et al.*, 1993].
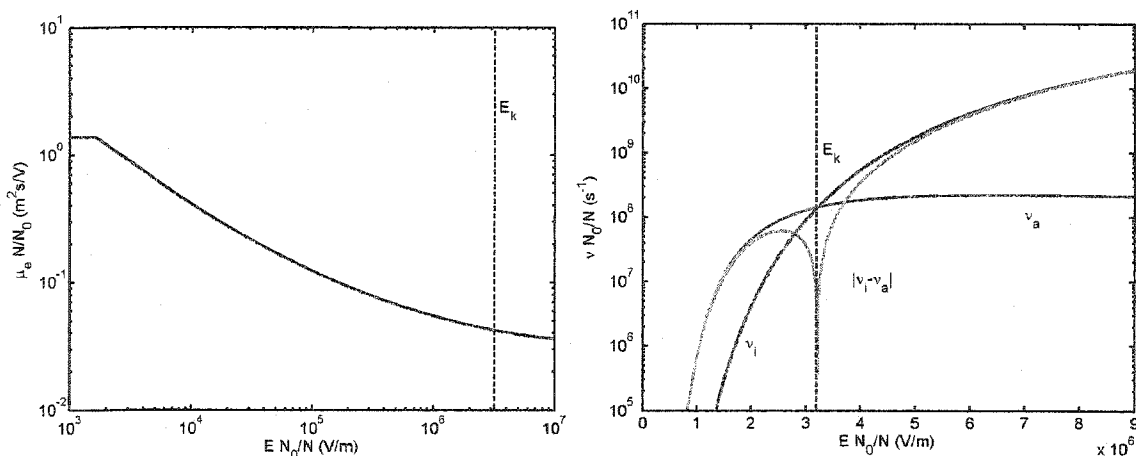
Figure 4.14 Mobility (left) and ionization (right) and attachment frequencies as a function of EN_0/N.

4.4.2.1 LAMINAR CASES

Six different cases were run for a laminar atmosphere. For each conductivity profile, σ_A and σ_B, all three charge configuration were employed. All the results of this dissertation are presented in terms of electron mobility, electron density, conductivity, the ratio E/E_k, and total charge density. They are shown at $t = 0$ ms (before lightning), at the time step in which $E/E_k \geq 1$ for the first time, and at $t = 1$ ms (at the termination of the lightning discharge).

The results at $t = 1$ ms of the control case (σ_A and $Q_\pm = \pm 50$ C) and of the other two cases in which only the thunderstorm charge was varied (σ_A and $Q_\pm = \pm 100$ C, $Q_\pm = \pm 200$ C), were compared with the correspondent results of *Pasko et al.* [1997b]. They are in very good qualitative and reasonable quantitative agreement, with only minor differences due to the fact that different ambient ($t = 0$ ms) conductivity profiles were used in the respective models. Figure 4.15 shows a comparison of vertical profiles of electron density and conductivity at $t = 1$ ms, together with the ambient profiles, taken at $r = 0$ km. For 50 C, attachment dominates at all altitudes and the electron density is slightly reduced in both models compared to the ambient profiles.

The altitude distribution of mobility and electron density are shown in Figure 4.16, Figure 4.18 and Figure 4.20 for the region above 60 km, where modifications from the ambient profiles occur. Figure 4.17, Figure 4.19 and Figure 4.21 show the altitude distribution of conductivity and E/E_k, for the same region. In the control case (Figure 4.16 and Figure 4.17) no breakdown is produced. The mobility and conductivity are reduced by approximately 2 orders of magnitude everywhere above 60 km. Changes in mobility dominate over changes in the electron density in this case, and the conductivity temporal-spatial evolution is determined by the mobility evolution. The electron density is modified by attachment within ~40 km distance in the radial direction.
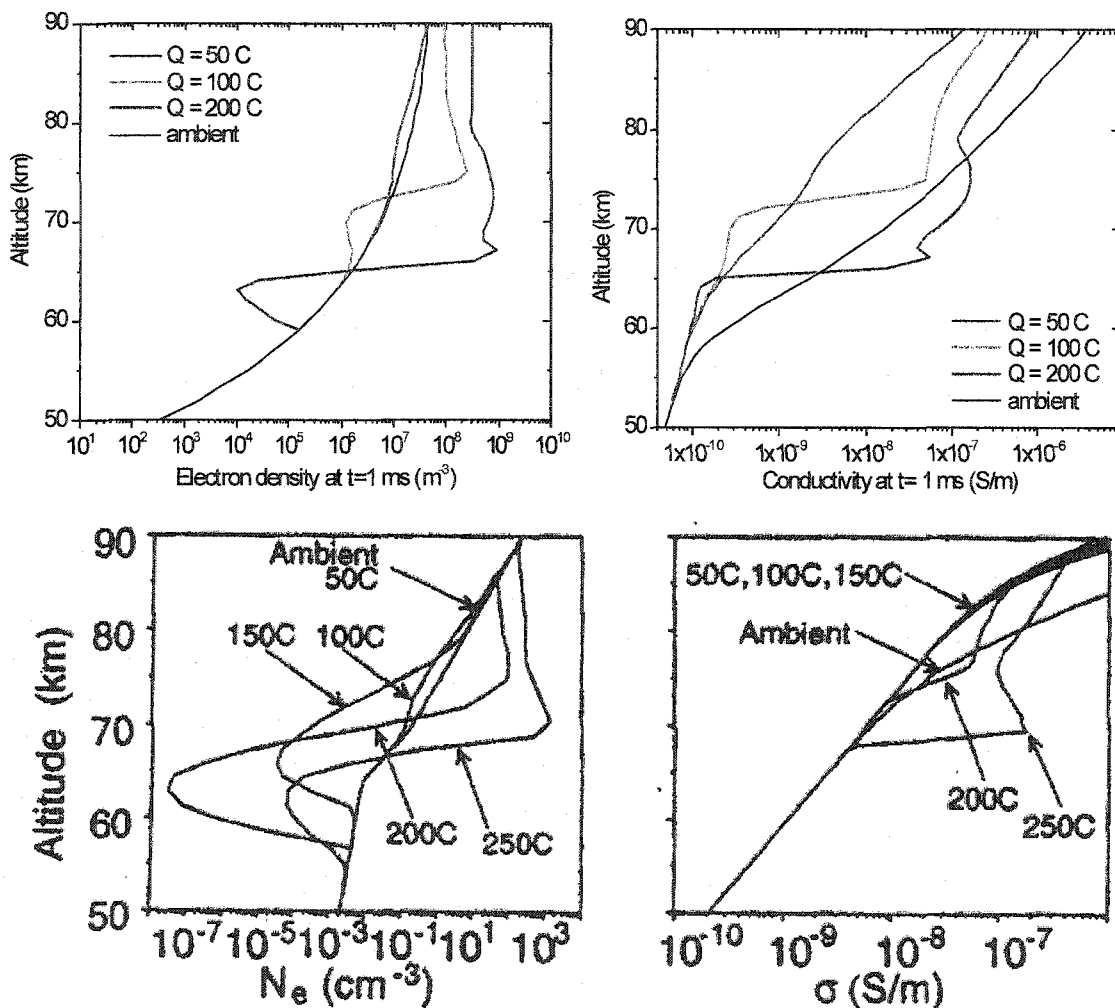
Figure 4.15 Electron density and conductivity for this and *Pasko et al.* [1997b] model. All the results are for the termination of the lightning discharge ($t = 1$ ms). The first row shows results for this model and the second row shows the top row of Figure 12 of *Pasko et al.* [1997b].

Figure 4.16 Electron mobility (left) and electron density (right) for the control case. The first row shows t = 0 ms and the second row shows t = 1 ms. The atmosphere does not breakdown in this case.

Figure 4.17 Conductivity (left) and E_{tot}/E_k, (right) for the control case. The first row shows t = 0 ms and the second row shows t = 1 ms. The atmosphere does not breakdown in this case.

For the cases where $Q_\pm = \pm 100$ C (Figure 4.18 and Figure 4.19) and $Q_\pm = \pm 200$ C (Figure 4.20 and Figure 4.21), the mobility term dominates over the electron density, reducing the conductivity over all altitudes until the electric field reaches the breakdown threshold. Breakdown occurs earlier, and therefore with less charge removal, for the 200 C case than the 100 C case. After that, the electron density term becomes progressively dominant, i.e., ionization progressively dominates over attachment above ~73 km, for 100 C, and above ~65 km, for 200 C, enhancing the conductivity in that region up to $r =$ ~50 km. Below those altitudes, the conductivity is reduced.
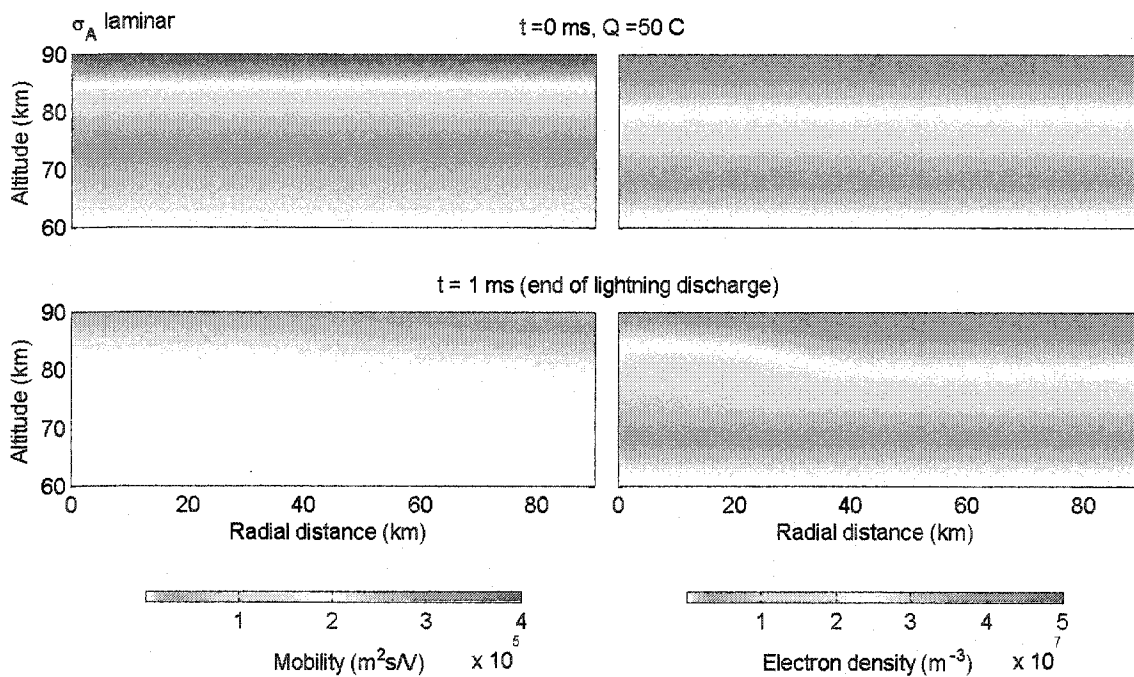

Figure 4.18 Electron mobility (left) and electron density (right) for the 100 C case. The first row shows $t = 0$ ms, the second row shows when $E_{tot} = E_k$ for the first time, and the third row shows $t = 1$ ms. The percentage of the total charge removed (Q_{remov}) and breakdown time are indicated above the middle row panel. The laminar control profile, σ_A, was used.

The other three laminar cases, where the conductivity profile σ_B was used (same charge configurations), qualitatively show behavior similar to that previously described. In general, the greater the charge in the initial configuration, the greater are the changes in the magnitude of the electron mobility, electron density and conductivity, and the earlier the atmosphere breaks down. The main difference between profiles σ_A and σ_B is that breakdown occurs in the 50 C case for profile σ_B, the environment with smaller conductivity has fewer charge carriers to shield the penetration of the electric field. This case is shown in Figures A-1 and A-2 of Appendix A.
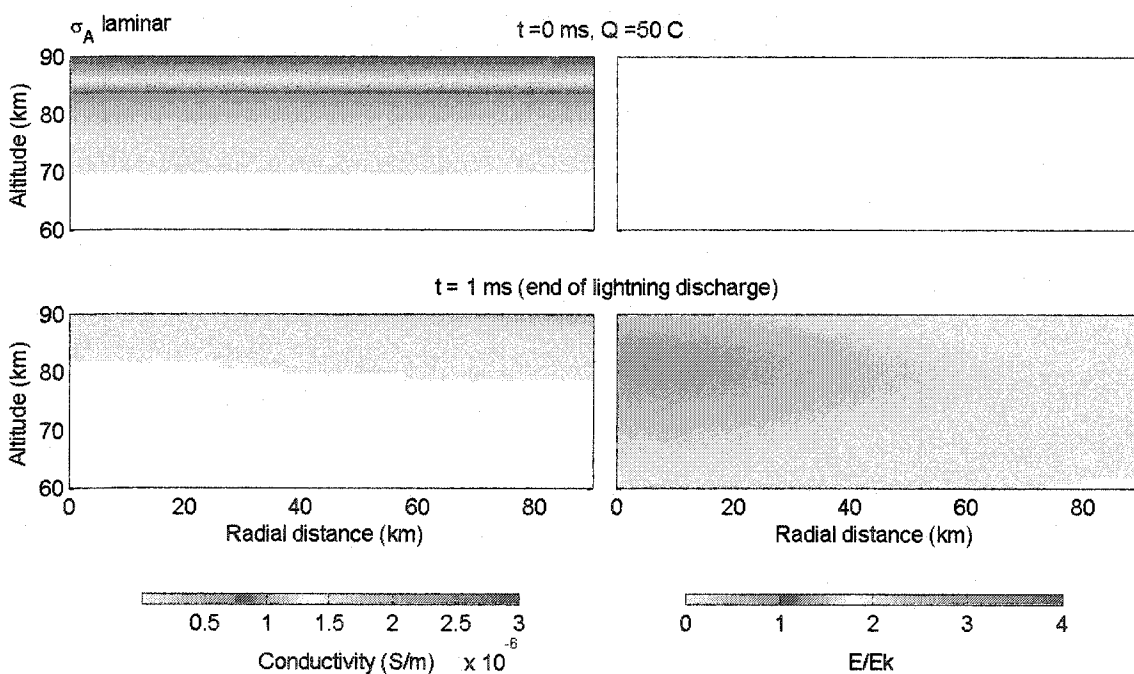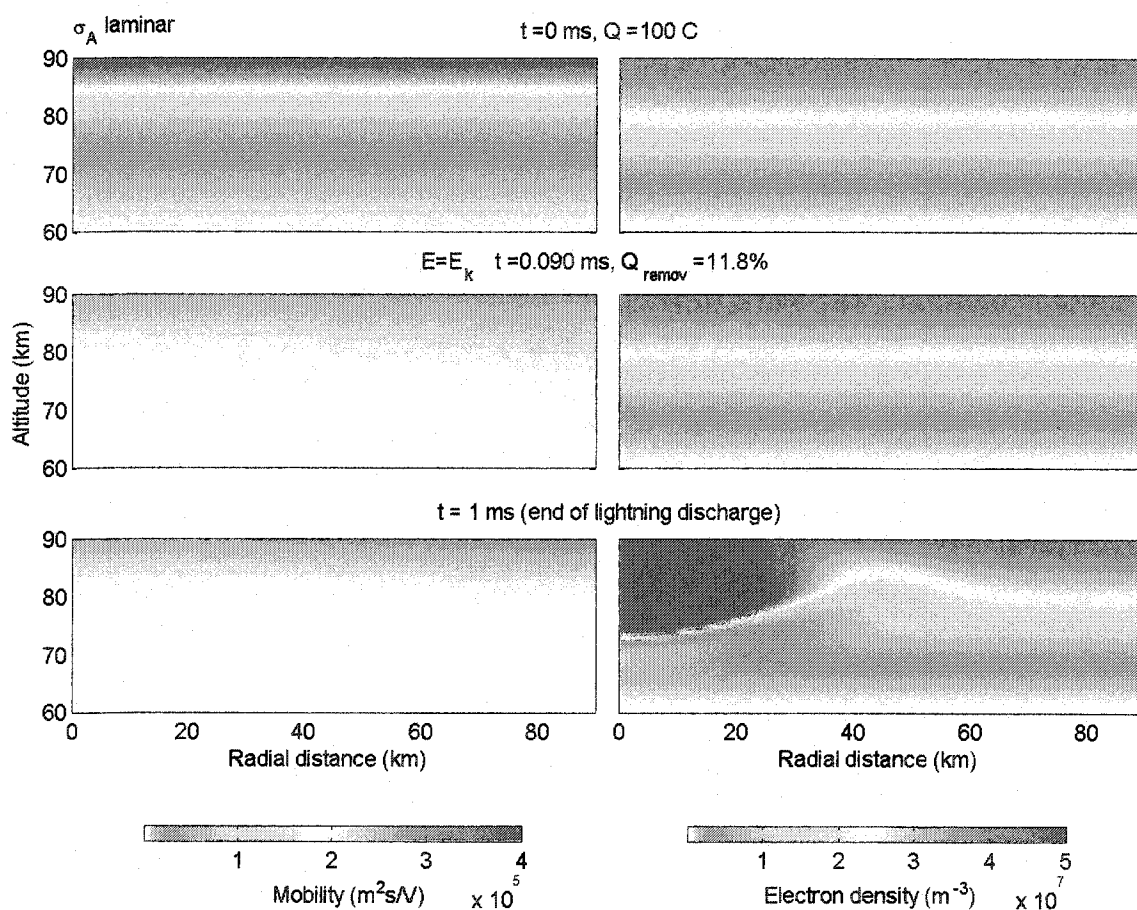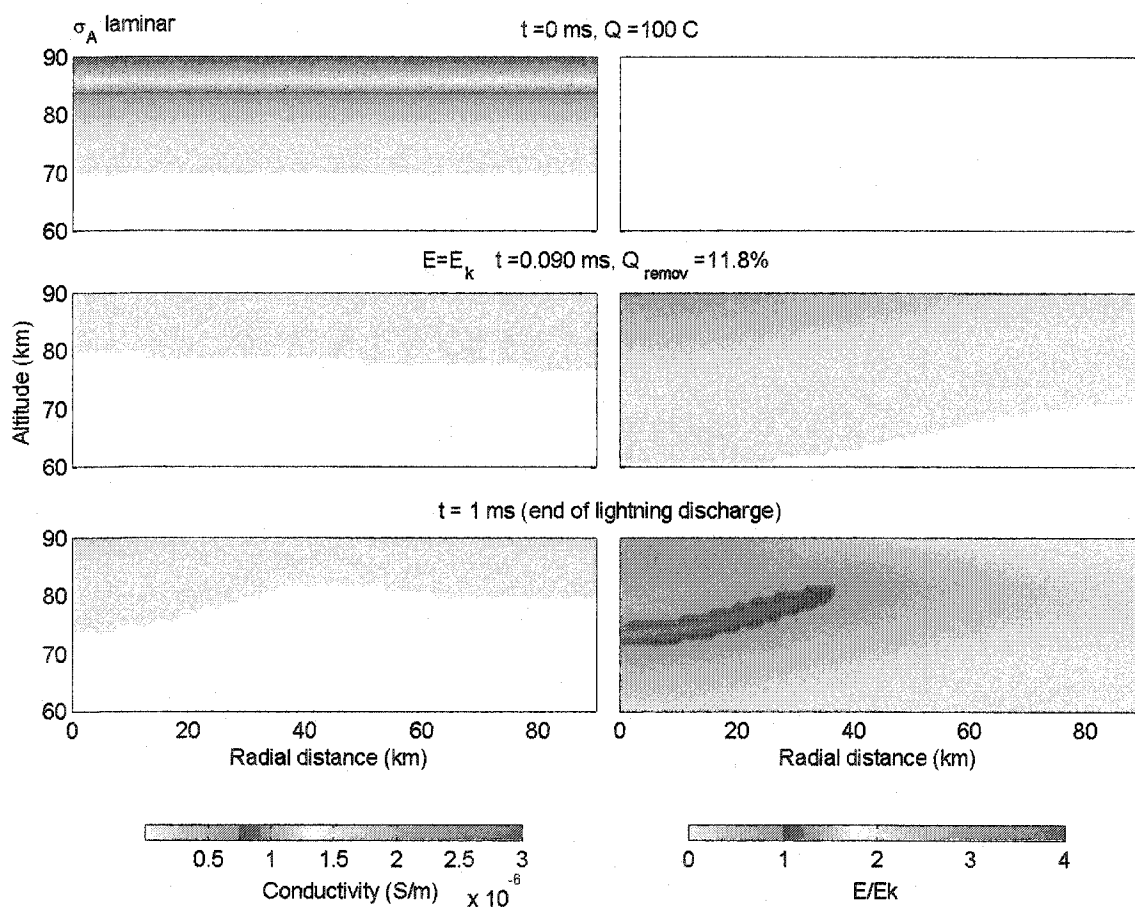

Figure 4.19 Conductivity (left) and E_{tot}/E_k, (right) for the 100 C case. The first row shows $t = 0$ ms, the second row shows when $E_{tot} = E_k$ for the first time, and the third row shows $t = 1$ ms. The percentage of the total charge removed (Q_{remov}) and breakdown time are indicated above the middle row panel. The laminar control profile, σ_A, was used.

In all laminar cases in which the electric field reaches the breakdown threshold, it develops centered on the underling charge, as in other models adopting a laminar description of the atmosphere. The temporal-spatial evolution of the electric field is in good agreement with the evolution of modeled intensity of emissions of the first positive band of N_2 shown in Figure 14 of *Pasko et al.* [1997b], for 250 C. The temporal-spatial evolution of the optical emissions is controlled by the development of ionization and the relatively faster relaxation of the electric field at higher altitudes.

Figure 4.20 Electron mobility (left) and electron density (right) for the 200 C case. The first row shows $t = 0$ ms, the second row shows when $E_{tot} = E_k$ for the first time, and the third row shows $t = 1$ ms. The percentage of the total charge removed (Q_{remov}) and breakdown time are indicated above the middle row panel. The laminar control profile, σ_A, was used.

However, in this model, breakdown first occurs at the ionospheric boundary at 90 km, at the very top "row" of the domain, where the upper boundary is located. This could

be interpreted as the boundary condition (perfect conductor, $\partial\varphi/\partial r = 0$) leading to unrealistic large values of the electric field at the boundary.

Figure 4.22 shows the total charge density in the atmosphere ($\rho_{tot} = \rho_0 + \rho_1$) for the three charge configurations, before the lightning, when the electric field first reaches breakdown, and at the end of the discharge. A layer of positive polarization charge develops above 60 km due to the removal of the positive center of the thunderstorm. The magnitude of this induced charge layer reflects the amount of removed charge. A similar behavior is observed when the conductivity profile B is used (Figure A-3, Appendix A).

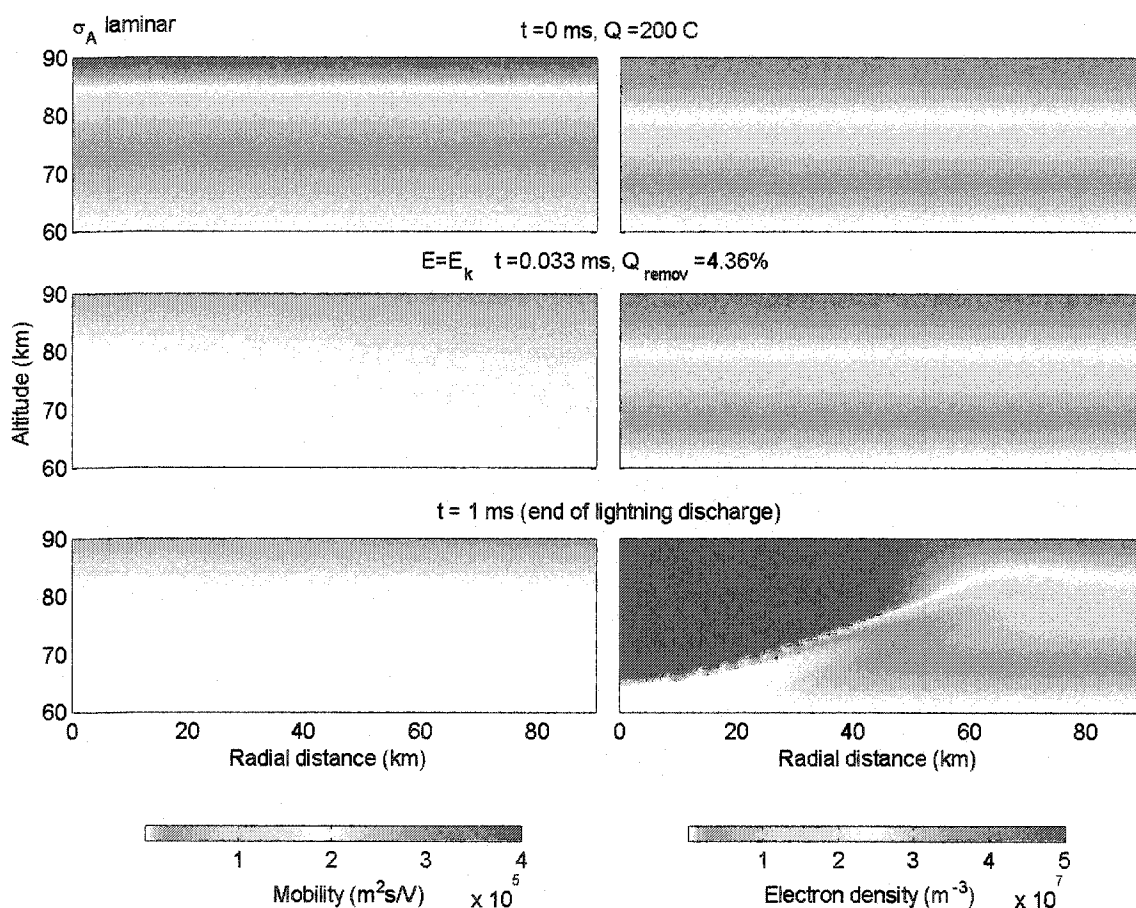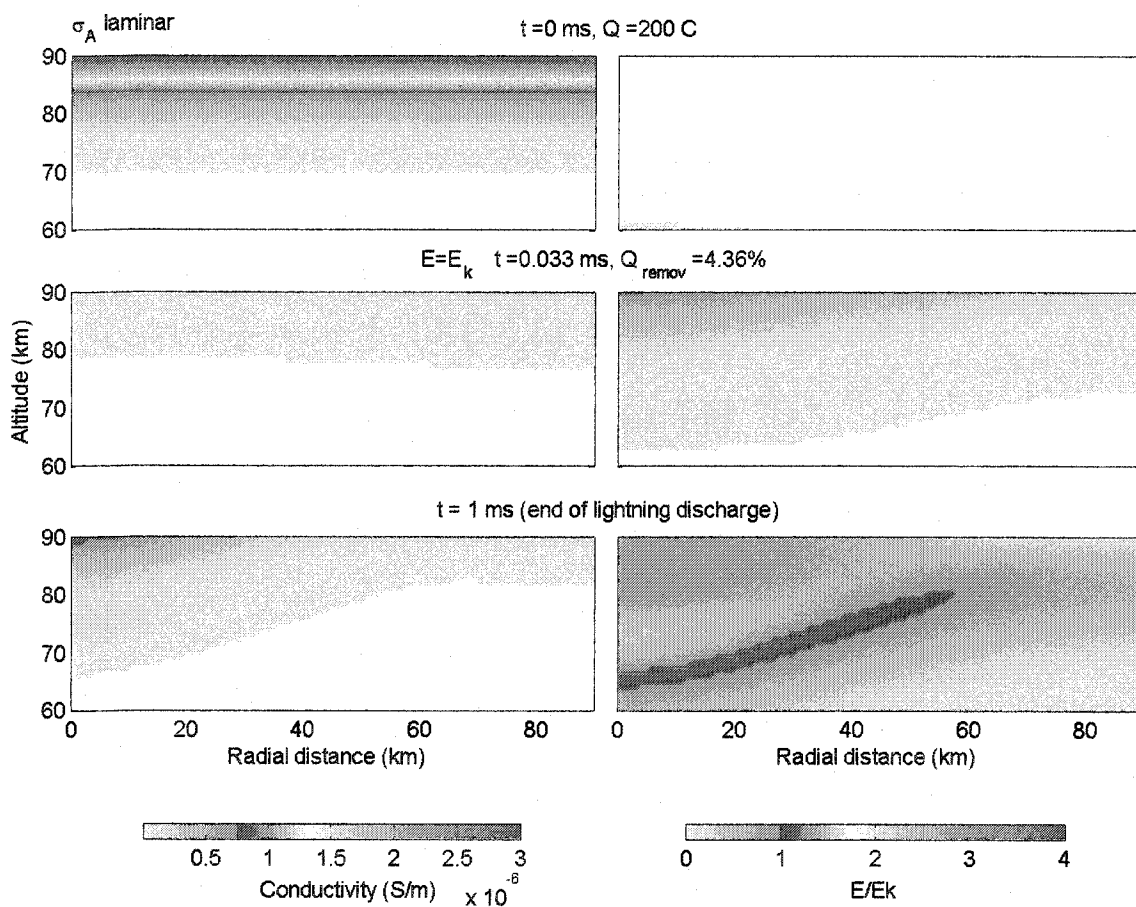
Figure 4.21 Conductivity (left) and E_{tot}/E_k, (right) for the 200 C case. The first row shows $t = 0$ ms, the second row shows when $E_{tot} = E_k$ for the first time, and the third row shows $t = 1$ ms. The percentage of the total charge removed (Q_{remov}) and breakdown time are indicated above the middle row panel. The laminar control profile, σ_A, was used.
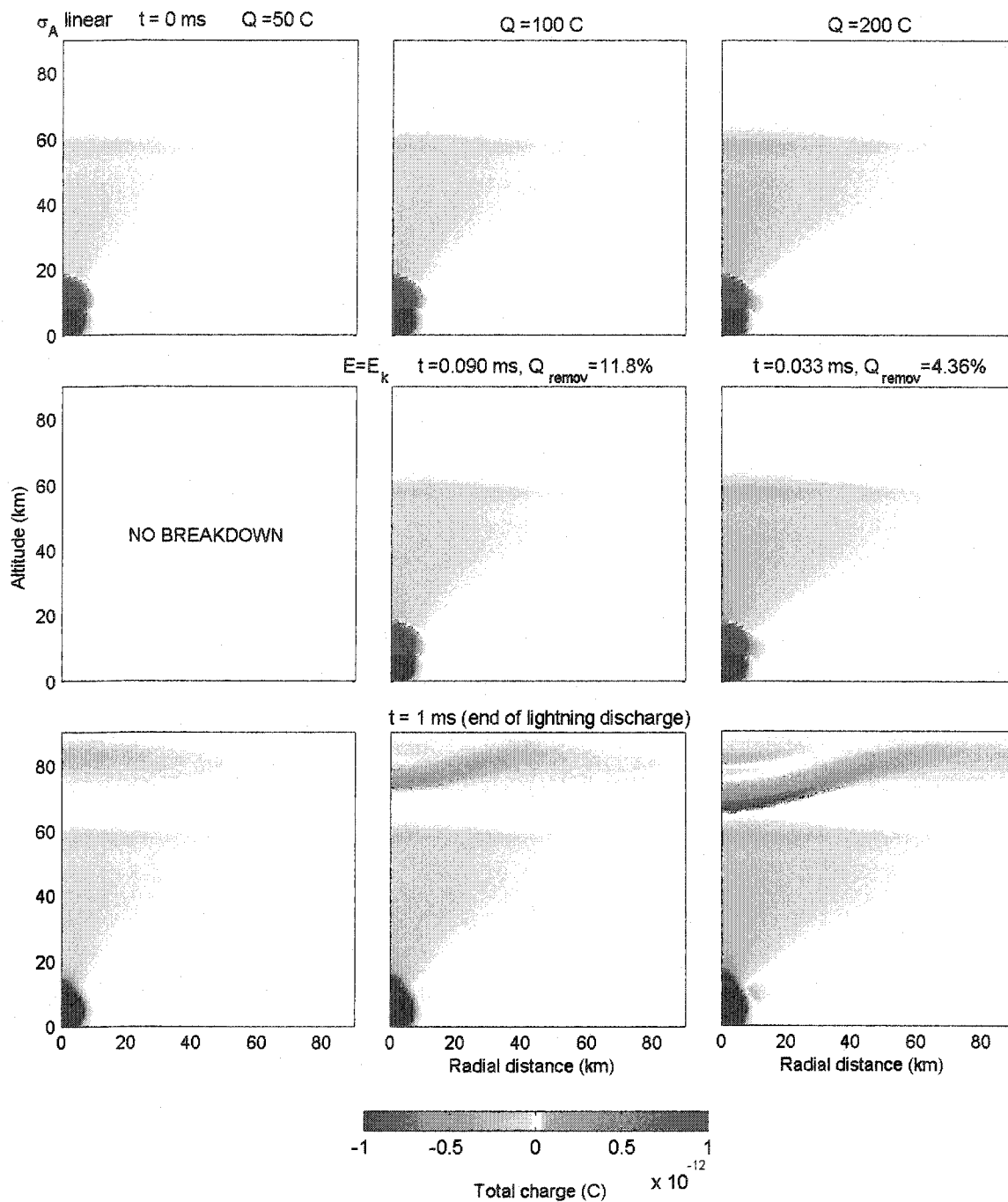
Figure 4.22 Total charge density for Q = 50, 100, 200 C. Refer to Table 4.2 for further details. The first row shows t = 0 ms, the middle row shows when $E_{tot} = E_k$ for the first time, and the last row shows t = 1 ms. The percentage of the total charge removed (Q_{remov}) and breakdown time are indicated above the middle row figures. The laminar control profile, σ_A, was used. Notice that the control case (left column) does not breakdown.

4.4.2.2 PERTURBED CASES

A total of eight different perturbation cases were evaluated, in which the relative average amplitude (A_{pert}) of the perturbation was varied from 0.1 to 0.4 in steps of 0.1, and the average characteristic spatial scale ($size_{pert}$) was either 2km or 5km. The first difference noticed between perturbed and laminar cases, is that in all the perturbed cases breakdown occurred in locations laterally displaced from the underling lightning, agreeing with sprite observations and with the distribution presented in Figure 2.4. Furthermore, breakdown occurred at multiple regions (e.g. Figure 4.27), simultaneously or within time scales less than 1 ms. Sprites initiated at these points would appear to be "simultaneous" for observations at a rate of 1000/s or less. Figure 4.23, an enlargement of part of Figure 1.7, contains *Stenbaek-Nielsen et al.* [2000] 1000 fps observations of sprites, showing multiple sprite initiation regions that breakdown points simulated by this model, e.g. Figure 4.27, could trigger. The first row was contrast enhanced.
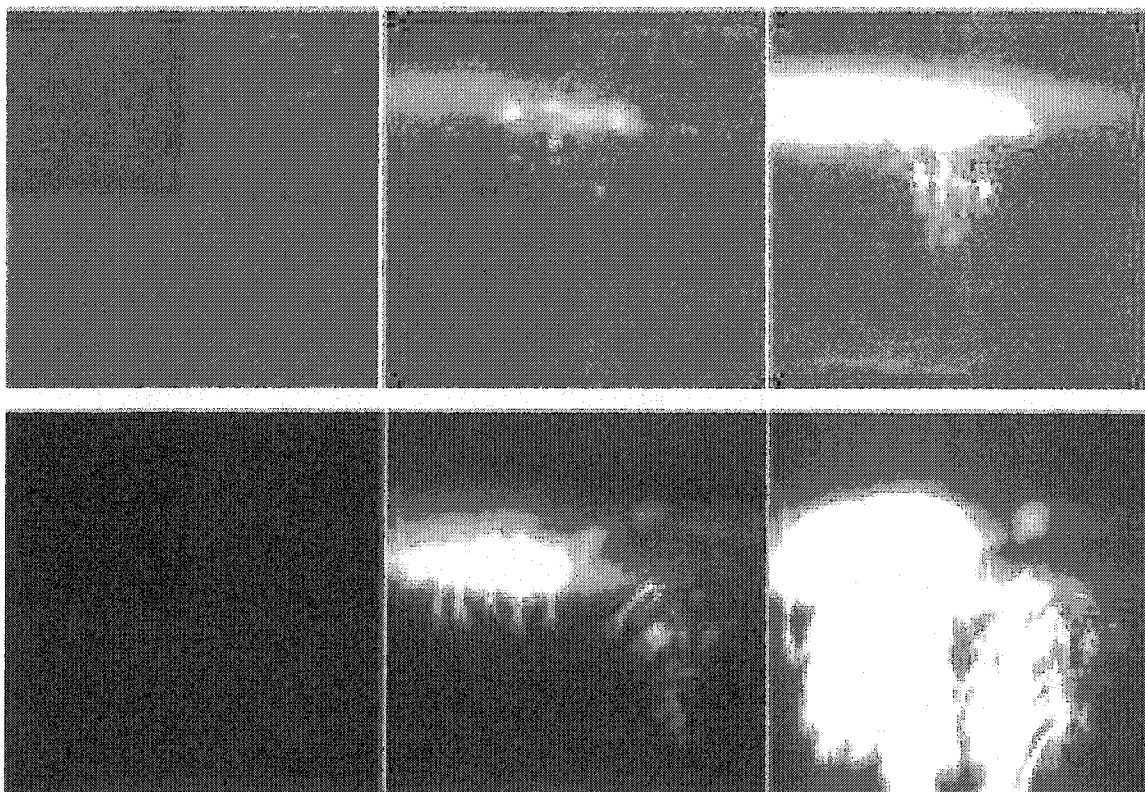
Figure 4.23 Multiple sprite initiation points shown in the middle column. This sequence of images adapted from *Stenbaek-Nielsen et al.* [2000] was recorded at 1000 fps. The first row was contrast enhanced.

Perturbations with A_{pert} = 0.1 and $size_{pert}$ = 2 km (Figure 4.24 and Figure 4.25) are sufficient to produce breakdown in the control case. However, no breakdown has been observed for 3 different patterns with A_{pert} = 0.1 and $size_{pert}$ = 5 km (not shown). The cases with A_{pert} = 0.2 and $size_{pert}$ = 2 km and 5 km are shown in Figures A-4 to A-7, and the cases with A_{pert} = 0.4 and $size_{pert}$ = 2 km and 5 km are shown in Figures A-8 to A-11 in Appendix A. Breakdown first occurred inside "pocket" regions of very large density depletions ($\geq$ 70%). As the charge moment increased, breakdown progressively occurred in regions of lower density depletions ($\leq$ 25%). Around the termination of the lightning breakdown was produced in regions with depletions $\leq$ 10%.

Figure 4.24 Electron mobility (left) and electron density (right) for perturbed case 1. The first row shows t = 0 ms, the second row shows when E_{tot} = E_k for the first time, and the third row shows t = 1 ms. The percentage of the total charge removed (Q_{remov}) and breakdown time are indicated above the middle row panel. Case 1 is the control case with input perturbations parameters A_{pert} = 0.1 and $size_{pert}$ = 2 km.
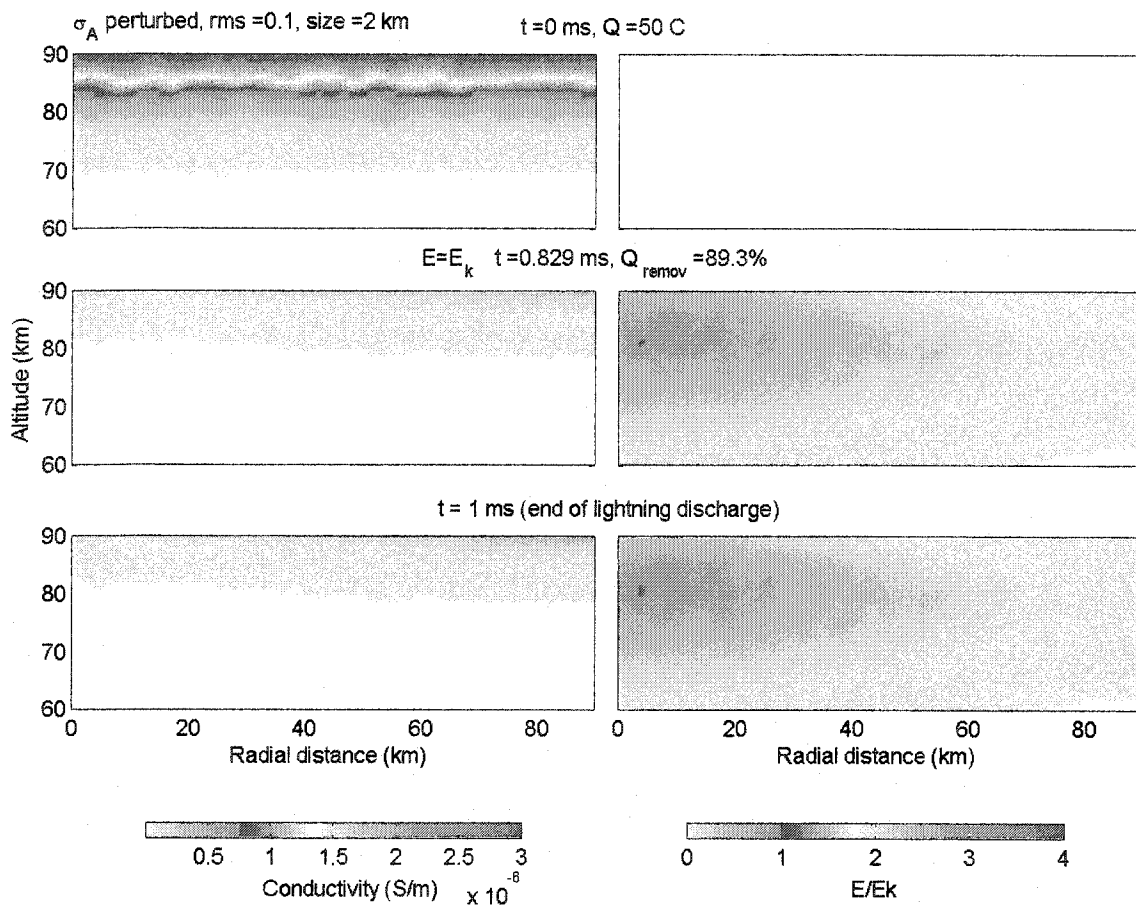
Figure 4.25 Conductivity (left) and E_{tot}/E_k (right) for perturbed case 1. The first row shows $t = 0$ ms, the second row shows when $E_{tot} = E_k$ for the first time, and the third row shows $t = 1$ ms. The percentage of the total charge removed (Q_{remov}) and breakdown time are indicated above the middle row panel. Case 1 is the control case with input perturbations parameters $A_{pert} = 0.1$ and $size_{pert} = 2$ km.

For a larger perturbation amplitude, $A_{pert} = 0.3$, with the same size, $size_{pert} = 2$ km, larger modifications of the atmosphere were observed. Breakdown was produced at multiple locations, within pockets of decreased neutral density. The first breakdown point occurred at ~84 km altitude, and ~7 km lateral displacement, in a pocket of ~74% density depletion. Regions with lower density depletions, e.g. ~20% and ~5%, located at (r, z) coordinates approximately (7, 85) and (9, 81) respectively, broke down at a latter time. In these pocket regions E_k was lowered. This effect summed with the self-consistent reduction of the conductivity, discussed in the previous section, "facilitated" breakdown.
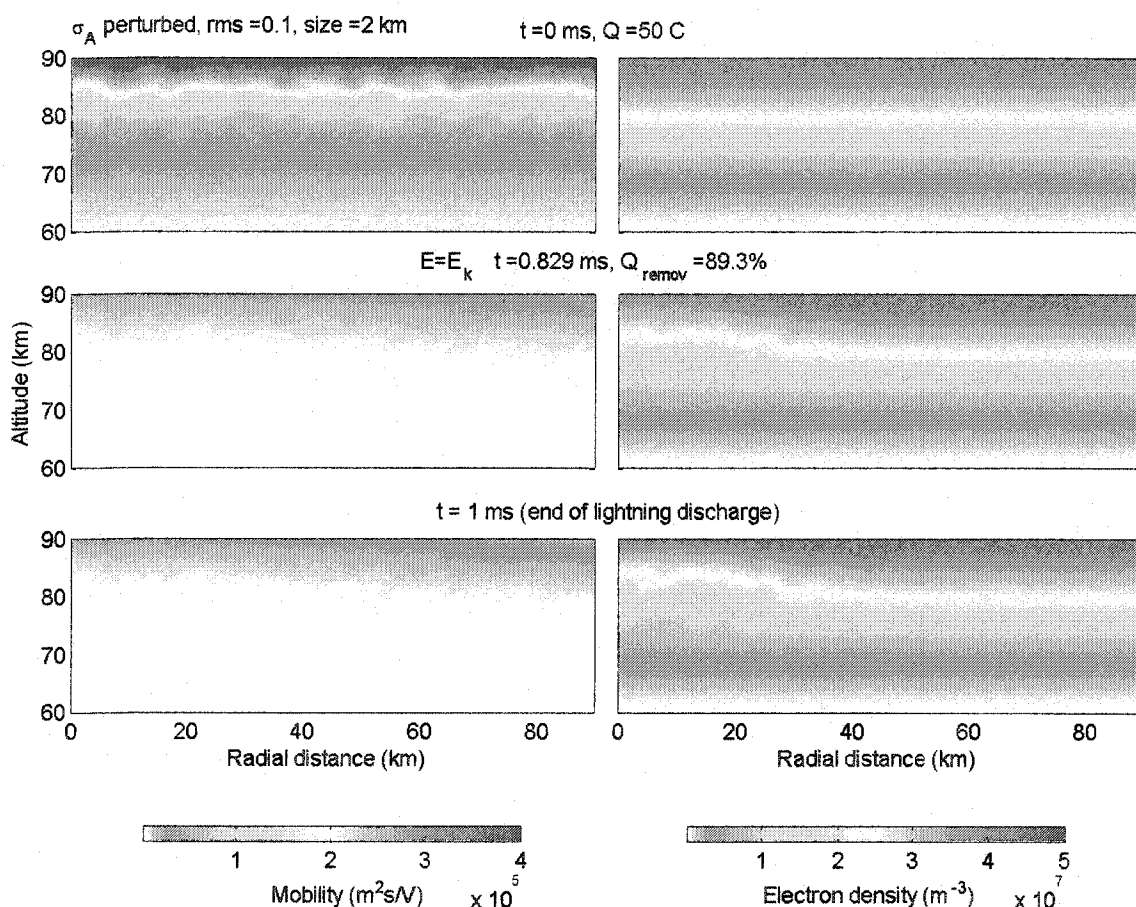
Figure 4.26 Electron mobility (left) and electron density (right) for perturbed case 4. The first row shows t = 0 ms, the second row shows when $E_{tot} = E_k$ for the first time, and the third row shows t = 1 ms. The percentage of the total charge removed (Q_{remov}) and breakdown time are indicated above the middle row panel. Case 4 is the control case with input perturbations parameters A_{pert} = 0.3 and $size_{pert}$ = 2 km.

Figure 4.27 Conductivity (left) and E_{tot}/E_k (right) for perturbed case 4. The first row shows $t = 0$ ms, the second row shows when $E_{tot} = E_k$ for the first time, and the third row shows $t = 1$ ms. The percentage of the total charge removed (Q_{remov}) and breakdown time are indicated above the middle row panel. Case 4 is the control case with input perturbations parameters $A_{pert} = 0.3$ and $size_{pert} = 2$ km.

Keeping the same average amplitude of $A_{pert} = 0.3$ and increasing the average size of the perturbations to $size_{pert} = 5$ km, breakdown also occurred in pocket regions of neutral density depletions. The first breakdown point (depletion ~74%) was located at approximately (48, 82). At the termination of the discharge, a second, large, breakdown region (depletions ranging from ~35% to ~16%) centered at approximately (7, 80) had developed. The removal of a larger amount of charge was necessary to produce breakdown in this case (~26%), compared to the case in which the average size was 2 km (~18%).

In all cases, the conductivity is enhanced in the regions of depleted density, which tends to inhibit breakdown. A focusing of the electric field is expected to occur at the external surface of the pocket of enhanced conductivity, however this effect is only minor. Conductivity effects, however, are dominated by the lowering of the breakdown threshold due to the depleted density and the overall effect is breakdown facilitation, as mentioned before.
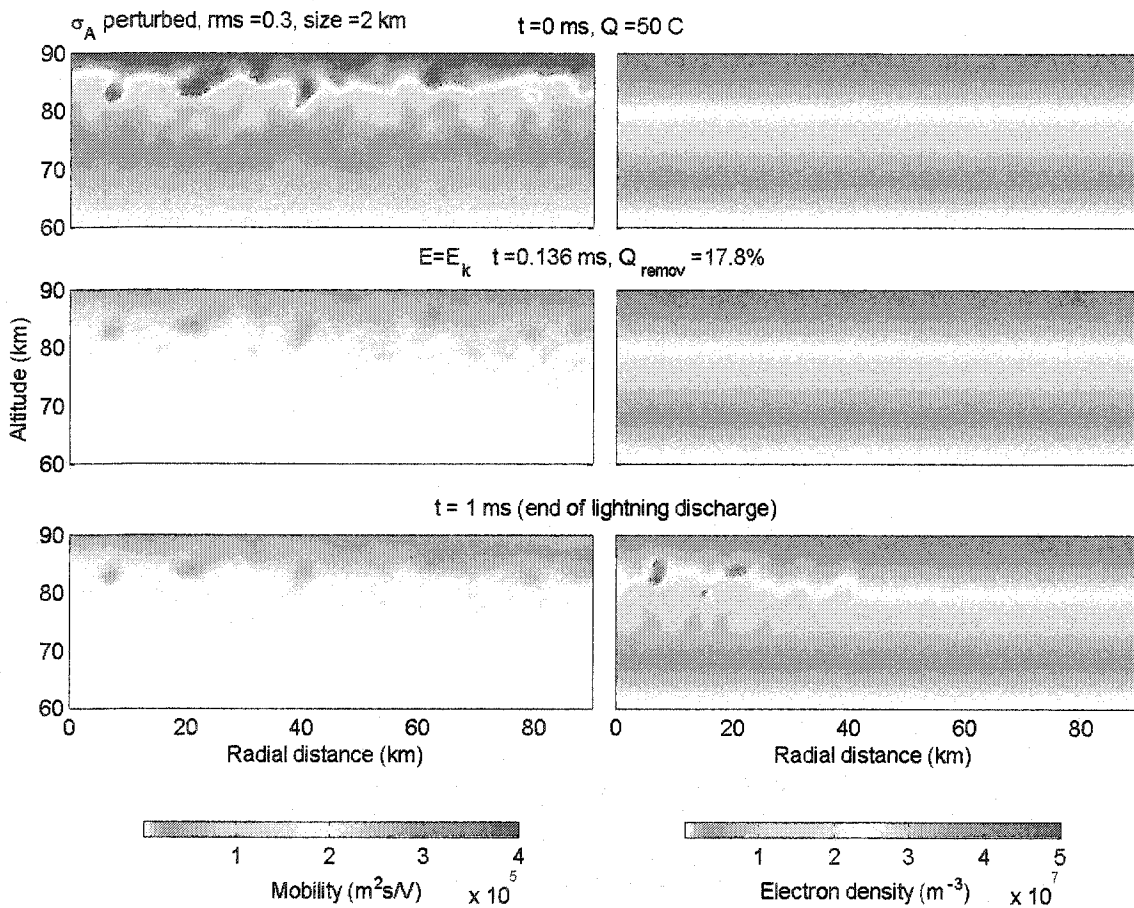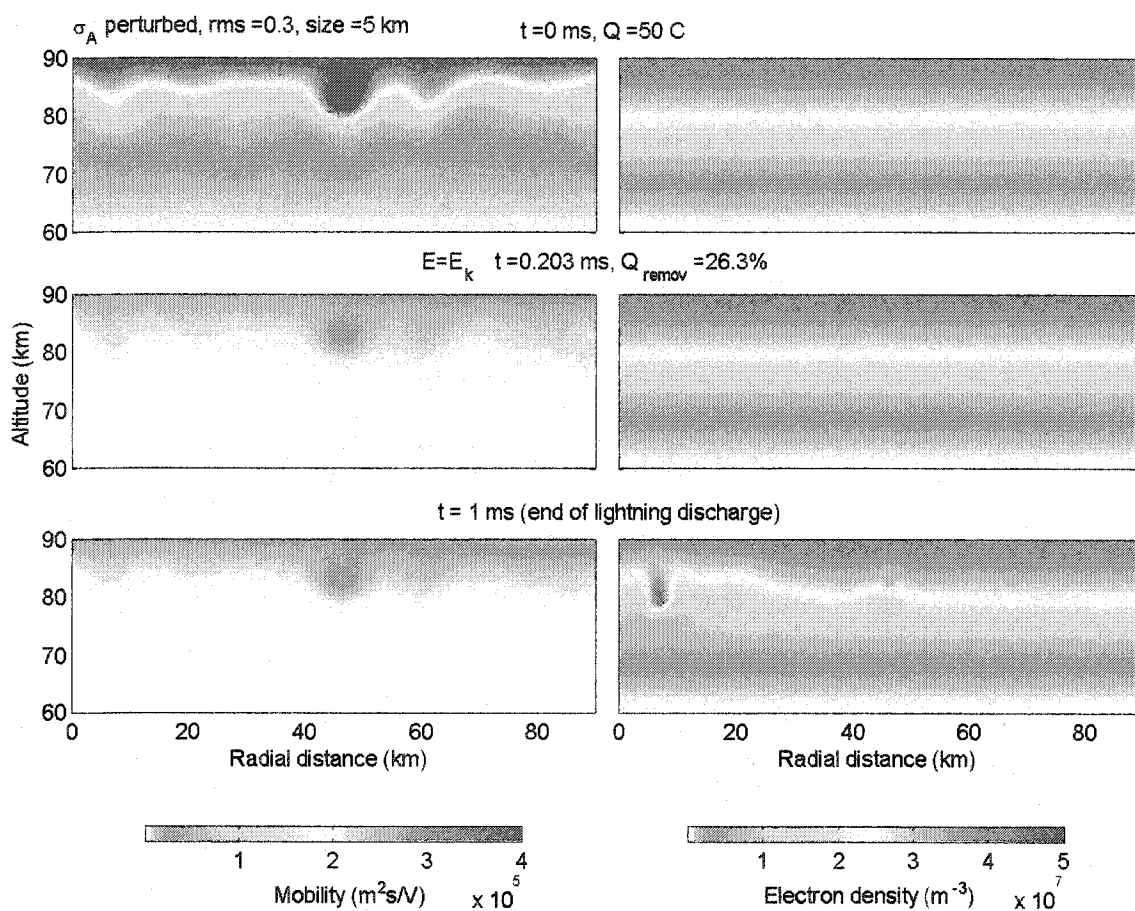

Figure 4.28 Electron mobility (left) and electron density (right) for perturbed case 5. The first row shows t = 0 ms, the second row shows when $E_{tot} = E_k$ for the first time, and the third row shows t = 1 ms. The percentage of the total charge removed (Q_{remov}) and breakdown time are indicated above the middle row panel. Case 5 is the control case with input perturbations parameters $A_{pert} = 0.3$ and $size_{pert} = 5$ km.
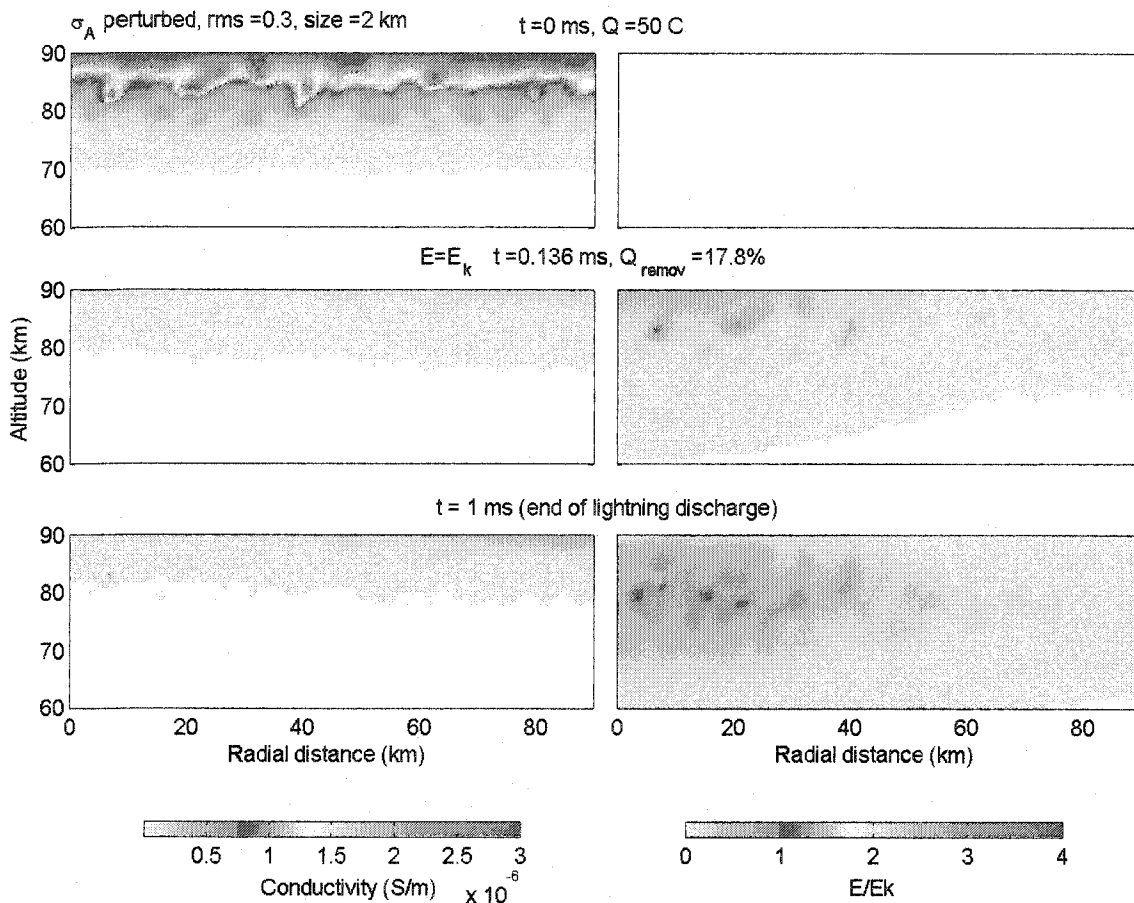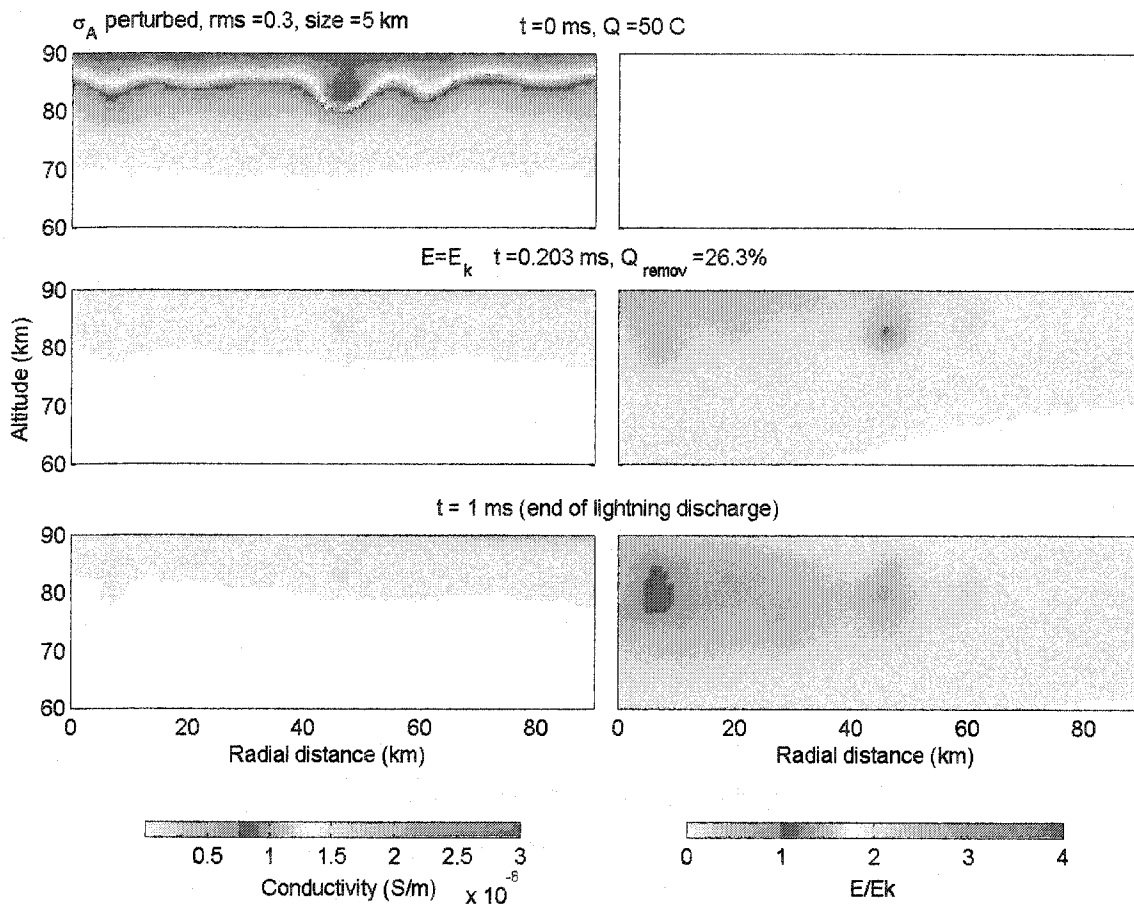
Figure 4.29 Conductivity (left) and E_{tot}/E_k (right) for perturbed case 5. The first row shows $t = 0$ ms, the second row shows when $E_{tot} = E_k$ for the first time, and the third row shows $t = 1$ ms. The percentage of the total charge removed (Q_{remov}) and breakdown time are indicated above the middle row panel. Case 5 is the control case with input perturbations parameters $A_{pert} = 0.3$ and $size_{pert} = 5$ km.

Figure 4.30 shows the total charge density in the atmosphere for the cases with average perturbation $size_{pert} = 2$ km and $A_{pert} = 0.1$, 0.3 and 0.4, respectively, before the lightning, when the electric field first reached breakdown, and at the end of the discharge. The layer of positive polarization charge above 60 km, centered above the thunderstorm, shows spatial structure that reflects the amplitude and size of the perturbations.
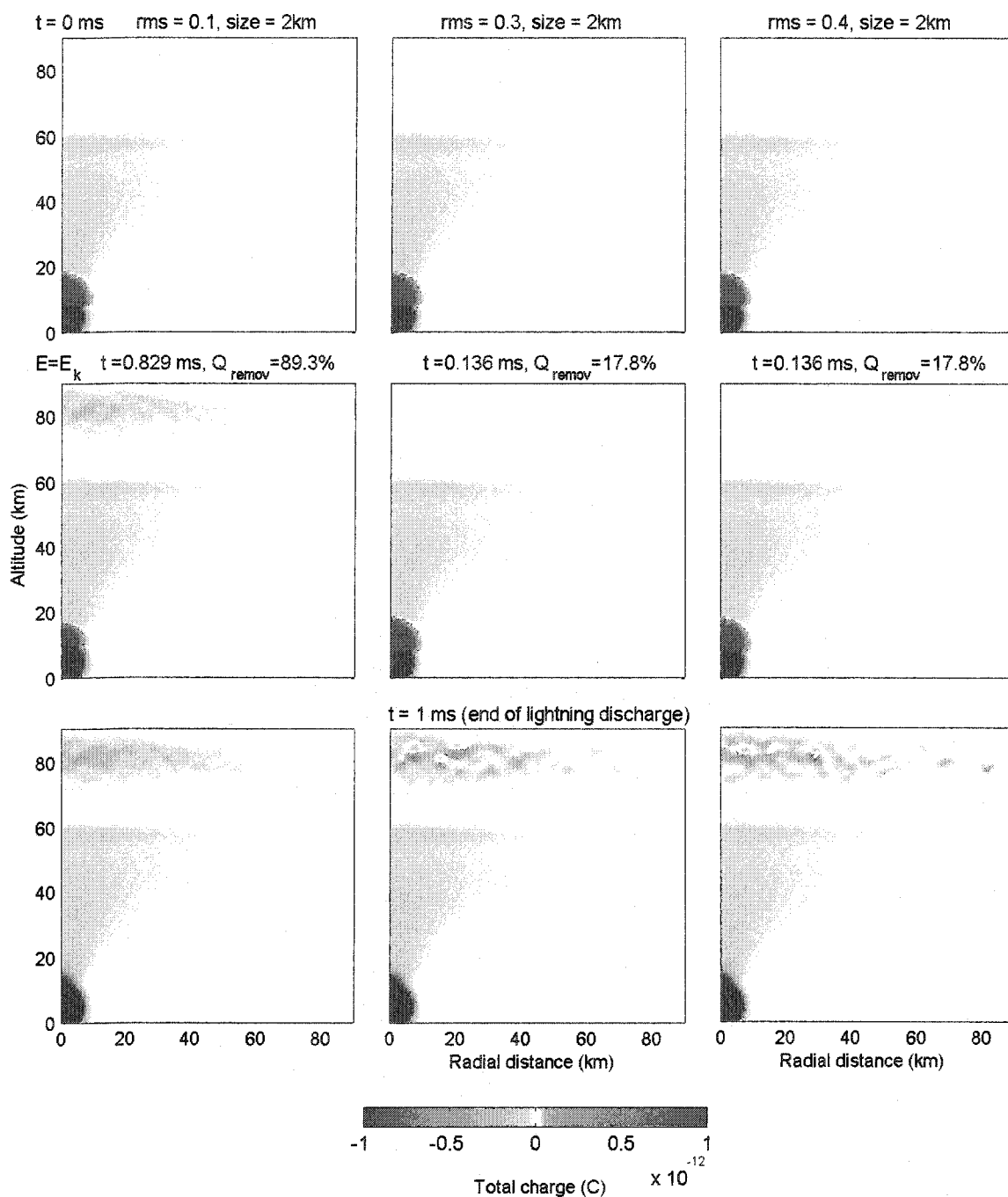
Figure 4.30 Total charge density for perturbed cases 1, 4 and 6. Refer to Table 4.3 for further details. The first row shows $t = 0$ ms, the middle row shows when $E_{tot} = E_k$ for the first time, and the last row shows $t = 1$ ms. The percentage of the total charge removed (Q_{remov}) and breakdown time are indicated above the middle row figures. The laminar control profile, σ_A, was used. Cases 1, 4 and 6 are the control case with input perturbations parameters $A_{pert} = 0.1$, 0.3 and 0.4 and $size_{pert} = 2$ km.

Figure 4.31 shows a summary of the effects of neutral density perturbations in the conductivity spatial structure and the location of electric breakdown points in the atmosphere for the profile σ_A, 50 C, $size_{pert} = 2$ km and $A_{pert} = 0.1, 0.2, 0.3$ and 0.4.
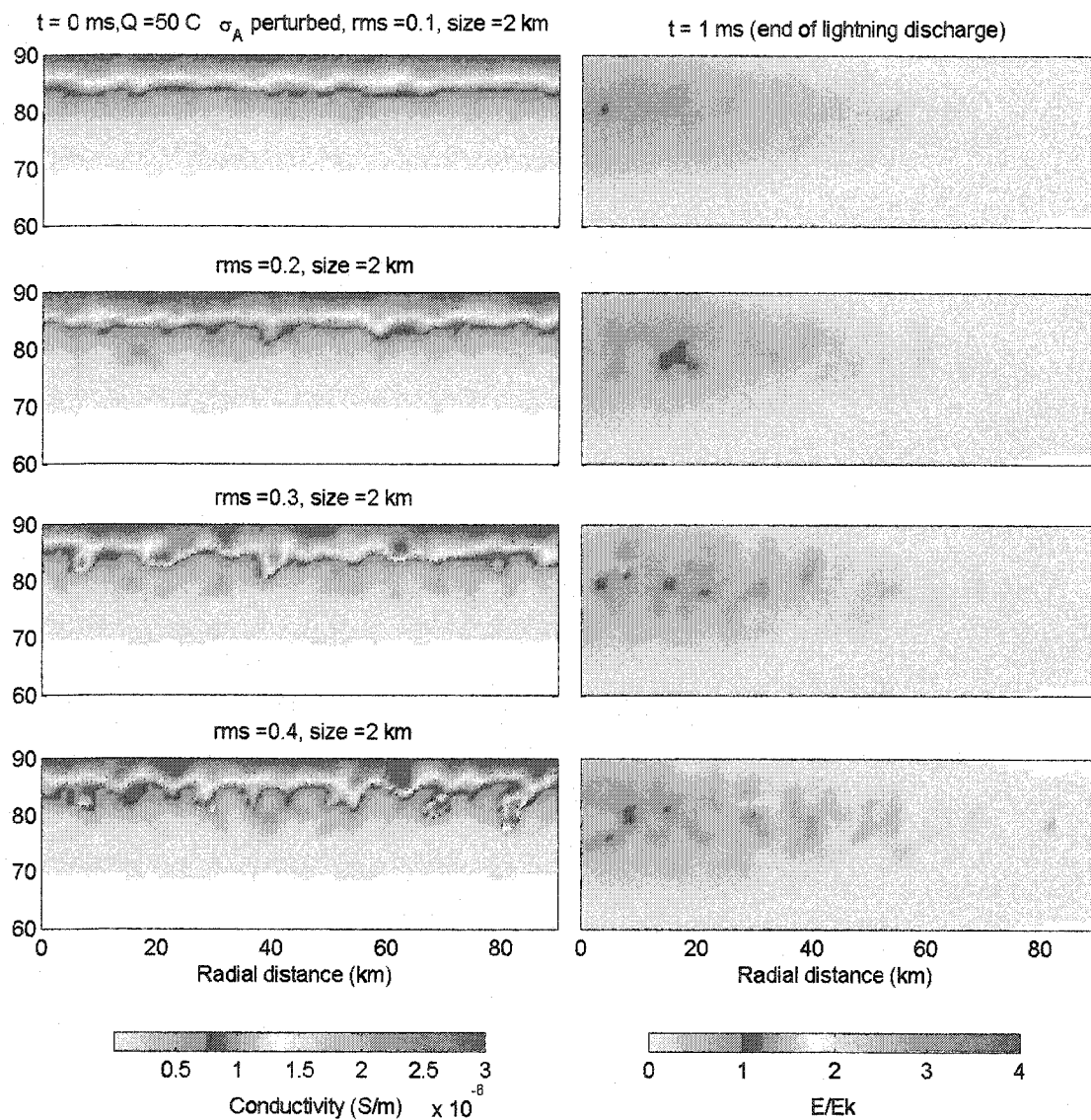
Figure 4.31 Summary of the effects of conductivity spatial perturbations. Perturbed conductivity profiles at $t = 0$ ms (left) and the E/E_k at $t = 1$ ms (right). The $size_{pert} = 2$ km and A_{pert} varies between 0.1 and 0.4 from top to bottom.

4.4.2.3 NEGATIVE LIGHTNING

A negative lightning discharge was generated for the perturbed case with A_{pert} = 0.3 and $size_{pert}$ = 2 km. Here, charge was removed from the bottom negative charge center to simulate a -CG discharge, as opposed to removal of charge from the top positive center, as in the previous runs.

Breakdown first occurred at the same location as for the positive discharge (Figure 4.33 and Figure 4.27 respectively). The negative discharge required removal of more charge to produce breakdown than the positive, ~64.5% against 17.8%. This is consistent with expectations, since the associated charge moment for the -CG (250 C/km) was half that of the +CG (500 C/km) on account of the lower altitude of the negative charge. The duration used for the negative is longer than typical values, which may also contribute to the larger charge removal necessary for breakdown. The return stroke of a typical negative cloud-to-ground discharge has a characteristic duration of ~100 µs [Uman, 1987], with peak currents of ~30 kA. Large strokes may possess currents that surpass 200 kA. Thus, the average charge transferred in a typical negative lightning discharge is ~30 C, with large strokes transferring up to 200 C.

No breakdown region was present at the termination of the lightning. Another difference is that the polarization charge layer formed above 60 km was of negative polarity, as opposed to positive due to a +CG (Figure 4.34).
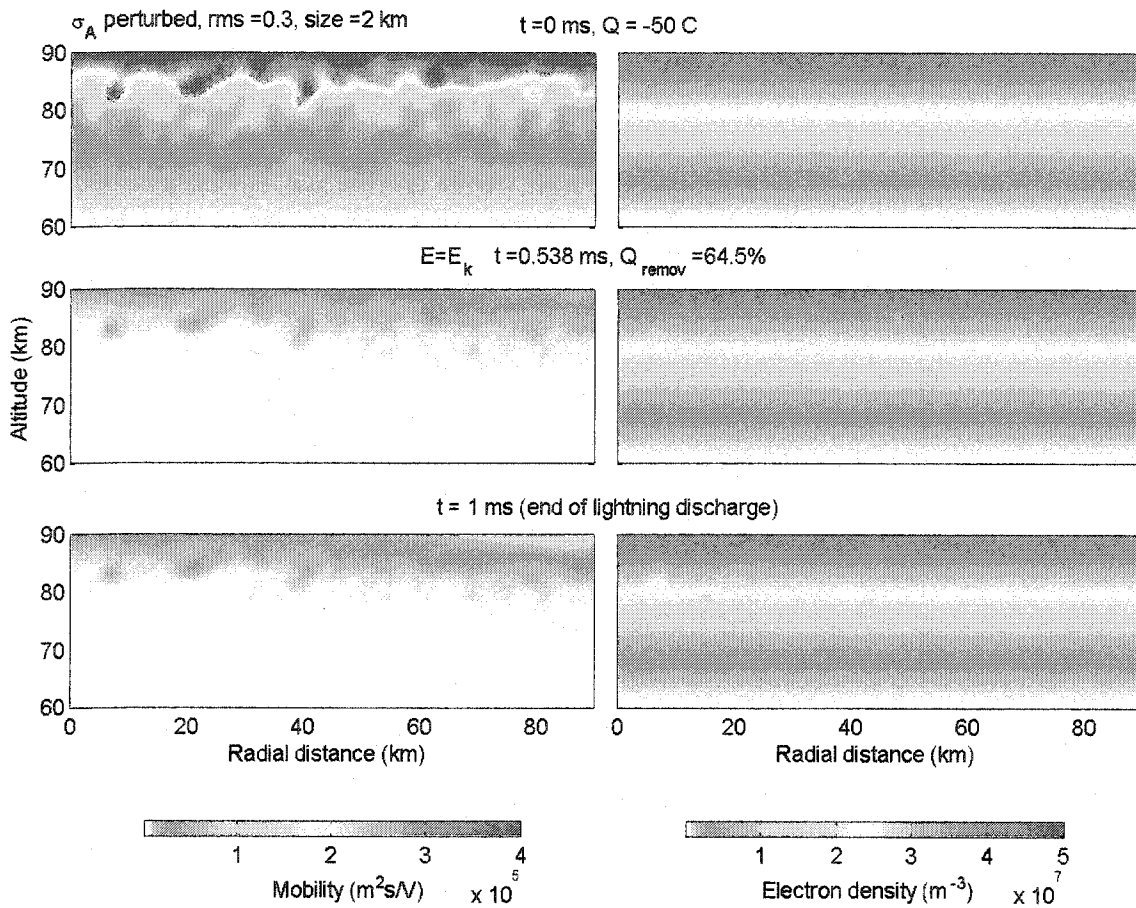
Figure 4.32 Electron mobility (left) and electron density (right) for negative discharge. The first row shows $t = 0$ ms, the second row shows when $E_{tot} = E_k$ for the first time, and the third row shows $t = 1$ ms. The percentage of the total charge removed (Q_{remov}) and breakdown time are indicated above the middle row panel. The –CG was performed for case 3, the control case with input perturbations parameters $A_{pert} = 0.3$ and $size_{pert} = 2$ km.

σ_A perturbed, rms =0.3, size =2 km   t =0 ms, Q = -50 C

E=E$_k$ t =0.538 ms, Q$_{remov}$ =64.5%

t = 1 ms (end of lightning discharge)

Altitude (km)

Radial distance (km)   Radial distance (km)

Conductivity (S/m) $\times 10^{-8}$ E/Ek

Figure 4.33 Conductivity (left) and E_{tot}/E_k (right) for negative discharge. The first row shows $t = 0$ ms, the second row shows when $E_{tot} = E_k$ for the first time, and the third row shows $t = 1$ ms. The percentage of the total charge removed (Q_{remov}) and breakdown time are indicated above the middle row panel. The –CG was performed for case 3, the control case with input perturbations parameters $A_{pert} = 0.3$ and $size_{pert} = 2$ km.
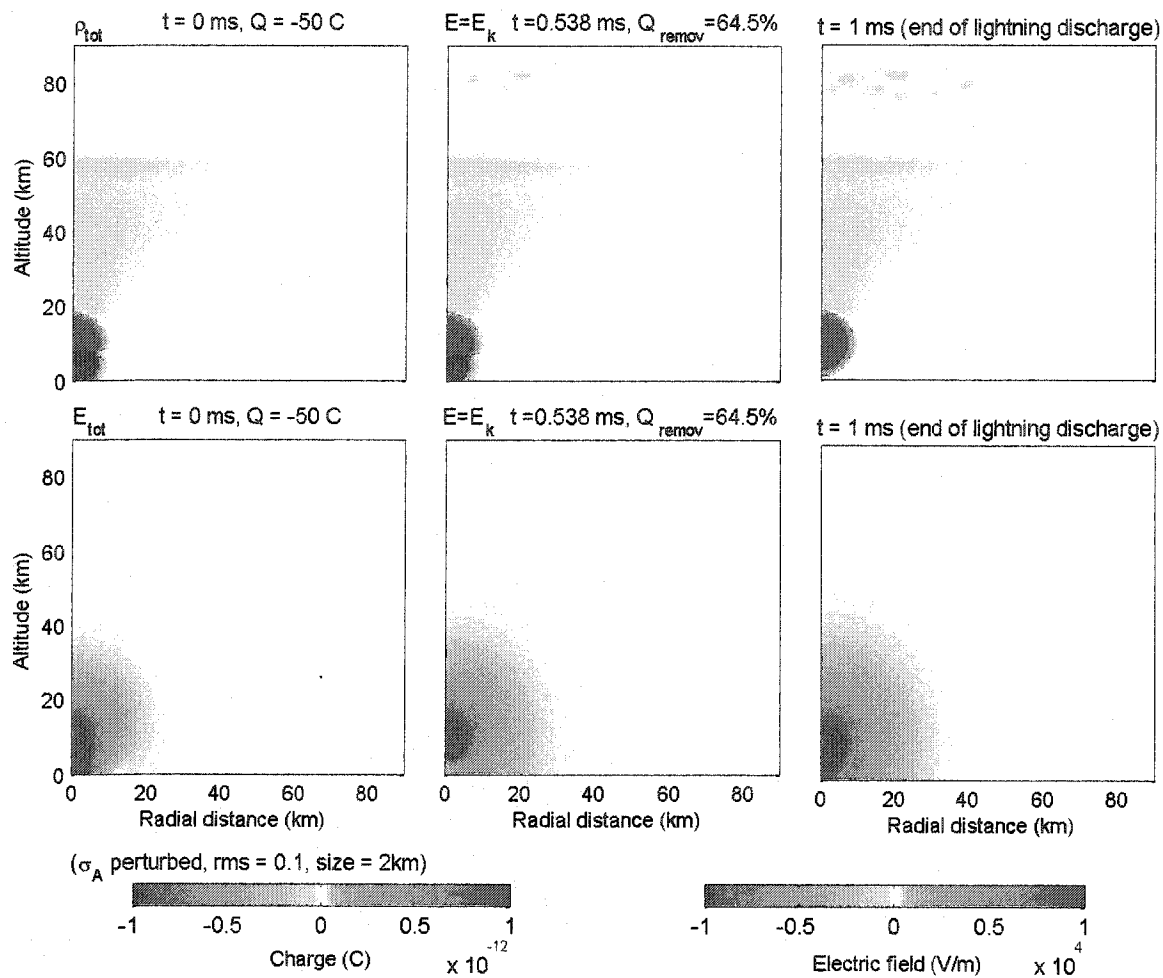
Figure 4.34 Total charge density for negative discharge. The first column shows $t = 0$ ms, the middle column shows when $E_{tot} = E_k$ for the first time, and the last column shows $t = 1$ ms. The percentage of the total charge removed (Q_{remov}) and breakdown time are indicated above the middle column figures. The $-$CG was performed for case 3, the control case with input perturbations parameters $A_{pert} = 0.3$ and $size_{pert} = 2$ km.

4.5 SUMMARY OF RESULTS

Simulations of the response of the upper atmosphere to lightning discharges were performed using a non-linear, self-consistent quasi-electrostatic model. The objective was to investigate the role of neutral turbulence in creating multiple, laterally offset breakdown regions for sprite initiation. The results can be summarized as follows:

1. The results for a laminar atmosphere agree well with results previously obtained by *Pasko et al.* [1997b].

2. Spatial structure in the neutral density can facilitate breakdown of the upper atmosphere by lowering the breakdown threshold at regions of density depletions, such that weaker electric fields than in a laminar atmosphere are needed to produce breakdown.

3. The conductivity, which is enhanced at the density depleted regions, has the effect of inhibiting breakdown at those pockets; electric field focusing on the external surfac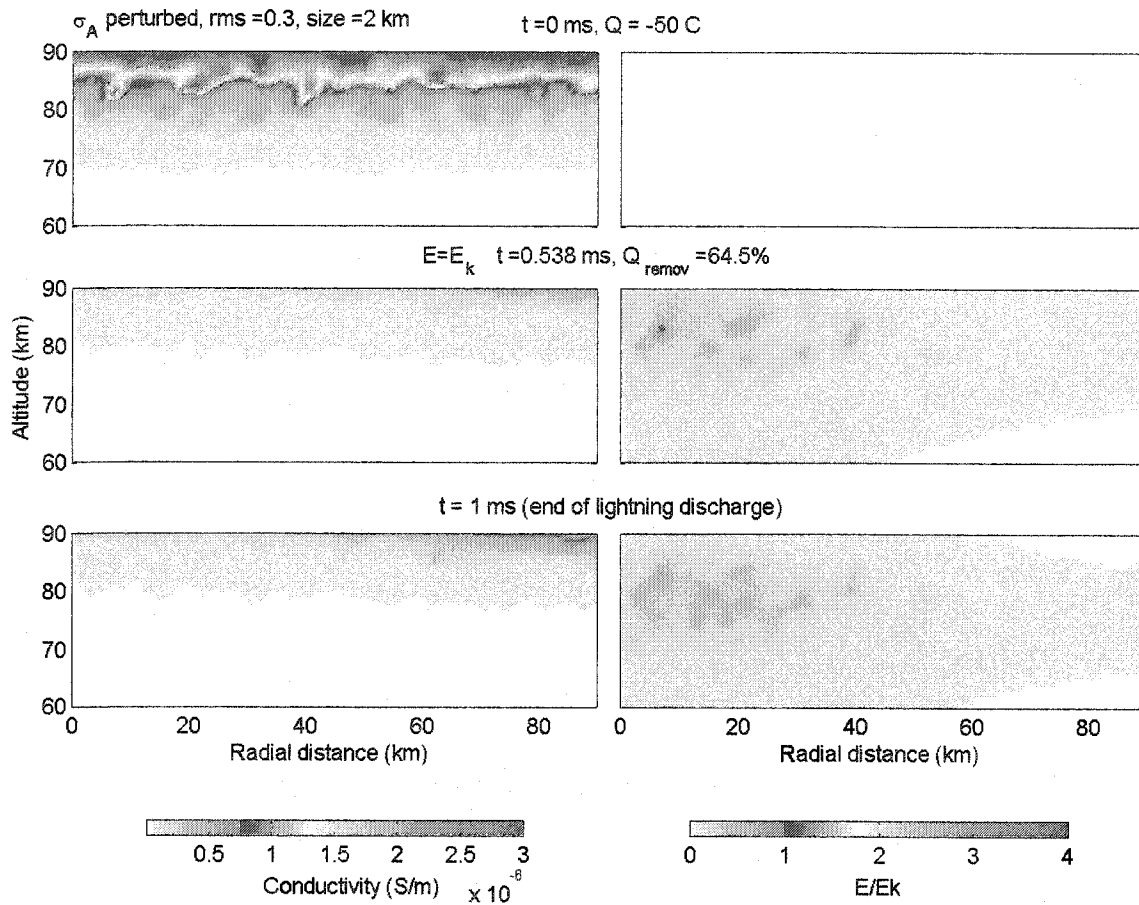e of those regions is only marginal. However the conductivity effects are dominated by the effects of the lower breakdown threshold due to the lower density.

4. Breakdown occurred at multiple points between ~75 km and ~85 km altitude, laterally displaced from the underlying lightning. This result is consistent with occurrence of multiple sprites generated by a single lightning, as well as their lateral displacements.

5. Breakdown first occurred inside pockets of large density depletions ($\geq 70\%$). As the charge moment increased, breakdown progressively occurred in regions of lower density depletions ($\leq 25\%$). Around the termination of the lightning breakdown was produced in regions with depletions $\leq 10\%$.

6. A negative discharge may also lead to breakdown in a turbulent atmosphere.

7. The model accounts for the occurrence and location of multiple breakdown points. Sprites may develop at these breakdown points if conditions for streamer generation are satisfied.

8. The model is two-dimensional and for $r > 0$ the modeled turbulence corresponds to cylindrical rings centered at the symmetry axis. For short segments, the turbulence modeled here closely corresponds to plane wave, mesospheric bores and rolls that are observed at mesospheric heights.

9. The results obtained in this study are not expected to change significantly in a 3-D isotropic turbulence field. The main effect facilitating breakdown is the lowering of the threshold in density depletions. This occurs because the electron-neutral mean free path is increased, and the mean free path is isotropic.

CHAPTER 5

CONCLUSIONS

In this work the role of conductivity spatial structure in determining the location of sprite initiation points was studied. The investigation was motivated by observations showing that sprites are typically offset laterally by several tens of km from the parent lightning, and was performed in three interrelated studies: (a) A statistical analysis of the temporal-spatial relationships between sprites and their causative lightning; (b) An analysis of the relationship between the convective activity of the underlying thunderstorm, based on GOES-8 observations of infrared cloudtop temperatures, and the occurrence of lightning and sprites; and (c) Computer simulations of the temporal-spatial evolution of the lightning-induced electric fields in the mesosphere, under conditions when the neutral density structure is both laminar and turbulent. The nonlinear relationship between the electric field and the conductivity plays an important role in the response of the system, and is treated self-consistently in the simulations. The results of these studies are summarized in detail at the ends of Chapters 2, 3 and 4, respectively. Studies (a) and (b) have been published as standalone works, and provide the observational foundation for the simulations presented in study (c).

The principal results from study (a) used in the simulations are the distribution of distances between sprites and their parent +CG, showing that most sprites (~2/3) occur within 50 km from the +CG. The principal result of study (b) of importance to the simulations was the dynamical relationship between thunderstorm convective activity and the production rate of the total -CG population and sprites. This aspect was revealed when the maximum sprite and -CG production of the system were simultaneously achieved at the time of maximum contiguous cloud cover of the coldest region with $T_c \leq$ -52° C (region with most intense convective activity). Observations have shown that sprite activity generally commences a few hours after the onset of lightning activity, suggesting that the thunderstorm creates some delayed pre-conditioning of the

mesosphere. It was hypothesized that this pre-conditioning could originate from thunderstorm generated gravity waves, and/or turbulence from breaking gravity waves, creating density perturbations at the altitude range of ~75 to ~85 km, where sprites are observed to be initiated. On average, gravity waves take a few hours to propagate to the mesopause, which is consistent with the observed delay of several hours between onset of lightning and sprite production.

Perturbations to the neutral density can also be generated by other sources, e.g. wind shear instability, and mesospheric bores and rolls. Independent of the source, neutral density perturbations alter the local response of the atmosphere to electrical stimuli. Under these circumstances, breakdown, a necessary condition for sprite development, may occur at particular locations that are not directly above the generating cloud-to-ground discharge.

Model simulations of the effects of neutral density perturbations on mesospheric electrical breakdown were performed to test this hypothesis. The perturbations were modeled as isotropic random turbulence fields spanning a range of amplitudes and characteristic scale sizes similar to observed mesospheric perturbations.

The results from the simulations of a laminar atmosphere elucidated the non-linear self-consistent relationship between the electric field and conductivity. The electric field applied to the mesosphere due to thundercloud charge removal heats the free electrons above 60 km, increasing the electron-neutral collision frequency, which decreases their mobility. Consequently, the conductivity, which is directly proportional to the mobility, is reduced; this reduction can be as much as a factor of fifty. The effects due to changes in the electron density, which are completely dominated by the effects due to electron heating, also contribute to the reduction of conductivity, since attachment dominates before the field reaches the breakdown threshold. This reduction of the conductivity leads to a faster growth of lightning induced electric field in the mesosphere than if the self-consistent effects are not taken into account.

In the simulations a standard thundercloud charge distribution, comprising a positive charge $+Q$ at an altitude of 10 km and negative charge $-Q$ at 5 km, was adopted for all cases. Measurements show that the actual charge distribution inside the thunderstorm can be extremely complex involving several layers of charge with alternated polarity. For the strength of the lightning generated electric field in the mesosphere, the important quantity is the charge moment and the simple standard model adopted is perfectly adequate. A $+/-$CG discharge was simulated by removal of the $+/-Q$ with a characteristic time scale of a few hundred μs, and complete removal after 1 ms. The discharge was performed in a pre-lightning configuration having the atmosphere above 50 km relaxed from the influence of the thundercloud dipolar electric. As previously mentioned, sprite activity generally commences a few hours after the onset of lightning activity. If the interval between lightning discharges is shorter than the relaxation time at a particular altitude h_{lim}, the pre-sprite electric field configuration at h_{lim} and lower altitudes will be different from the pre-lightning configuration used here, and may be a superposition of $+/-$ cloud-to-ground, and/or intracloud and etc, discharges. The pre-lightning configuration used in the simulations is a good approximation since the average time interval between CGs ranges from ~300 ms to ~1.5 s.

To simulate neutral density perturbations, a randomly generated isotropic turbulence layer centered at 80 km with a characteristic thickness of 10 km was introduced in the neutral density. Electric fields produced by positive cloud-to-ground discharges using mesospheric turbulence levels with relative average amplitudes 0.1-0.4 and average characteristic scale sizes 2 and 5 km, were investigated. These cases were compared against a laminar control case that did not breakdown. Breakdown occurred in all simulations involving perturbed mesosphere except the case of the perturbation with the smallest relative amplitude (0.1) and largest average perturbation scale size (5 km).

The simulation of a negative lightning discharge also produced breakdown in a perturbed atmosphere. The breakdown occurred at the same location as for the first breakdown point produced by a positive discharge using the same perturbation pattern. The removal of a larger amount of charge was necessary for breakdown with a negative

discharge than for the positive charge, consistent with observations that negative sprites are less frequent events than positive sprites on account of the lower overall charge moments associated with negative lightning. These results are consistent with the results of Chapter 2, where it was found that 17% of the sprites did not have a parent +CG registered by NLDN or VLF sensor, and one sprite was associated with a negative cloud-to-ground discharge.

In the perturbed cases, breakdown occurred in isolated pockets of neutral density depletions. In no case was breakdown observed in regions of increased density. The physical reason for this behavior is that inside pockets of lower density, the electron-neutral mean free path is increased, which lowers the characteristic electric breakdown field. In the absence of an electric field such density depletions induce local conductivity enhancements due to reduced collision frequency and increased mobility. At the onset of the cloud-to-ground lightning discharge, the enhanced conductivity initially leads to a lower electric field inside the depletions. However, when the field grows enough to heat the local free electrons ($E \sim 0.0005\ E_k$), their mobility decreases, leading to a reduction of the local conductivity and larger electric fields. Even though by the moment of breakdown the conductivity can be a factor of 50 lower than the initial value, it is still a local maximum. Focusing of the electric field occurs at the external surface of those pocket regions, but this effect is only minor compared to the effect of conductivity enhancement. Consequently, the resulting effect of the conductivity is to inhibit breakdown at the pockets of density depletions. Conductivity effects are dominated by the lowering of the breakdown threshold purely due to the depleted density, with the end result that breakdown is locally "facilitated" inside pockets of neutral density depletions. Sprites will initiate at these locations if the local mesospheric conditions are conducive to the subsequent development of streamer channels.

The turbulence levels modeled in this work correspond to moderate turbulence. Knowledge of the mean level of fluctuations in the mesosphere is presently sparse, as is information about the variance of this quantity, or the relative occurrence rates of discrete structures such as monochromatic wave trains, mesospheric bores and rolls in comparison

to isotropic turbulence. In the perturbed density cases studied here, breakdown occurred first in locations corresponding to regions of greatest density depletions ($\geq 70\%$), and was followed by breakdown in other regions of progressively smaller density depletions. Close to the termination of the lightning discharge (1 ms) breakdown occurred in regions with density depletions $\leq 10\%$. The breakdown threshold depended on a combination of size and amplitude of the local density perturbation, and charge moment of the underlying lightning.

Because the dominant effect facilitating breakdown, the reduction of the breakdown threshold, is a local effect due solely to neutral density depletions, it is immune to structure out of the r-z model plane. Hence, the results obtained from the present two-dimensional cylindrical model simulations also apply to good approximation to three-dimensional turbulence. Short sections of the cylindrically symmetric rings modeled are in fact good approximations to horizontal plane waves, mesospheric bores and rolls that are observed at mesospheric heights. Therefore, the two-dimensional cylindrical model used here can be used to study a wide variety of mesospheric conductivity inhomogeneities.

This work extends previous studies of the effects of neutral density perturbations on breakdown by using realistic mesospheric turbulence structures and following the dynamical development of breakdown within these structures in response to applied lightning electric fields. The results demonstrate that regions of neutral density depletions in the mesosphere lead to local electrical breakdown at multiple sites laterally offset from the parent lightning discharge. These results are in good agreement with sprite observations. Furthermore, the results of this work indicate that neutral density depletions may play a decisive role in setting the sprite activity level above a thunderstorm. The isolated breakdown points provide the seed electrons necessary for the primary electron avalanche that initiate the generation of the plasma streamers forming sprites.

REFERENCES

Abramowitz, M., and I. Stegun, Handbook of Mathematical Functions, Dover, New York, 1962.

Alexander, M.J., A simulated spectrum of convectively generated gravity waves: Propagation from the tropopause to the mesopause and effects on the middle atmosphere, *J. Geophys. Res.*, 101(D1), 1571, 1996.

Armstrong, R.A., J.A. Shorter, M.J. Taylor, D.M. Suszcynsky, W.A. Lyons, and L.S. Jeong, Photometric measurements in the SPRITES '95 and '96 campaigns of nitrogen second positive (399.8 nm) and first negative (427.8 nm) emissions, *J. Atmos. Terr. Phys.*, 60, 787, 1998.

Armstrong, R.A., D.M. Suszcynsky, W.A. Lyons and T.E. Nelson, Multi-color photometric measurements of ionization and energies in sprites, *Geophys. Res. Lett.*, 27, 653-656, 2000.

Armstrong, R.A.,D.M. Suszcynsky, W.A. Lyons, and E.A. Williams, Optical signatures, energy deposition, ionization and chemical dynamics in lightning-induced transient electrodynamics middle and upper atmospheric events (sprites), *Proc. URSI Nat. Radio Sci. Meeting* (Abstract), Boulder, 2001.

Baginski, M.E., L.C. Hale and J.J. Olivero, Lightning-related fields in the ionosphere, *Geophys. Res. Lett.*, 15, 764-767, 1996.

Barrington-Leigh, U.S. Inan, M. Stanley, and S. Cummer, Sprite directly triggered by negative lightning, *Geophys. Res. Lett.*, 26, 683-686, 1999.

Barrington-Leigh, C.P., C.P., Fast Photometric Imaging of High Altitude Optical Flashes Above Thunderstorms, Ph.D. Dissertation, Dept. of Electrical Engineering, Stanford University, Stanford, 2000.

Barrington-Leigh, C.P., U.S. Inan, and M. Stanley, Identification of sprites and elves with intensified video and broadband array photometry, *J. Geophys. Res.*, 106(A2), 1741-1750, 2001.

Bartels, R.H., and G.W. Stewart, The solution of the matrix equation AX - XB = C, *Comm. Assoc. Comp. Mach.*, 8, 820-826, 1972.

Bell T.F., V.P. Pasko, and U.S. Inan, Runaway electrons as a source of Red Sprites in the mesosphere, *Geophys. Res. Lett.*, 22, 2127-2130, 1995.

Bell, T.F., S.J. Reising, U.S. Inan, Intense continuing currents following positive cloud-to-ground lightning associated with red sprites, *Geophys. Res., Lett.*, 25, 1285-1288, 1998.

Boccippio, K.J., E.R.Williams, S.J.Heckman, W.A.Lyons, I.T.Baker, and R.Boldi, Sprites, ELF transients, and positive ground strokes, *Science*, 269, 1088, 1995.

Brasseur, G., and S. Solomon, *Aeronomy of the Middle Atmosphere*, 2nd ed., Reidel, Dordrecht, 1986.

Boeck, W., J. Vaughan, O.H., R. Blakeslee, B. Vonnegut, and M. Brook, Lightning induced brightening in the airglow layer, *Geophys. Res. Lett.*, 19, 99-102, 1992.

Bucsela, E., J. Morrill, C. Siefring, M. Heavner, D. Moudry, D. Sentman, E. Wescott, D. Osborne, and W. Benesch, Estimating electron energies in sprites from 1NG/2PG intensity ratios, *EOS Trans. Amer. Geophys. Union*, 81, A42-D04 (Abstract), 1998.

Cho, M., and M.J. Rycroft, Computer simulation of the electric field structure and optical emission from cloud-top to the ionosphere, *J. Atmos. Solar-Terr. Phys.*, 60, 871-888, 1998.

Cho, M., and R.J. Rycroft, Non-uniform ionization of the upper atmosphere due to the electromagnetic pulse from a horizontal lightning discharge, *J. Atmos. Solar-Terr. Phys.*, 63, 559-580, 2001.

Conforte, J.C., *A Study of Mesoscale Convective Complexes over South America and Neighbourhood* (in Portuguese), Ph.D. Dissertation, National Institute of Space Research (INPE), S. J. dos Campos, Brazil, 1997.

Cummer, S.A., and U.S. Inan, Measurements of charge transfer in Sprite-producing lightning using ELF radio atmospherics, *Geophys. Res., Lett.*, 24, 1731-1734, 1997.

Cummins, K.L.; M.J. Murphy, E.A. Bardo, W.L. Hiscox, R.B. Pyle, and A.E. Pifer, A combined TOA/MDF technology upgrade of U.S. National Lightning Detection Network. *J. Geophys. Res.*, 103, 9035, 1998a.

Cummins, K., E. Krider, and M. Malone, The US National Lightning Detection Network/sup TM/ and applications of cloud-to-ground lightning data by electric power utilities, *IEEE Transactions on Electromagnetic Compatibility*, 40, 465-80, 1998b.

Dejnakarintra, M. and C.G. Park, Lightning-Induced Electric Fields in the Ionosphere, *J. Geophys. Res.*, 79, 1903, 1974.

Dewan, E.M., and R.H. Picard, Mesospheric bores *J. Geophys. Res.*, 103 (D6), 6295-6305, 1998.

Dewan, E.M., R.H. Picard, R.R. O'Neil, H.A. Gardiner, J. Gibson, J.D. Mill, E. Richards, M. Kendra, and W.O. Gallery, MSX satellite observations of thunderstorm-generated gravity waves in midwave infrared images of the upper stratosphere. *Geophys. Res. Lett.* 25, 939–942, 1998.

Dewan, E.M., and R.H. Picard, On the origin of mesospheric bores *J. Geophys. Res.*, 106 (D3), 2921-2927, 2001.

Dowden, R.L., J.B. Brundell, W.A. Lyons, and T. Nelson, Detection and location of sprites by VLF phase scattering of subionospheric transmissions, *Geophys. Res. Let.*, 23, 1741-1744, 1996.

Dutton, J., A survey of electron swarm data, *J. Phys. Chem. Ref. Data*, 4, 577, 1975.

Fernsler, R.F., and H.R. Rowland, Models of lightning-produced sprites and elves, *J. Geophys. Res.*, 101, 29,653-29,659, 1996.

Fletcher, C.A.J., *Computational Techniques for Fluid Dynamics*, Springer, 1990.

Franz, R.C., R.J. Nemzek, and J.R. Winckler, Television image of a large upward electrical discharge above a thunderstorm system, *Science*, 249, 48-51, 1990.

Fritts, D.C., Gravity wave saturation in the middle atmosphere: A review of theory and observations, *Rev. Geophys. Space Sci.*, 22, 275, 1984.

Fritts, D.C., J.R. Isler, J.H. Hecht, R.L. Walterscheid, and Ø. Andreassen, Wave Breaking signatures in sodium densities and OH nightglow 2. Simulation of wave and instability structures, *J. Geophys. Res.*, 102, 6669-6684, 1997.

Fuellekrug, M., Estimation of sprite occurrence densities in central Africa by infrared satellite imagery, *Proceedings of IAGA-IASEI Joint Scientific Assembly*, Hanoi, Vietnam, p. 99, Aug. 2001.

Fukunishi, H., Y. Takahashi, M. Fujito, Y. Watanabe, and K. Sakanoi, Fast imaging of elves and sprites using a framing / streak camera and a multi-anode array photometer, in *EOS Trans. Amer. Geophys. Union*, 77, F60 (Abstract), 1996a.

Fukunishi, H., Y. Takahashi, M. Kubota, K. Sakanoi, U. Inan, and W. Lyons, Elves: lightning-induced transient luminous events in the lower ionosphere, *Geophys. Res. Lett.*, 23, 2157-60, 1996b.

Fukunishi, H., Y. Takahashi, A. Uchida, M. Sera, K. Adachi, and R. Miyasato, Occurrences of sprites and elves above the Sea of Japan near Hokuriku in Winter. *EOS Trans. Amer. Geophys. Union*, 80, F55 (Abstract),1999.

Fukunishi, H., Y. Takahashi, T. Adachi and R. Miyasato, Characteristics of sprites and Elves observed in winter above Japan, *Proc. IAGA-IASEI Joint Scientific Assembly*, Hanoi, Vietnam, p. 98, Aug. 2001.

Gerken, E. A., U. S. Inan, C. P. Barrington-Leigh, Telescopic imaging of sprites, *Geophys. Res. Lett.*, 27(17), 2637-2640, 2000.

Goodman, S.J. and D.R. MacGorman, Cloud-to-Ground Lightning Activity in Mesoscale Convective Complexes, *Mon. Weath. Rev.*, 114, 2320, 1986.

Greifinger, C., and P. Greifinger, Transient ULF electric and magnetic fields following a lightning discharge, *J. Geophys. Res.*, 81, 2237, 1976.

Groves, K.M., J.V. Rodriguez, J.M. Quinn, P.J. Erickson, M. Cox, and T. Arce, RF measurements of lightning-induced ionospheric effects, *Proc. URSI Nat. Radio Sci. Meeting*, GH5-5 (Abstract), Boulder, 1996.

Hampton, D. L., M. J. Heavner, E. M. Wescott, and D. D. Sentman, Optical spectral characteristics of sprites, *Geophys. Res. Lett.*, 23, 89-92, 1996.

Heavner, M.J., *Optical Spectroscopic Observations of Sprites, Blue Jets, and Elves: Inferred Microphysical Processes and Their Macrophysical Implications*, Ph.D. Dissertation, Department of Physics, University of Alaska, 2000a.

Heavner, M.J., D.D. Sentman, D.R. Moudry, E.M. Wescott, C.L. Siefring, J.S. Morrill, and E.J. Bucsela, "Sprites, Blue Jets, and Elves: Optical Evidence of Energy Transport Across the Stratopause," in *Atmospheric Science Across the Stratopause*, . (D. Siskind, Ed.), American Geophysical Union, Washington DC, 2000b.

Hecht, J.H., R.L. Walterscheid, D.C. Fritts, J.R. Isler, D.C. Senft, C.S. Gardner, and S.J. Franke, Wave breaking signatures in OH airglow and sodium densities and temperature 1. Airglow imaging, Na lidar, and MF radar observations, *J. Geophys. Res.*, 102, 6655-6668, 1997.

Hecht, J.H., C. Fricke-Begemann, R.L. Walterscheid, and J. Höffner, Observations of the breakdown of an atmospheric gravity wave near the cold summer mesopause at 54N, *Geophys. Res. Lett.*, 27, 879-882, 2000.

Hines, C.O., Internal atmospheric gravity waves at ionospheric heights, *Can. J. Phys.*, 38, 1441, 1960.

Holzworth, R.H., M.C. Kelley, C.L. Siefring, L.C. Hale and J.D. Mitchell, Electrical measurements in the atmosphere and the ionosphere over an active thunderstorm. 2.

Direct current electric fields and conductivity, *J. Geophys. Res.*, 90(A10), 9824-9830, 1985.

Inan, U.S., T.F. Bell, V.P. Pasko, D.D. Sentman, and E.M. Wescott, and W.A. Lyons, VLF signatures of ionospheric disturbances associated with sprites, *Geophys. Res. Lett.*, 22, 3461-3464, 1995.

Inan, U. S., V. P. Pasko, and T. F. Bell, Early/Fast VLF events as evidence of sustained heating of the ionosphere above thunderclouds, *Geophys. Res. Lett.*, 23, 1067-1070, 1996.

Inan, U.S., C. Barrington-Leigh, S. Hansen, V.S. Glukhov, T.F. Bell, and R. Rairden, Rapid lateral expansion of optical luminosity in lightning-induced ionospheric flashes referred to as "elves", *Geophys. Res. Lett.*, 24, 583-586, 1997.

Krassovsky, V.I., Infrasonic variations of OH emission in the upper atmosphere. *Ann. Geophys.*, 28, 739, 1972

Larsen, M.F., W.E. Swartz, and R.F. Woodman, Gravity-wave generation by thunderstorms observed with a vertically-pointing 430 MHz radar, *Geophys. Res., Lett.*, 9, 571-574, 1982.

Larsen, M.F., A.Z. Liu, C.S. Gardner, M.C. Kelley, S. Collins, J. Friedman, and J.H. Hecht, Observations of overturning in the upper mesosphere and lower thermosphere, *J. Geophys. Res.*, (submitted), 2003.

Liu, A.Z., and G.R. Swenson, A modeling study of O_2 and OH airglow perturbations induced by atmospheric gravity waves, *J. Geophys. Res.* 108(D4), ACH 11-1 to 11-9, 2003.

Lübken, F.-J., M. Rapp, and P. Hoffman, Neutral air turbulence and temperatures in the vicinity of polar mesosphere summer echoes, *J. Geophys. Res.*, 107(D15), ACL 9-1 to 9-10, 2002.

Lummerzheim, D., *Electron Transport and Optical Emissions in the Aurora*, Ph.D. Dissertation, University of Alaska Fairbanks, Fairbanks, 1987.

Lyons, W. A., Sprite observations above the U.S. High Plains in relation to their parent thunderstorm systems, *J. Geophys. Res.*, 101, 29641, 1996.

Lyons, W. A., R. A. Armstrong, E. R. Williams and E. A. Bering, "The Hundred Year Hunt for the Sprite," *EOS Trans. Amer. Geophys. Union*, 81(33), 373-377, 2000.

Maddox, R. A., Mesoscale convective complexes, *Bull. Am. Meteorol. Soc.*, 61, 1374-1387, Nov. 1980.

Maynard, N.C., C.L. Croskey, J.D. Mitchell, and L.C. Hale, Measurement of volt/meter vertical electric fields in the middle atmosphere, *Geophys. Res. Lett.*, 8(8), 923-926, 1981.

Matthews, J.D., Q. Zhou, C.R. Philbrick, Y.T. Morton, and C.S. Gardner, Observations of ion and sodium layer coupled processes during AIDA, *J. Atmos. Terr. Phys.*, 55, 487, 1993.

Medeiros, A.F, "Observações de Ondas de Gravidade Através do Imageamento da Aeroluminescência", (Gravity Wave Observations through Airglow Imaging), *Ph.D. Dissertation, Instituto Nacional de Pesquisas Espaciais (INPE)*, São José dos Campos, SP, Brazil, Sept. 2001.

Mende, S. B., R. L. Rairden, G. R. Swenson, and W. A. Lyons, Sprite spectra: N2 1 PG band identification, *Geophys. Res. Lett.*, 22, 2633-2636, 1995.

Milikh, G.M., K. Papadopoulos, C.L. Chang, On the physics of high altitude lightning, *Geophys. Res. Lett.*, 22, 85-88, 1995.

Morrill, J.S., E.J. Buscela, V.P. Pasko, S.L. Berg, M.J. Heavner, D.R. Moudry, W.M. Benesch, E.M. Wescott, and D.D. Sentman, Time resolved N_2 triplet state vibrational populations and emissions associated with red sprites, *J. Atmos. Solar-Terr. Phys.*, 60, 811-830, 1998.

Moudry, D.R., M.J. Heavner, D.D. Sentman and E.M. Wescott, Sprites over small storms, *EOS Trans. Am. Geophys. Union*, 78(46), F83, 1997.

Moudry, D. R., H.C. Stenbaek-Nielsen, D.D. Sentman and E.M. Wescott, 1 ms time development of upper atmospheric flashes, *Proc. URSI Nat. Radio Sci. Meeting* (Abstract), Boulder, 2001.

Moudry, D.R., *The Dynamics and Morphology of Sprites*, Ph.D. Dissertation, Physics Department, University of Alaska, Fairbanks, Alaska, 2003.

Neubert, T., T.H. Allin, H. Stenbaek-Nielsen, E. Blanc, Sprites over Europe, *J. Geophys. Res. Lett.*, 28, 3585-3588, 2001.

Papadopoulos, K., G. Milikh, A. Gurevich, A. Drobot, and R. Shanny, Ionization rates for atmospheric and ionospheric breakdown, *J. Geophys. Res.*, 98, 17593, 1993.

Pasko, V., U. Inan, Y. Taranenko, and T. Bell, Heating, ionization and upward discharges in the mesosphere due to intense quasi-electrostatic thundercloud fields, *Geophys. Res. Lett.*, 22, 365-368, 1995

Pasko, V.P., U.S. Inan, and T.F. Bell, Sprites as luminous columns of ionization produced by quasi-electrostatic thundercloud fields, *Geophys. Res. Lett.*, 23, 649-652, 1996.

Pasko, V.P., U.S. Inan, and T.F. Bell, Sprites as evidence of vertical gravity wave structures above mesoscale thunderstorms, *Geophys. Res. Lett.*, 24, 1735-1738, 1997a.

Pasko, V.P., U.S. Inan and T.F. Bell, Sprites produced by Quasi-electrostatic heating and ionization in the lower ionosphere, *J. Geophys. Res.*, 102, 4529, 1997b.

Pasko, V. P.; Inan, U. S.; Bell, T. F., Spatial structure of sprites, *Geophys. Res. Lett.*, 25(12), 2123-2126, 1998.

Pasko, V.P., M.A. Stanley, J.D. Mathews, U.S. Inan, and T.G. Wood, Electrical discharge from a thundercloud top to the lower ionosphere, *Nature*, 416, 152, 14 March, 2002.

Picard, R.H., R.R. O'Neil, H.A. Gardiner, J. Gibson, J.R. Winick, W.O. Gallery, A.T. Stair Jr., P.P. Wintersteiner, E.R. Hegblom, and E. Richards, Remote sensing of

discrete stratospheric gravity-wave structure at 4.3 μm from the MSX satellite, *Geophys. Res. Lett.*, 25, 2809–2812, 1998.

Pierce, A.D., and S.C. Coroniti, A mechanism for the generation of acoustic-gravity waves during thunderstorm formation, *Nature*, 210, 1209, 1966.

Pinto Jr., O., and Pinto, I.R.C.A., *Relâmpagos*, São Paulo: Editora Brasiliense, 1996.

Raizer, Yu.P., *Gas Discharge Physics*, Springer, Berlin, 1991.

Raizer, Yu.P., G.M. Milikh, M.N. Shneider, and S.V. Novakovski, Long streamers in the upper atmosphere above a thundercloud, *J. Phys. D: Appl. Phys.*, 31, 3255-3264, 1998.

Rees, M.H., *Physics and Chemistry of the Upper Atmosphere*, Cambridge University Press, Cambridge, 1989.

Reising, S.C., U.S. Inan, T.F. Bell, and W.A. Lyons, Evidence for continuing current in sprite-producing cloud-to-ground lightning, *Geophys. Res. Lett.*, 23, 3639-3642, 1996.

Roussel-Dupré, R.A., and A.V. Gurevich, On runaway breakdown and upward propagating discharges, *J. Geophys. Res.*, 101, 2297, 1996.

Rowland, H.L., R.F. Fernsler, J.D. Huba, and P.A. Bernhardt, Lightning driven EMP in the upper atmosphere, *Geophys. Res. Lett.*, 22, 361-364, 1995.

Rowland, H.L., R.F. Fernsler, and P.A. Bernhardt, Breakdown of the neutral atmosphere in the D-region due to lightning driven electromagnetic pulses, *J. Geophys. Res.*, 101, 7935, 1996.

São Sabbas, F. T., *Study of the relationship between Sprites and lightning from the associated storms* (in Portuguese). Master dissertation, Instituto Nacional de Pesquisas Espaciais (INPE), São José dos Campos, SP, Brazil, Feb. 1999a.

São Sabbas, F T, Pinto, O , Mendes, O , Taylor, M J, Sentman, D D, Wescott, E M, Characteristics of sprite-associated lightning and total lightning," *EOS Trans. Am. Geophys. Union*, 80, F226 (Abstract), 1999b.

São Sabbas, F. T., D.D. Sentman, E.M. Wescott, O. Pinto Júnior, O. Mendes Júnior and M. J. Taylor, Statistical analysis of space-time relationships between sprites and lightning, *J. Atmos. Solar-Terr. Phys.*, 65(5), 523-533, 2003a.

São Sabbas, F. T., and D.D. Sentman, Dynamical relationship of infrared cloudtop temperatures with occurrence rates of cloud-to-ground lightning and sprites, *Geophys. Res. Lett.*, 30(5), 40-1 to 40-4, 2003b.

Sentman, D. D.; Wescott, E. M.; Osborne, D. L.; Hampton, D. L. and Heavner, M. J. Preliminary results from the Sprites94 aircraft campaign: 1. Red sprites. *Geophys. Res. Lett.*, 22, 1205-1208, 1995a.

Sentman, D., and E. Wescott, Red sprites and blue jets: thunderstorm-excited optical emissions in the stratosphere, mesosphere, and ionosphere, *Phys. Plasmas*, 2, 2514-22, 1995b.

Sentman, D.D., E.M. Wescott, D.L. Osborne, M.J. Heavner and D.L. Hampton, The Peru95 Sprites Campaign: Overview, *EOS Trans. AGU*, 76, F238, (Abstract), 1995c.

Sentman, D. D., D. R. Moudry, H. C. Stenbaek-Nielsen, E. M. Wescott, and F. T. São Sabbas, Electrical field effects on chemical reaction rates within sprites, *EOS Trans. Amer. Geophys. Union*, 81, F130 (Abstract), 2000.

Sentman, D.D. and F. T. São Sabbas, Comparison of South American and African diurnal signatures in the Schumann resonances with satellite infrared Images", *Proceedings of Vietnam 2001 IAGA-IASPEI Joint Scientific Assembly*, paper G2.01[2624], p 100, Hanoi, Vietnam, August, 2001.

Sentman, D.D., E.M. Wescott, R.H. Picard, J.R. Winick, H.C. Stenbaek-Nielsen, E.M. Dewan, D.R. Moudry, F.T. São Sabbas, M.J. Heavner, and J. Morrill, Simultaneous observations of mesospheric gravity waves and sprites generated by a midwestern thunderstorm, *J. Atmos. Solar-Terr. Phys.*, (in press), 2003.

Siefring, C. L., J. S. Morrill, D. D. Sentman, D. R. Moudry, E. M. Wescott, M. J. Heavner, D. L. Osborne and E. J. Bucsela, Do sprites sometimes connect to the cloud tops?, *EOS Trans. Amer. Geophys. Union*, *80*, F225 (Abstract), 1999.

Stanley, M., P. Krehbiel, M. Brook, C. Moore, W. Rison, and B. Abrahams, High speed video of initial sprite development, *Geophys. Res. Lett.*, 26, 3201-3204, 1999

Stanley, M., M. Brook, P. Krehbiel, and S. A. Cummer, Detection of daytime sprites via a unique sprite ELF signature, *Geophys. Res. Lett.*, 27, 871-874, 2000.

Stenbaek-Nielsen, H.C., D.R. Moudry, E.M. Wescott, D.D. Sentman, and F.T. São Sabbas, Sprites and possible mesospheric effects, *Geophys. Res. Lett.*, 27(23), 3829-3932, 2000.

Stull, R.B., Internal gravity waves generated by penetrative convection, *J. Atmos. Sci.*, 33, 1279, 1976.

Suszcynsky, D.M., R.A. Roussel-Dupré, W.A. Lyons, and R.A. Armstrong, Blue light imagery and photometry of sprites. *J. Atmos. Solar-Terr. Phys.*, 60, 801, 1998.

Symbalisty, E.M.D., R.A. Roussel-Dupré, D.O. ReVelle, D.M. Syszcynsky, and V. Yukhimuk, Meteor trails and columniform sprites, *Icarus*, 148(1), 65, 2000.

Su, H.T., R.R. Hsu, A.B. Chen, Y.J. Lee and L C. Lee, Observations of sprites over the Asian continent and over oceans around Taiwan, *Geophys. Res. Lett.*, 29, 1-4, 2002.

Takahashi, U., Y. Watanabe, A. Uchida, M. Sera, M. Sato, and H. Fukunishi, Energy distributions of electrons exciting sprites and elves inferred from the Fast Array Photometer observations, *EOS Trans. Amer. Geophys. Union*, 79, F175 (Abstract), 1998.

Taranenko, Y.N. U.S. Inan and T.F. Bell, Interaction with lower ionosphere of electromagnetic pulses from lightning: Heating, attachment, and ionization, *Geophys. Res. Lett.*, 20(15, 1539-1542, 1993.

Taranenko, Y., and R. Roussel-Dupre, High altitude discharges and gamma-ray flashes: a manifestation of runaway air breakdown, *Geophys. Res. Lett.*, 23, 571-574, 1996.

Taylor, M.J., Hapgood, M.A., Identification of a thunderstorm as a source of short period gravity waves in the upper atmospheric nightglow emissions, *Planet. Space Sci.*, 36, 975–985, 1988.

Taylor, M.J., D.N. Turnbull, and R.P. Lowe, Coincident imaging and spectrometric observations of zenith OH nightglow structure, *Geophys. Res. Lett.*, 18, 1349–1352, 1991.

Taylor, M.J. L.C. Gardner, C. Siefring, Image measurements during the 1999 Leonids-MAC Airborne Campaign: High-resolution meteor ablation signatures and longitudinal gravity wave study, *Proc. 2nd Leonids-MAC workshop* (Abstract), Tel Aviv, April, 2000.

Tsuda, T., M. Nishida, C. Rocken and R. Ware, A global morphology of gravity wave activity in the stratosphere revealed by the GPS occultation data (GPS/MET), *J. Geophys. Res.*, 105(D6), 7257-7273, 2000.

Uman, M.A, *The Lightning Discharge*, Academic Press, London, 1987.

Valdivia, J., G. Milikh, and K. Papadopoulos, Red sprites: Lightning as a fractal antenna, *Geophys. Res. Lett.*, 24(24), 3169-3172, 1997.

Velasco, I. and J.M. Fritsch, Mesoscale convective complexes in the Americas, *J. Geophys. Res.*, 92, 9591, 1987.

Walterscheid, R.L., and G. Schubert, Nonlinear evolution of an upward propagating gravity wave: Overturning, convection, transience and turbulence, *J. Atmos. Sci.*, 47, 101, 1990.

Weinreb, M.P., J.X. Johnson and D. Han, "Conversion of GVAR Infrared Data to Scene Radiance or Temperature", *NOAA NESDIS Office of Satellite Operations*, Boulder, Colorado, Revised, June, 2001.

Wescott, E.M., D. Sentman, D. Osborne, D. Hampton, and M. Heavner, Preliminary results from the Sprites94 aircraft campaign: 2. Blue jets, *Geophys. Res. Lett.*, 22, 1209-1212, 1995a.

Wescott, E.M, D.D. Sentman, D.L. Osborne, M.J. Heavner and D.J. Hampton , The Peru95 Sprites campaign: Aircraft video observations of equatorial sprites," *EOS Trans. Amer. Geophys. Union,* 76, F238 (Abstract), 1995b.

Wescott, E.M., D. Sentman, D. Hampton, M. Heavner, D. Osborne, and O. Vaughan, Blue starters and lightning discharges from an intense thunderstorm over Arkansas, July 1, 1994, *Geophys. Res. Lett.,* 23, 2153-2156, 1996.

Wescott, E. M., D.D. Sentman, M.J. Heavner, D.L. Hampton, and O.H. Vaughan Jr., Blue Jets: Their relationship to lightning and very large hailfall, and physical mechanisms for their production, *J. Atmos. Solar-Terr. Phys.,* 60, 713-724, 1998a.

Wescott, E.M., D.D. Sentman, M.J. Heavner, D.L. Hampton, W.A. Lyons, and T. Nelson, Observations of "Columniform" sprites, *J. Atmos. Solar-Terr. Phys.,* 60, 733-740, 1998b.

Wescott, E.M., H.C. Stenbaek-Nielsen, D.D. Sentman, M.J. Heavner, D.R. Moudry, and F.T. São Sabbas, Triangulation of sprites, associated halos and their possible relation to causative lightning and micro-meteors, *J. Geophys. Res.,* 106(A6), 10,467-10,477, 2001.

Yamada, Y., Fukunishi, H., Nakamura, T., Tsuda, T., Breaking of small-scale gravity wave and transition to turbulence observed in OH airglow, *Geophys. Res. Lett.,* 28(11), 2153-2156, 2001.

Yukhimuk, V., R.A. Roussel-Dupre, E.M. D. Symbalisty, and Y. Taranenko, Optical characteristics of Red Sprites produced by runaway air breakdown, *J. Geophys. Res.,* 103, 11,473-11,482, 1998.

Zabotin, N.A., and J.W. Wright, Role of meteoric dust in sprite formation, *Geophys. Res. Lett.,* 28(13),2593-2596, 2001.
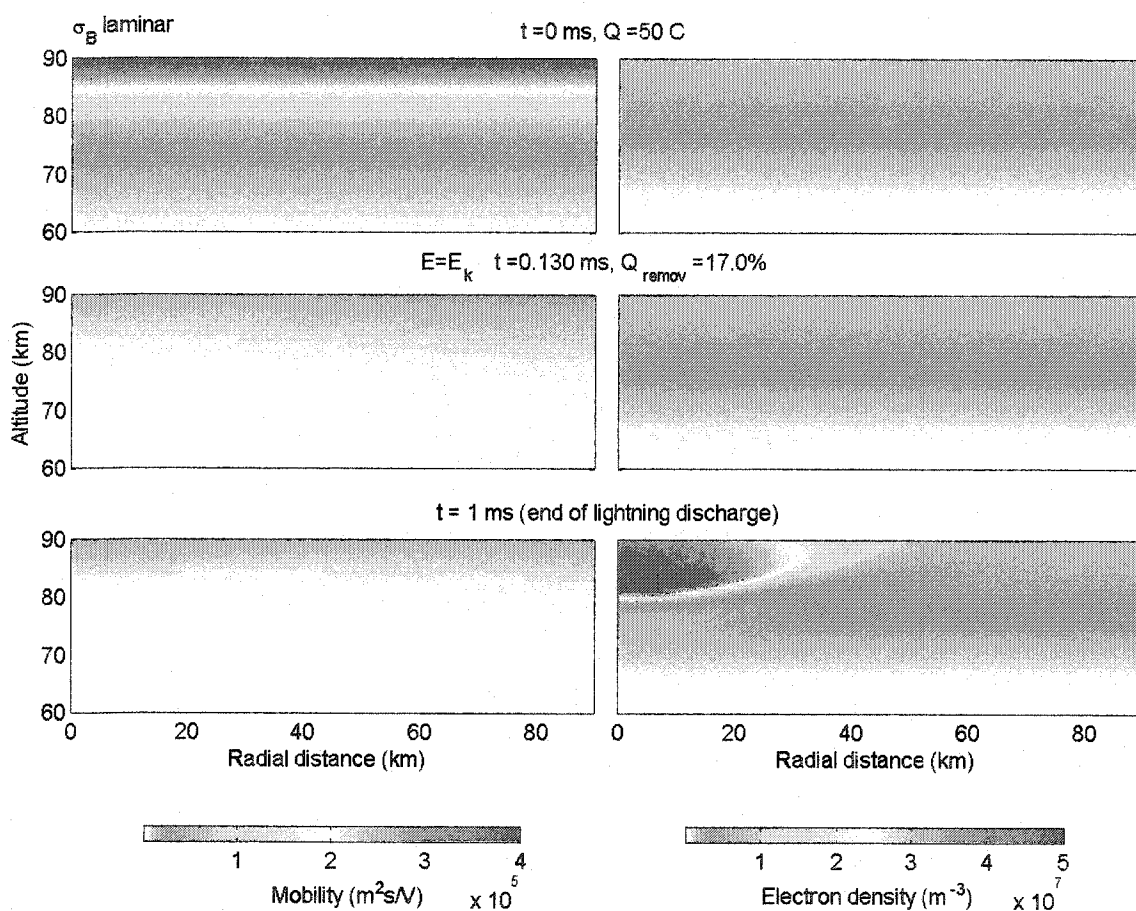
APPENDIX A

LAMINAR CONDUCTIVITY PROFILE σ_B AND PERTURBED

CASES NUMBER 2, 3, 6 AND 7

Figure A-1 Electron mobility, left, and electron density, right, for $Q = 50$ C and laminar conductivity profile σ_B. The first row is at $t = 0$ ms (pre-lightning), the second row is at breakdown ($E = E_k$) and the last row is at the end of the positive lightning discharge ($t = 1$ ms). The instance when breakdown first occurs and percentage of the total charge removed (Q_{remov}) at that time are indicated above each panel in the middle row.
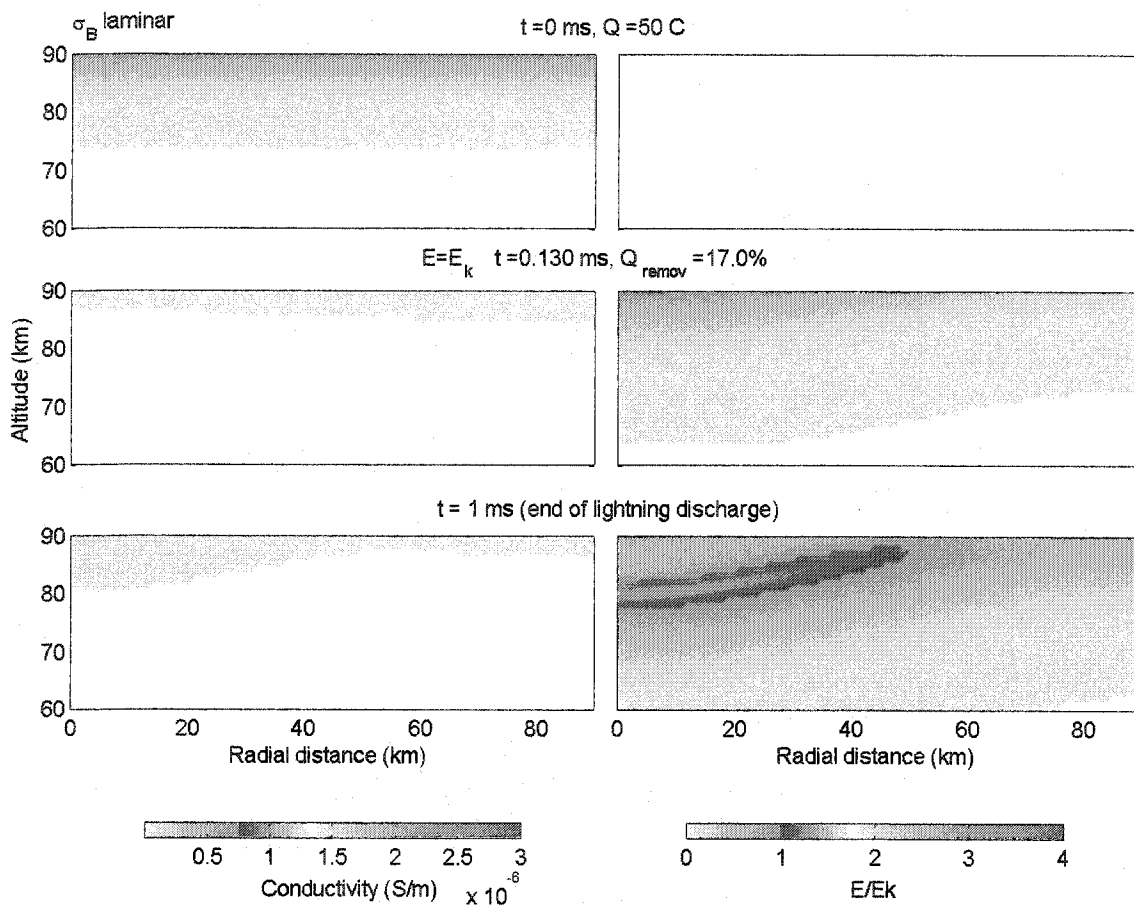
Figure A-2 Total conductivity, left, and E_{tot}/E_k, right, for $Q = 50$ C and laminar conductivity profile σ_B. The first row is at $t = 0$ ms (pre-lightning), the second row is at breakdown ($E = E_k$) and the last row is at the end of the positive lightning discharge ($t = 1$ ms). The instance when breakdown first occurs and percentage of the total charge removed (Q_{remov}) at that time are indicated above each panel in the middle row.
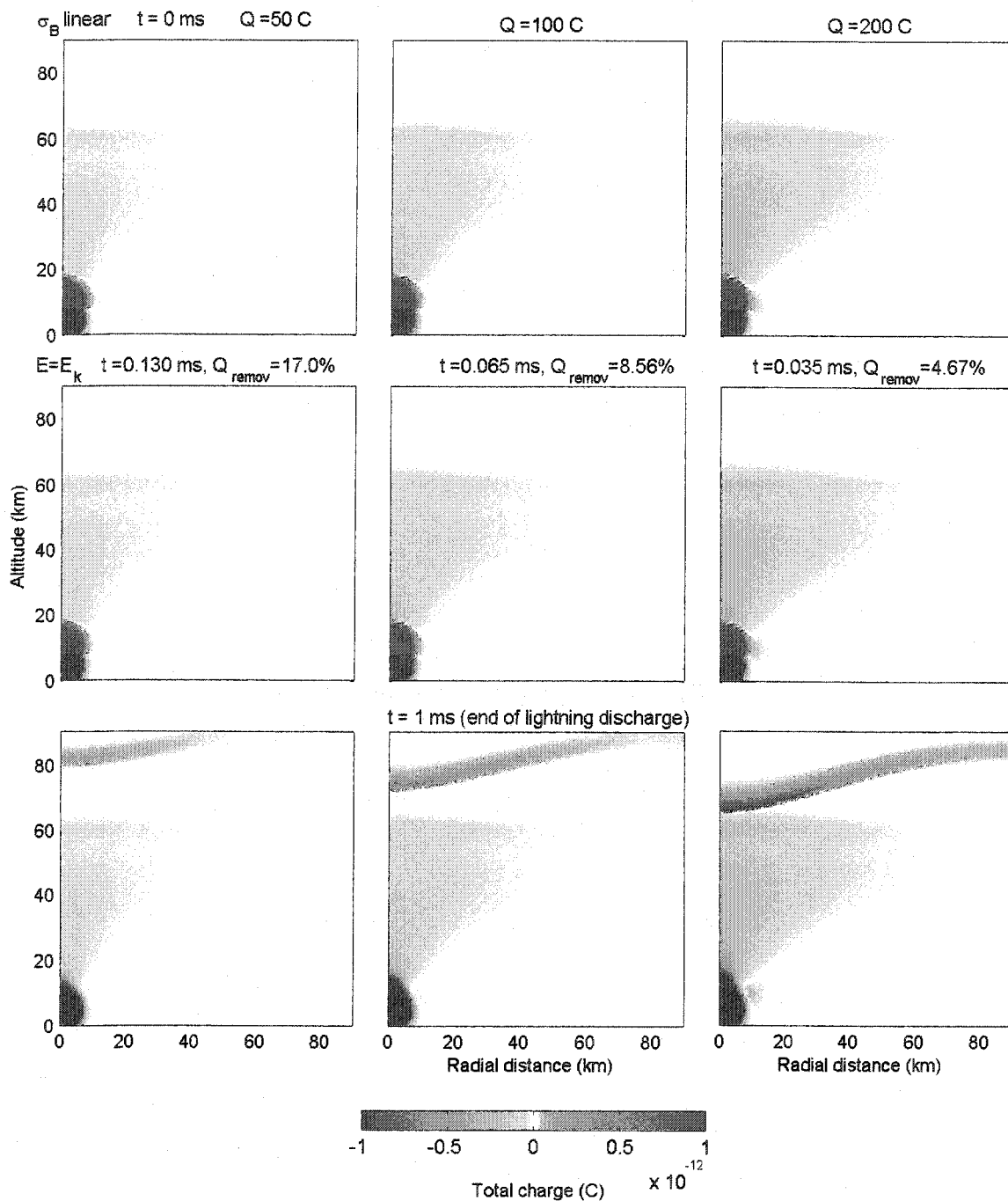
Figure A-3 Total charge density for Q = 50, 100, 200 C and σ_B. Refer to Table 4.2 for further details. The first row shows t = 0 ms, the middle row shows when $E_{tot} = E_k$ for the first time, and the last row shows t = 1 ms. The percentage of the total charge removed (Q_{remov}) and breakdown time are indicated above the middle row figures. Notice that the control case (left column) does breakdown.
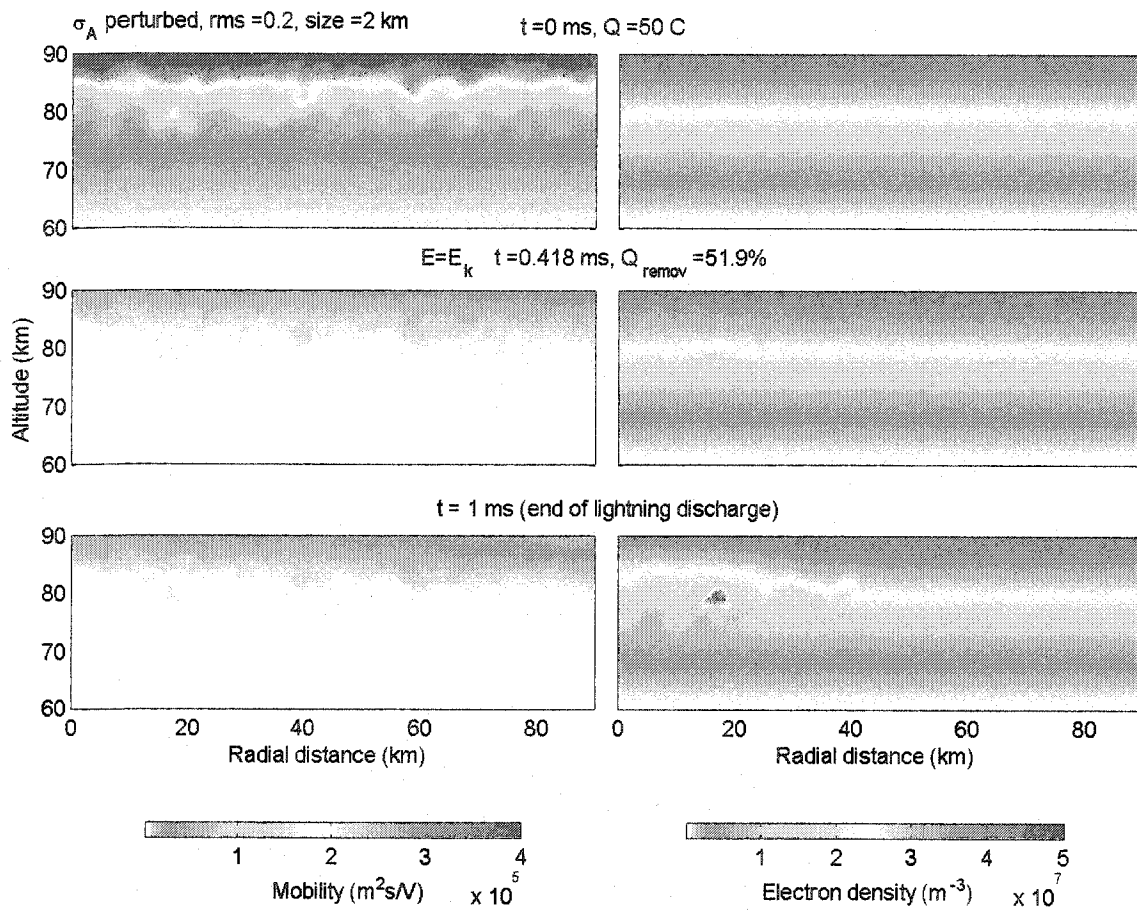
Figure A-4 Electron mobility (left) and electron density (right) for perturbed case 2. The first row shows t = 0 ms, the second row shows when $E_{tot} = E_k$ for the first time, and the third row shows t = 1 ms. The percentage of the total charge removed (Q_{remov}) and breakdown time are indicated above the middle row panel. Case 2 is the control case with input perturbations parameters A_{pert} = 0.2 and $size_{pert}$ = 2 km.

Figure A-5 Conductivity (left) and E_{tot}/E_k (right) for perturbed case 2. The first row shows $t = 0$ ms, the second row shows when $E_{tot} = E_k$ for the first time, and the third row shows $t = 1$ ms. The percentage of the total charge removed (Q_{remov}) and breakdown time are indicated above the middle row panel. Case 2 is the control case with input perturbations parameters $A_{pert} = 0.2$ and $size_{pert} = 2$ km.
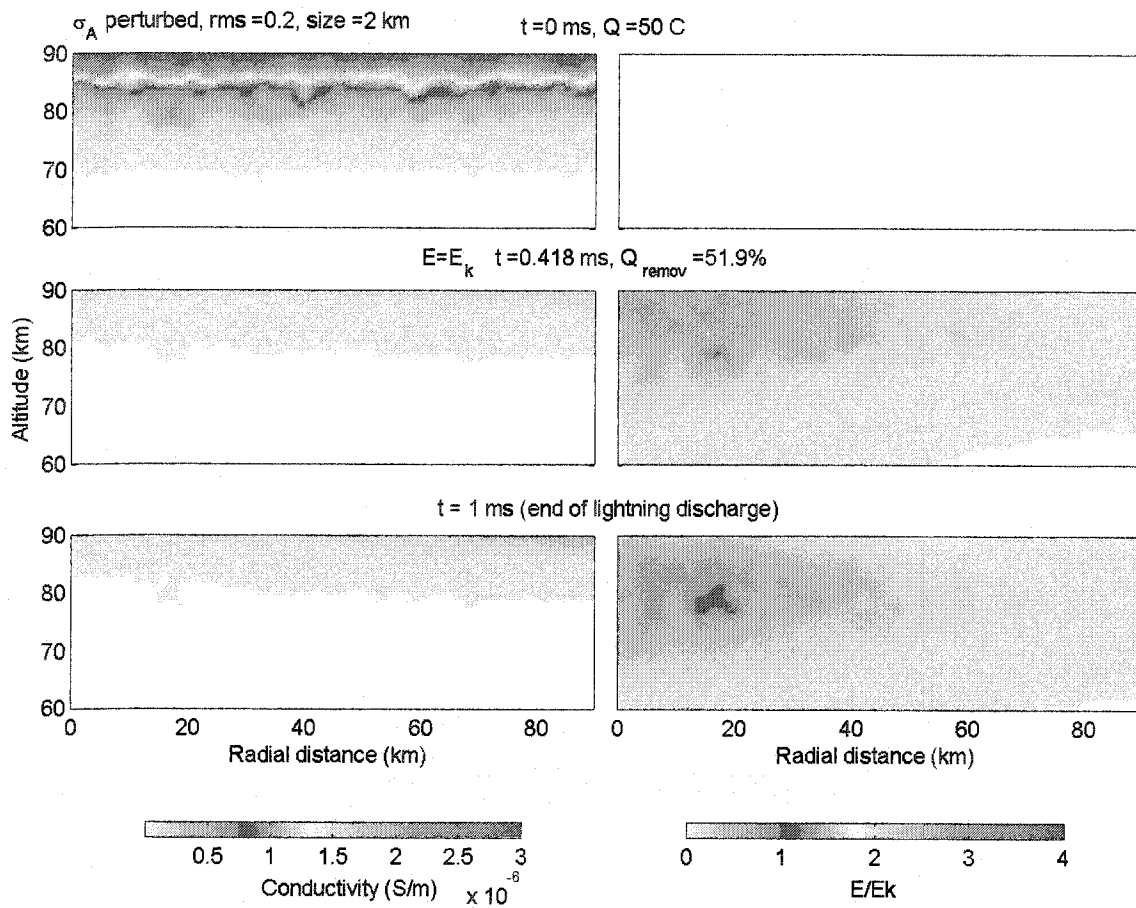
Figure A-6 Electron mobility (left) and electron density (right) for perturbed case 3. The first row shows t = 0 ms, the second row shows when $E_{tot} = E_k$ for the first time, and the third row shows t = 1 ms. The percentage of the total charge removed (Q_{remov}) and breakdown time are indicated above the middle row panel. Case 3 is the control case with input perturbations parameters A_{pert} = 0.2 and $size_{pert}$ = 5 km.

Figure A-7 Conductivity (left) and E_{tot}/E_k (right) for perturbed case 3. The first row shows $t = 0$ ms, the second row shows when $E_{tot} = E_k$ for the first time, and the third row shows $t = 1$ ms. The percentage of the total charge removed (Q_{remov}) and breakdown time are indicated above the middle row panel. Case 3 is the control case with input perturbations parameters $A_{pert} = 0.2$ and $size_{pert} = 5$ km.
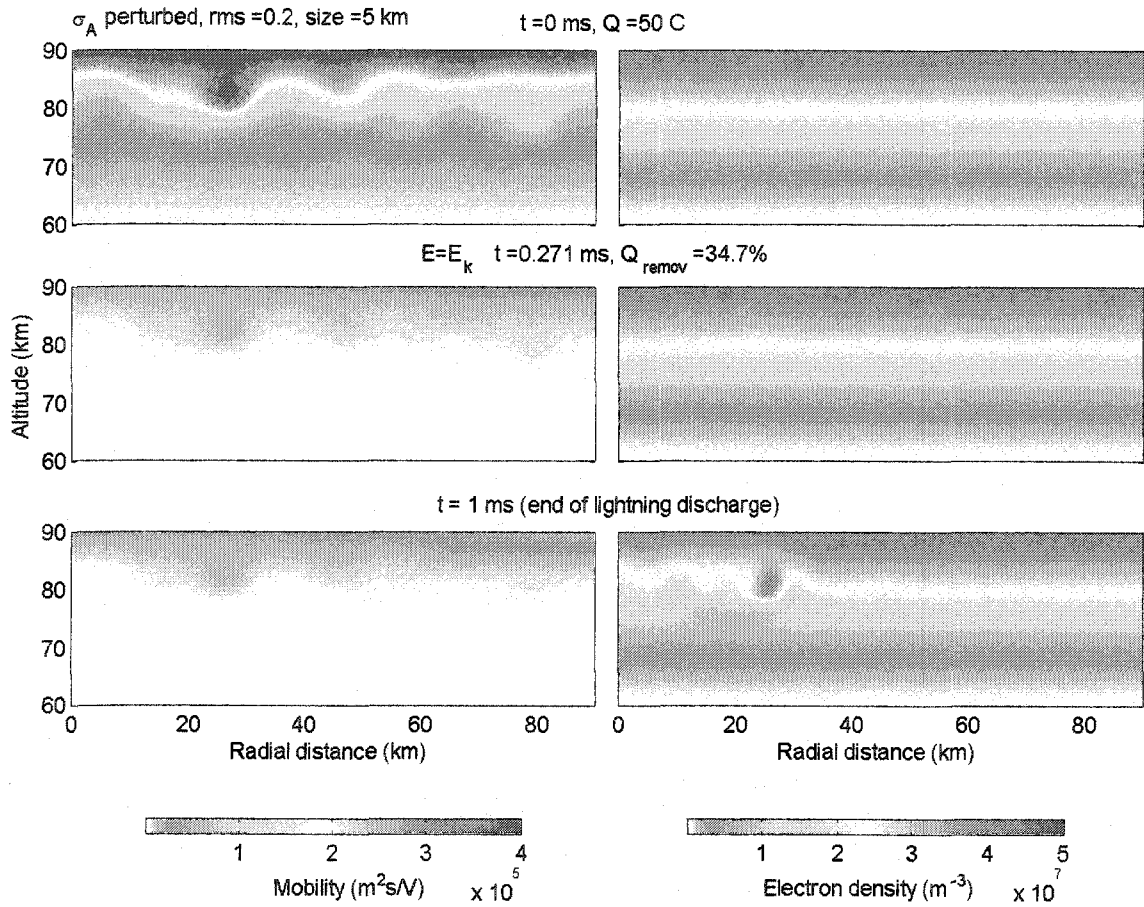
Figure A-8 Electron mobility (left) and electron density (right) for perturbed case 6. The first row shows t = 0 ms, the second row shows when $E_{tot} = E_k$ for the first time, and the third row shows t = 1 ms. The percentage of the total charge removed (Q_{remov}) and breakdown time are indicated above the middle row panel. Case 6 is the control case with input perturbations parameters A_{pert} = 0.4 and $size_{pert}$ = 2 km.
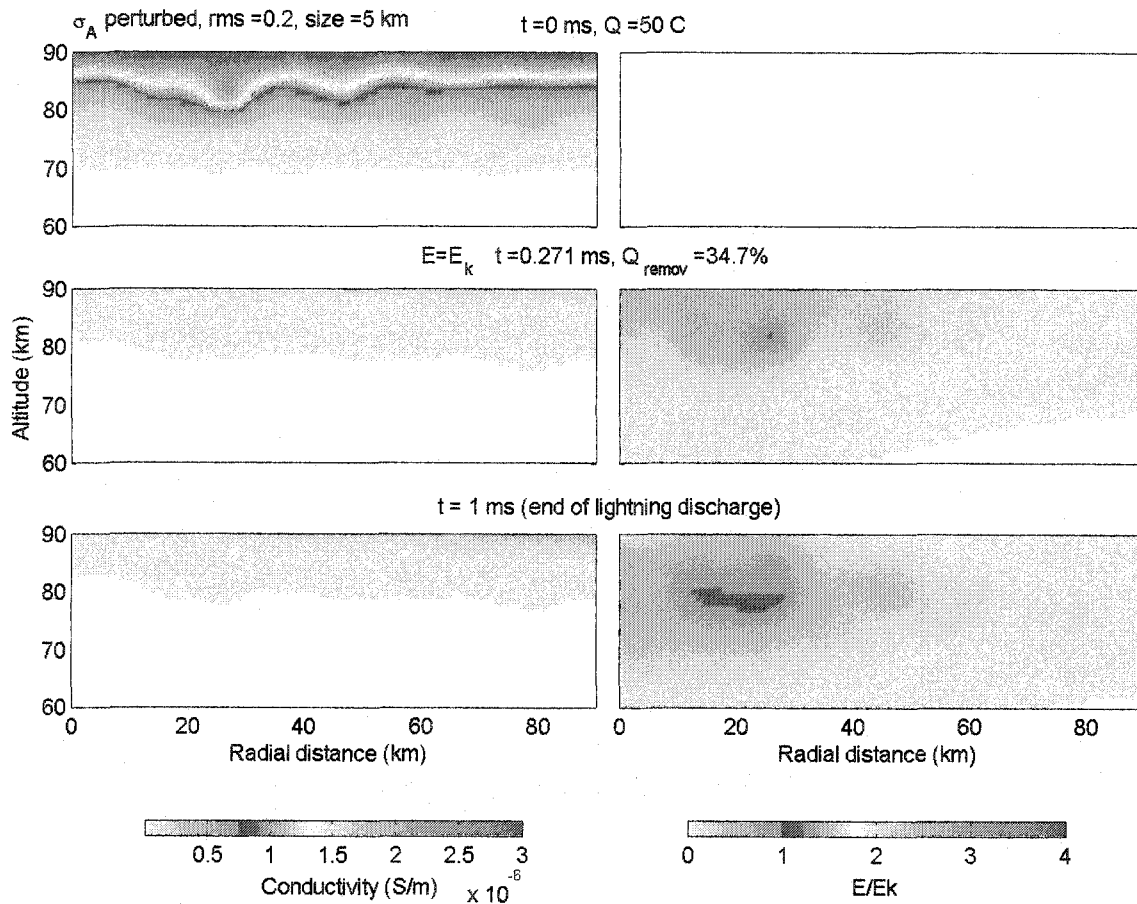
Figure A-9 Conductivity (left) and E_{tot}/E_k (right) for perturbed case 6. The first row shows $t = 0$ ms, the second row shows when $E_{tot} = E_k$ for the first time, and the third row shows $t = 1$ ms. The percentage of the total charge removed (Q_{remov}) and breakdown time are indicated above the middle row panel. Case 6 is the control case with input perturbations parameters $A_{pert} = 0.4$ and $size_{pert} = 2$ km.
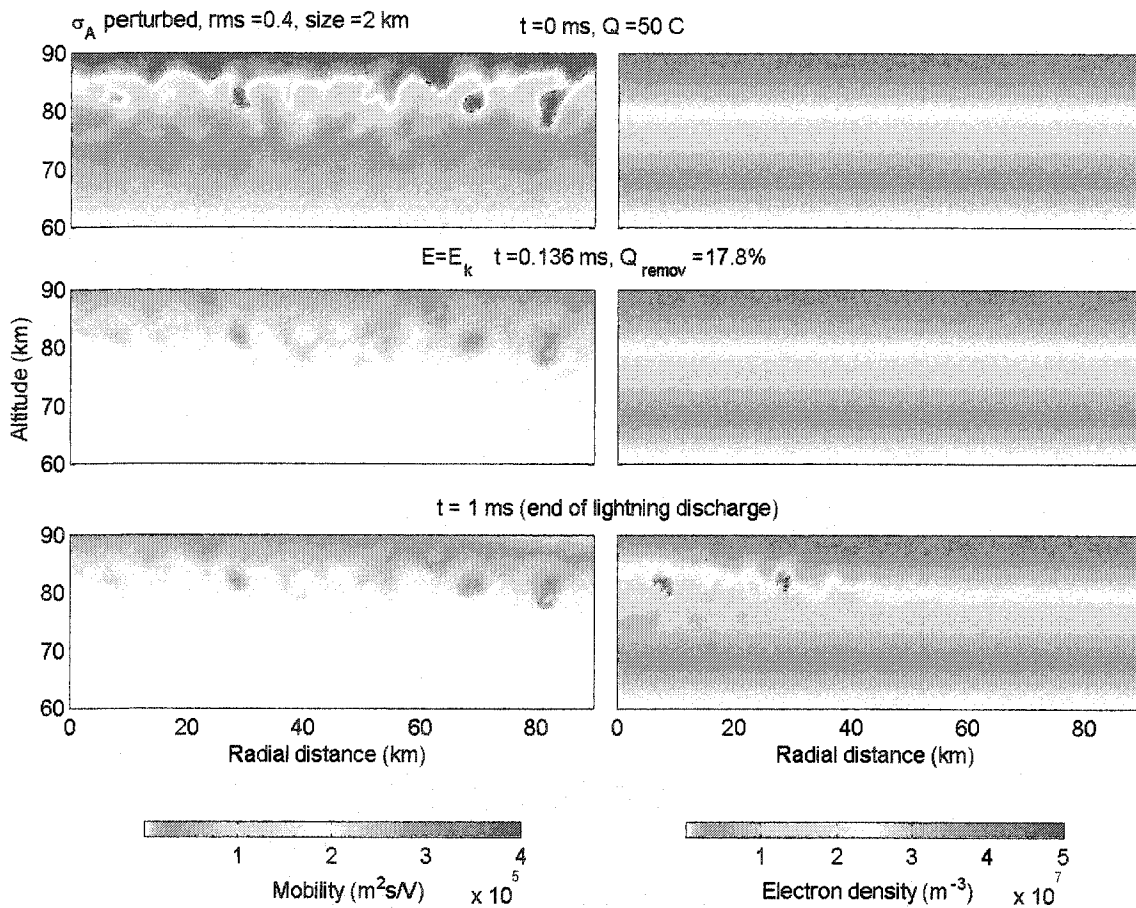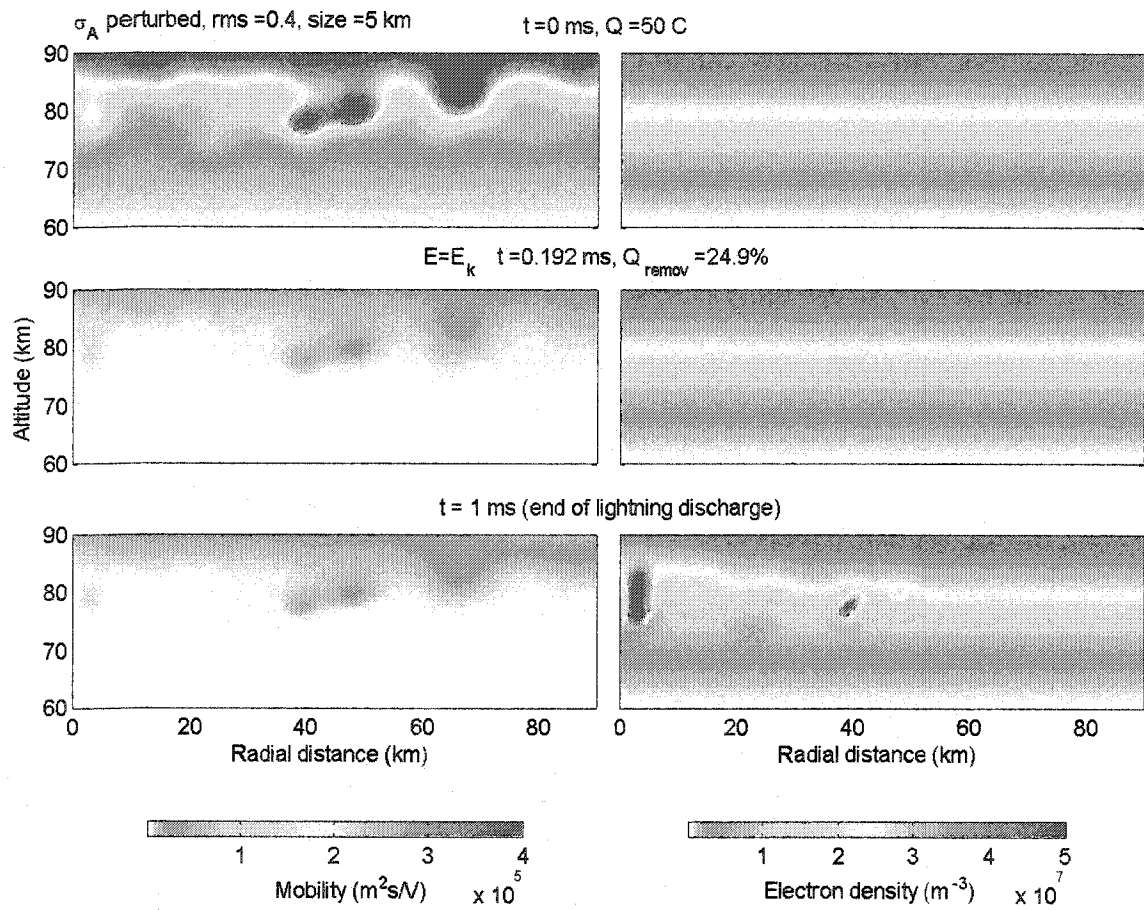
Figure A-10 Electron mobility (left) and electron density (right) for perturbed case 7. The first row shows t = 0 ms, the second row shows when $E_{tot} = E_k$ for the first time, and the third row shows t = 1 ms. The percentage of the total charge removed (Q_{remov}) and breakdown time are indicated above the middle row panel. Case 7 is the control case with input perturbations parameters A_{pert} = 0.4 and $size_{pert}$ = 5 km.
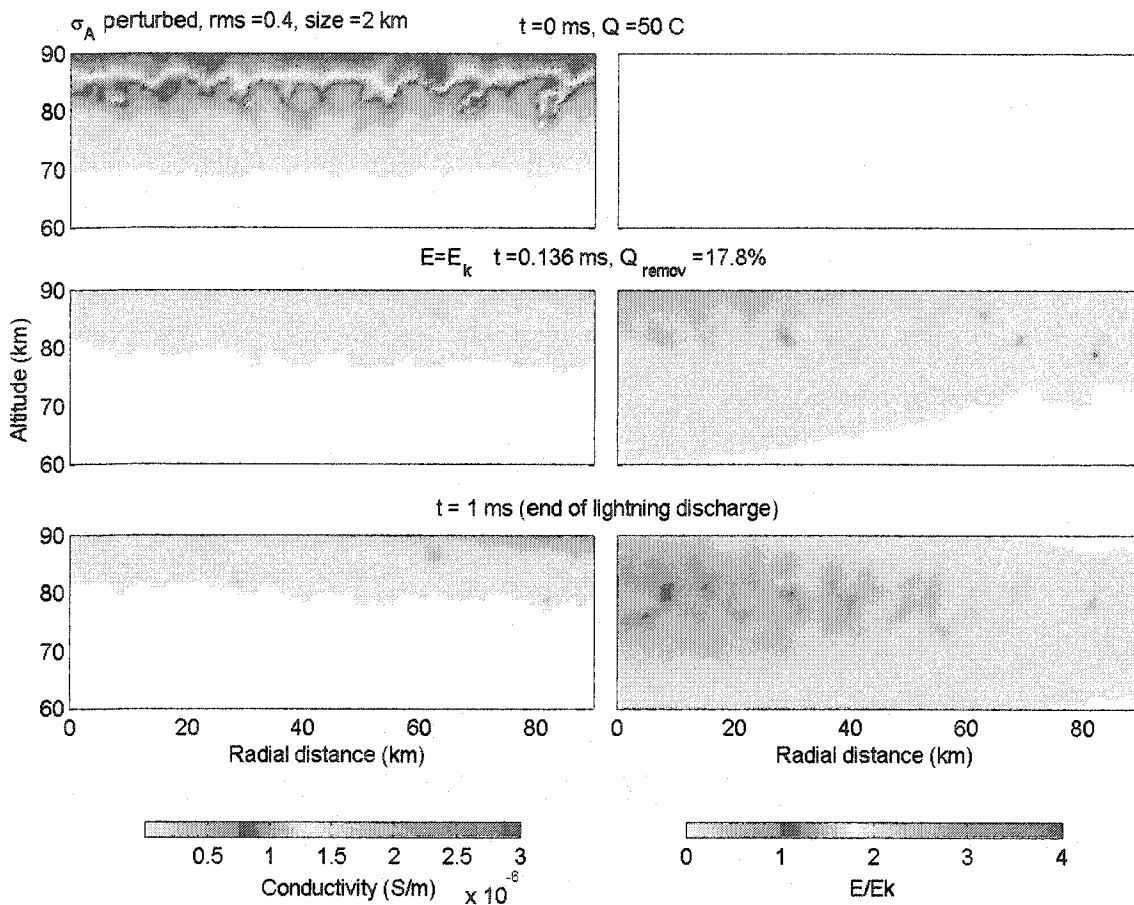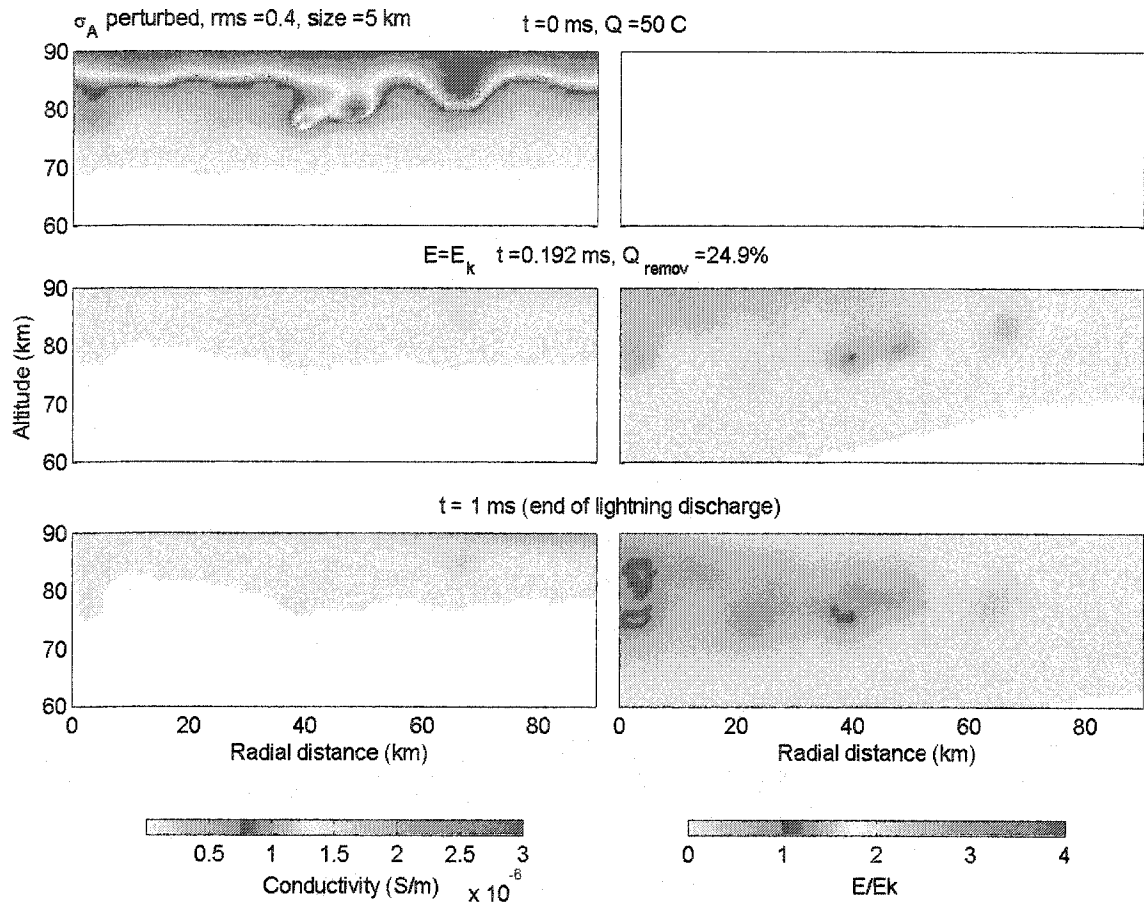
Figure A-11 Conductivity (left) and E_{tot}/E_k (right) for perturbed case 7. The first row shows $t = 0$ ms, the second row shows when $E_{tot} = E_k$ for the first time, and the third row shows $t = 1$ ms. The percentage of the total charge removed (Q_{remov}) and breakdown time are indicated above the middle row panel. Case 7 is the control case with input perturbations parameters $A_{pert} = 0.4$ and $size_{pert} = 5$ km.

APPENDIX B

PUBLICATIONS RELATED TO CHAPTERS 2 AND 3

Statistical analysis of space–time relationships between sprites and lightning

Fernanda T. São Sabbas[a,*], Davis D. Sentman[a], Eugene M. Wescott[a], Osmar Pinto Jr.[b], Odim Mendes Jr.[b], Michael J. Taylor[c]

[a]*Geophysical Institute, University of Alaska Fairbanks, 903, Koyukuk Drive, Fairbanks, AK 99775-7320, USA*
[b]*Instituto Nacional de Pesquisas Espaciais (INPE), São José dos Campos, SP 12240-340, Brazil*
[c]*Space Dynamics Laboratory, Utah State University Research Foundation, 1695 N. Research Parkway, North Logan, UT 83431-1947, USA*

Abstract

We present a detailed statistical analysis of the association of 40 sprite events with lightning from the parent thunderstorm. Both temporal and spatial criteria were used to identify the parent cloud-to-ground (CG) lightning. Sprite images were GPS time stamped and their locations triangulated. In contrast to previous reports of nearly one-to-one association of sprites with positive cloud-to-ground (+CG) lightning, 11 events (27%) did not have a +CG recorded by the National Lightning Detection Network (NLDN), and 7 events (17%) had neither NLDN nor very low frequency (VLF) signatures associated with them. A negative cloud-to-ground (−CG) preceded one of these events by 9 ms. As expected for ∼16.7 ms integrated images, none of the sprites without a +CG had any discernible visual characteristic that would distinguish them from "regular positive sprites". We have calculated the distribution of time intervals ($\Delta t = t_{sprite} - t_{lightning}$) for the sprites that had a parent +CG flash registered by the NLDN or VLF systems, and the distribution of distances between the sprite nadir positions and the flash locations registered by the NLDN. The time interval (Δt) distribution had a peak around 10–20 ms and a mean of 30 ms (total). This distribution is broadly consistent with the characteristic single electron avalanche time scale associated with streamer growth between ∼70 and 85 km. The distribution of the distances (Δs) between the nadir point of sprites and the parent +CGs showed that approximately two-thirds of the sprites occurred within 50 km lateral displacement from the parent +CG. The parent +CG peak current distribution had a maximum at 40–50 kA and mean of 60 kA, suggesting that high peak currents ($I \geqslant 75$ kA) are not a necessary prerequisite for sprites. The peak current distribution for all +CGs of the storm, with a maximum around 10–20 kA and mean of 27 kA, exhibits a qualitatively different form from the peak current distribution of the parent +CGs producing sprites.
© 2003 Elsevier Science Ltd. All rights reserved.

Keywords: Sprites; Lightning; Relationships; Triangulation; Statistics

1. Introduction

Sprites are luminous mesospheric/D region emissions generally associated with positive cloud-to-ground lightning (+CGs). Their duration can vary from a few ms to a few hundred ms. Sprites were initially reported to extend

from 40 to 90 km altitude and possess lateral dimensions of 5–30 km (Sentman et al., 1995). More recent observations have shown that some sprites appear to extend down to the top of the clouds (Siefring et al., 1999), and that their horizontal extent within the mesosphere ranges from ∼10 m, for the small column sprites and fine structure within sprites (Gerken et al., 2000), to ∼40 km for fully developed single sprites (Stenbaek-Nielsen et al., 2000), and a few hundred of km for sprite clusters. Sprites are predominantly red in color and the dominant emissions are found to be from the

* Corresponding author. Tel.: +1-907-474-7410; fax: +1-907-474-7290.
E-mail address: fsabbas@gi.alaska.edu (F.T. São Sabbas).

first positive bands of N_2 (Mende et al. 1995; Hampton et al. 1996; Heavner et al., 2000). Evidence for ionization has been reported in the form of weak red N_2^+ Meinel emissions (Bucsela et al., 1998; Morrill et al. 1998) and transient blue N_2^+ 1NG emissions (Armstrong et al. 1998; Suszcynsky et al., 1998; Takahashi et al., 1998; Armstrong et al., 2000).

Boccippio et al. (1995) first established that a +CG lightning precedes most sprites by approximately 20–30 ms. In their study, totals of 42 and 55 sprites observed in July 12 and September 7, 1994, respectively, were analyzed. Approximately 86% and 82% of the sprites each night, respectively, were preceded by a +CG recorded by the NLDN, and 95% and 78% were preceded by a Q-burst (large excitation of the normal modes of the Earth-ionosphere cavity in the extremely low frequency (ELF) Schumann resonance band), recorded by an ELF sensor. Subsequent studies have reported results that are generally consistent with these observations (Lyons, 1996; Cummer and Inan, 1997; Bell et al., 1998).

Based on observations showing evidence that sprites are strongly associated with positive cloud-to-ground lightning, several mechanisms have been proposed to explain the sprite generation process (Boccippio et al., 1995; Pasko et al. 1997; Bell et al., 1995; Roussel-Dupré and Gurevich, 1996; Taranenko and Roussel-Dupré, 1996). A widely accepted model (Pasko et al., 1997) uses a quasi-electrostatic approach in which a transient electric field generated by a +CG is the dominant trigger mechanism for sprites. Because of the higher altitude of the positive charge center inside the thunderstorm assumed in this model and the higher incidence of continuing current among +CGs when compared to other types of lightning, the charge moment of +CGs is on average greater than other types of flashes, making +CGs more effective at generating sprites than other types of lightning. However, the model does not rule out occasional –CGs and intracloud discharges (ICs) with a large enough charge moment to generate a breakdown electric field in the mesosphere and produce a sprite.

Using an extensive set of low-light TV data from the summer of 1996, São Sabbas (1999) analyzed 746 sprites from 7 different nights and found that only 65% of sprites were associated with +CG recorded by the NLDN, suggesting that other types of lightning besides +CGs could be generating sprites. About 11% of sprites were found to be immediately preceded by a –CG, and 24% of sprites were not associated with a CG registered by the NLDN. At the time this study was performed no association between sprites and –CG had been reported. In an independent study, Barrington-Leigh et al. (1999) subsequently reported observations of 2 sprites that had a –CG VLF signature associated with them. Those results support São Sabbas (1999) suggestion that +CGs are not the only type of lightning that can generate sprites.

In this paper, we report results of a detailed statistical study of the space–time association of sprites with positive

and negative CGs. In most previous studies of the association of sprites with lightning, sprites were assumed to be centered above the causative +CGs, which were identified based on timing proximity (Lyons, 1996; Cummer and Inan, 1997; Bell et al., 1998). Lyons (1996), using 7 events, and Wescott et al. (1998; 2001), using 20 events, have triangulated the location of sprites showing that they are actually laterally displaced from the +CGs on average ~50 km. In the present study we investigated the association of sprites with ±CGs preceding the sprites based on time and distance. We calculated the distribution of distances and time differences between the parent +CG and the sprite, and the peak current distribution of the sprite-associated +CGs. The results obtained here were compared with four previous observational studies. We also discuss a definition for an "independent sprite event" based on the time interval and distance between the sprite and the parent +CG, as well as considerations about the physical process involved in initiating a sprite.

2. Observations

We studied a set of 40 sprite events recorded on July 22, 1996, during the Sprites96 Campaign, conducted in the central United States. The location of cloud-to-ground lightning discharges of the sprite producing thunderstorm, recorded by the NLDN between 00:00 and 14:00 UT, are shown in Fig. 1 together with locations of CGs from other thunderstorms. Sprites were documented above the mesoscale convective storm (MCS) over Kansas.

The location of the sprites was triangulated, with an accuracy of a few to a few tens of km, from images simultaneously obtained by University of Alaska (UAF) and Utah State University (USU) located at different ground optical sites. Simultaneously recorded sprites were easily identified by comparing their time and visual characteristics in the images recorded by UAF and USU. The UAF observations were made from the Wyoming Infra-Red Observatory (WIRO, 41.098°N, 105.997°E, 2.943 km alt.), on Jelm Mountain, Wyoming, using an unfiltered intensified (~600–800 nm BW) CCD video camera with ~17° FOV operating at 30 frames/s (fps). A GPS clock was coupled to the camera system to provide time stamped images (TV fields) with a resolution of ~16.7 ms (1 field), and an absolute scan line accuracy of 1 μs. The GPS time stamped onto the image (t_{field}) corresponded to the very last scan line of each field, and was used as the sprite time (t_{sprite}).

The USU observations were obtained from Yucca Ridge Field Station (YRFS, 40.669°N, 104.939°E, 1.6 km alt.), located 20 km northeast of Ft. Collins, Colorado. Sprites were recorded at 25 frames/s (fps) using an Isocon camera with ~22° field-of-view (FOV). The camera was fitted with a 665 nm interference filter to image sprites in the N_2 first positive system, and each video field was uniquely time stamped using a crystal clock oscillator with a drift of
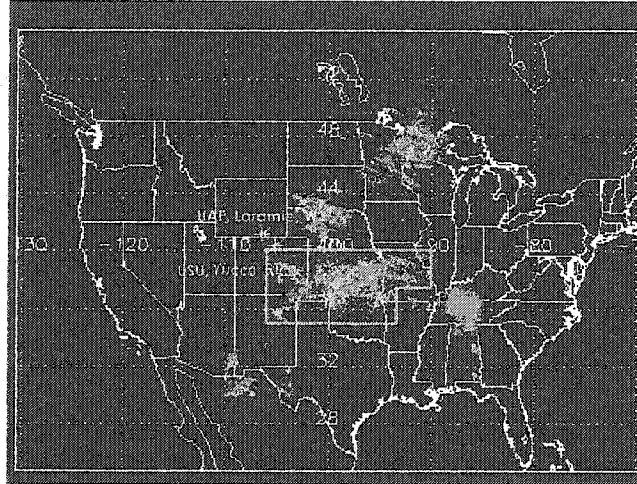
Fig. 1. Map of United States showing location of +CGs (red), −CGs (blue) and +CGs possibly associated with sprites (green), occurred between 0 and 14 UT, on July 22, 1996. The lightning from the sprite producing storm is within the green rectangular region. Yellow asterisks indicate the locations of the 2 ground observation sites.

~2 s/day assumed to be linear. The clock was set manually at the start of each night to an accuracy of better than 1 s (see Armstrong et al., 1998 for details).

The lightning information was provided by the NLDN (Cummins et al., 1998). Broadband electric field data (between ~200 Hz and ~200 kHz) recorded from the Langmuir Laboratory, New Mexico (Stanley et al., 2000), were examined to look for very low frequency (VLF) signatures (3–30 kHz) of CGs flashes in the cases for which NLDN did not record a lightning signature.

3. Results and discussion

3.1. Identification of sprite independent events

Initially, we visually identified 47 sprites recorded from both ground sites that could be triangulated. To be identified as an independent event, a sprite had to have occurred with a time separation of at least 1 video field (~16.7 ms) and be spatially distinct from any sprite occurring in the previous field. The spatial displacement requirement prevented counting a re-brightening or the continuity of previous processes as distinct events. Individual events could be single "sprite units" (Sentman et al., 1995) or what we defined as "sprite spatial groups", i.e., a group of units that occurred simultaneously, within a single video field (e.g. Figs. 9a and b).

This preliminary definition, based solely on video images, proved not to be completely unambiguous in the case of complex events when a single lightning discharge generates consecutive sprites. Hence, we constructed a statistic based on both the time interval between a sprite and its nearest preceding (parent) +CG and on triangulation. The parent CG candidates, positive or negative, were initially screened by requiring the CG to have occurred in a space–time vicinity of the sprite defined as a square region of 400 km on a side, centered on the sprite, and within a 1 s window preceding the sprite. Cloud-to-ground lightning registered by NLDN, occurring closest in time preceding the sprite and closest in space were selected as being the parent CG. For CGs with a VLF signature and no NLDN signature, only the time criterion was applied. Negative CGs were selected only if neither the NLDN nor the Broad band electric field sensor recorded a positive CG. To calculate the time interval between sprites and parent +CGs ($\Delta t = t_{sprite} - t_{lightning}$) the GPS time tag of the video field (t_{field}) in which the sprite first appeared was used as t_{sprite} (Fig. 2).

In the video systems used in this study the time stamp on each image field refers to the end of the video field. Each video field has a duration of ~16.7 ms, so the start of the image is at $t_{field} - 16.7$ ms and the end is at t_{field} ($= t_{sprite}$ when a sprite is present). Hence, the sprite could have occurred at any instant in the interval $t_{sprite} - 16.7$ ms to t_{sprite}, and 16.7 ms is the maximum uncertainty in the sprite time. In the cases when the parent lightning occurs within the interval of the video field containing the sprite, Δt may be less than 16.7 ms, since causality requires the sprite to have occurred some time after the lightning but before the end of the video field. The sprite must be constrained to this interval. When $\Delta t < 16.7$ ms, the uncertainty in the sprite time is equal to Δt.
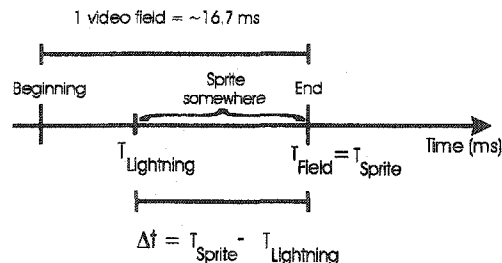
1 video field = ~16.7 ms

Fig. 2. Diagram showing how Δt can be < 16.7 ms. The lightning occurs before the sprite and the GPS time stamped at the end of the field is assigned as t_{sprite}. Due to causality the sprite must have occurred some time after the lightning but before the end of the video field.
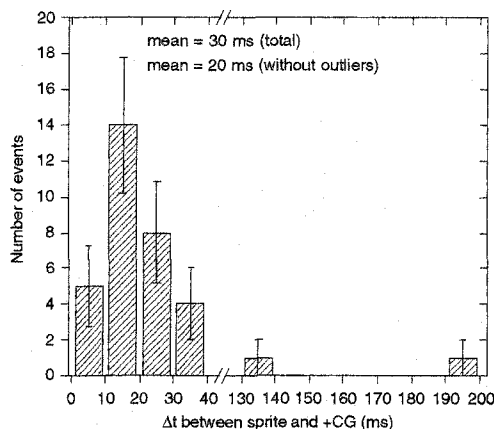

Fig. 3. Distribution of the time difference between the sprite and parent +CG flashes within the sprite's space-time vicinity, binned in intervals of 10 ms. The error bars are the statistical errors, i.e. the square root of the number of events in each bin.

Fig. 3 shows the distribution of time intervals between sprites and parent +CGs. The first bin $(0 \leqslant \Delta t < 10$ ms) and part of the second bin $(10 \leqslant \Delta t < 20$ ms) represent the cases in which the parent lightning occurs within the interval of the video field containing the sprite, discussed in the previous paragraph. The time-interval distribution peaks around 10–20 ms and possesses a mean value of 30 ms (20 ms if we exclude the 2 outlying events). This distribution agrees with results reported by Bell et al. (1998).

Bell et al. (1998) suggested that the longest delays observed in their study were associated with small sprites for which horizontal intracloud discharges removed the amount of charge necessary to generate them. Furthermore, Δt would vary from 0 to 15 ms for the larger events to 100 ms to the smallest events. We grouped the sprites analyzed here in three categories with respect to visual size

and brightness: small, medium and large. The three groups were statistically consistent with each other (graph not shown). We did not observe any consistent visual distinction between sprites with short and long Δt: in fact, the two events with largest Δt (outliers) were very bright (large) sprites. We suggest that the time delay between lightning and sprites characterizes the time scale of the duration of the physical process (or processes) that is responsible for the sprite initiation, and takes place once the transient electric field is established in the mesosphere. This process is discussed in recent models based on streamer physics (Pasko et al., 1998; Raizer et al., 1998) that explain in detail how the fine structure observed in high-speed (Stanley et al., 1999; Stenbaek-Nielsen et al., 2000) and telescopic (Gerken et al., 2000) images of sprites develop.

The process that originates a streamer can be triggered from an avalanche initiated by a single electron. The avalanche creates a local charge separation, and the streamer develops when the electric field of the space charge equals the external transient electric field in the mesosphere generated by the CG. Pasko et al. (1998) have modeled the characteristic time of this process as $t_z = z_s/v_d$, where $z_s = (1/\alpha)\ln(4\pi\varepsilon_0 r_s^2 E_k/e)$ is the distance over which the avalanche generates a space charge field comparable to the ambient electric field, taken to be the breakdown field $\sim E_k$. Here, $\alpha = (v_i - v_a)/v_d$, where v_i is the ionization rate, v_a is the electron attachment rate, v_d is the electron drift speed, and the space charge is assumed to be concentrated in a sphere of radius $\sim r_s$. Fig. 1 of Pasko et al. (1998) shows the altitude profile of the modeled t_z. The distribution of Δt between the sprite and parent +CG shown in Fig. 3 is consistent with the characteristic time scale for the development of an individual electron avalanche into a streamer between ~ 70 and 85 km altitude modeled by Pasko et al. (1998).

Fig. 4 shows the distribution of distances (Δs) between the triangulated nadir point (latitude and longitude) of sprite events and the location of parent +CGs. The distances between sprite events and parent +CGs were calculated for the +CGs detected by the NLDN only. When the sprite events were "spatial groups" an average nadir point was calculated using the triangulated nadir points of each "sprite unit". The distribution displayed in Fig. 4 shows that approximately two thirds of sprites occurred within 50 km from the parent +CG, in agreement with Lyons (1996) and Wescott et al. (1998). The maximum distance observed was ~ 82 km. Since "spider" discharges extending for ~ 100 km have been previously observed (Lyons, 1996), all +CGs in the present study were consistent with previous results, and no further spatial selection criteria were applied to identify independent events.

We also plotted the time intervals versus the distance (Fig. 5) and there was no correlation between the two quantities, i.e. sprites further away from the +CG do not appear to have longer delays.

Most sprites ($\sim 95 \pm 15\%$) that were associated with +CGs occurred within 40 ms after the parent +CG. Only
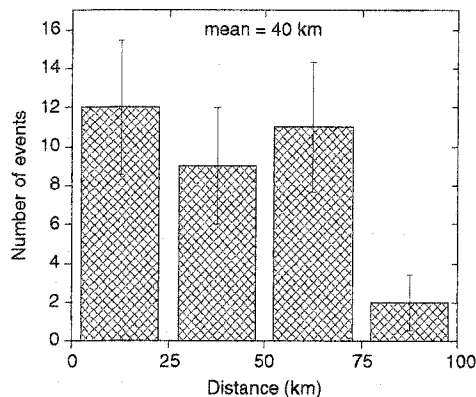
Fig. 4. Distribution of the distances between sprites events and parent +CG flashes within the sprite's space–time vicinity. The events were binned in intervals of 25 km, and the "error bars" are the statistical errors.
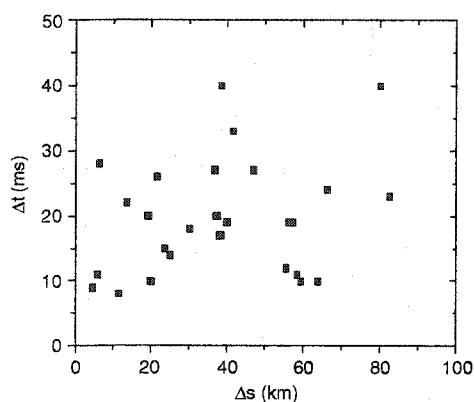

Fig. 5. Time interval between sprites and associated +CGs versus the distance between them. The two outliers, one with $\Delta t = 140$ ms and $\Delta s = 51$ km, and the other with $\Delta t = 197$ ms and $\Delta s = 75$ km, are not shown.

two events occurred with a Δt greater than 40 ms after the +CG. Given the large time interval that those sprites had from their parent +CG (140 and 197 ms) it is possible that closer +CGs had occurred but were not registered by either NLDN or the Broadband electric field sensor.

Except for the two outlying events, the analysis of Fig. 3 suggests 40 ms as an effective upper limit for the delay between the parent +CG flash and the sprites observed during this night. The 40 ms delay exceeds the timing uncertainty of $\sim$16.7 ms by a factor of $\sim$2.5, and is therefore a robust result. Based on this result, consecutive sprites that had a minimum time separation of $\sim$16.7 ms from each other and

a maximum time interval of 40 ms from the parent CG were grouped into a "sprite time group", similar to the manner in which individual strokes are grouped into flashes (Cummins et al., 1998). The individual "sprite units" or "sprite spatial groups" were called "sprite time units". Seven sprites that did not have a +CG registered by any system, and which had been initially considered to be independent events were reclassified to be "time units" forming a single "time group" event. The hypothesis used here is that if the electron avalanche can take up to 40 ms to develop into a streamer in a particular location, multiple "sprite time units" could be produced by the same CG at different locations, with a varying duration for the streamer development, probably influenced by the local characteristics, within a maximum Δt of 40 ms from the CG. The total number of sprite events was thereby reduced from 47 to 40, 7 events being "time groups" with 2 "time units" each.

The definition of what an independent sprite event might be has been extensively but informally discussed within the sprite community; the topic has not yet been approached in scientific papers. There is no established definition of "independent sprite event." This is an important issue since any analysis of the temporal and spatial relationship between sprites and lightning based on observational data is affected by how and if sprites are grouped into "independent events", i.e., by the definition used. For the sprites occurring on July 22, 1996, analyzed in this paper, the maximum Δt observed, excluding the 2 outliers, was 40 ms. However this could be a particularity of this specific night, resulting from a combination of the characteristics of the thunderstorm, lightning activity and local mesospheric conditions. For example, applying the same selection criteria for parent +CGs (closest in time preceding the sprite and closest in space), a preliminary analysis of 69 triangulated sprites from July 24, 1996, resulted in only 58 ± 9% sprites occurring within 40 ms after the parent +CG (not shown). That illustrates the necessity of a detailed statistical study of a large data set of triangulated sprites with GPS timing from a variety of storms and locations to establish a definition of "independent sprite event" with bounded variances that can be widely adopted. Such a study is been currently developed as a continuation of the analysis reported herein.

3.2. Sprites' association with lightning and comparison with other studies

Working with the redefined data set of 40 sprite events, we found that about 73 ± 13% of the sprites were associated with a +CG recorded by the NLDN. This percentage increased to 82 ± 14% when we considered VLF signatures for +CGs not detected by the NLDN. NLDN has detection efficiency around 90% for −CGs (Cummins et al., 1998). The detection efficiency of +CGs has not been documented, but may be assumed to be similar to this. The 10% increase in the number of sprites associated with +CGs when VLF data is considered supports this assumption.

Table 1
Comparison of reports of the percentage of sprites associated with +CGs

Study	Dates	Report	Total number of sprites	Percentage of sprites with +CGs detected by the NLDN (%)
1	July 12, 1994	Boccippio et al. (1995)	42	86 ± 14
2	September 7, 1994	Boccippio et al. (1995)	55	82 ± 12
3	August 6, 1994	Lyons (1996)	36	94 ± 16
4	July 6, 7, 11, 19, 21, 22, 24, 1996	São Sabbas (1999)	746	65 ± 3
5	July 22, 1996	This study	40	73 ± 13

We have compared the percentage of sprites associated with lightning calculated in this work with values reported by Boccippio et al. (1995), Lyons (1996) and São Sabbas (1999). Boccippio et al. (1995) compared the time of occurrence of sprites, recorded in GPS time-stamped low-light-level video images, with the time of lightning discharges from the associated thunderstorms recorded by the National Lightning Detection Network (NLDN), as well as with electromagnetic "Q-bursts" events. The ELF data was time-tagged with an internal PC clock that drifted ~13 s/day. The drift was assumed to be linear. An algorithm generated by comparing the recorded onset times with the GPS-timed sprite events corrected the drift. The sprites occurred above thunderstorms over the central US and were observed from Yucca Ridge. The identification of the parent +CGs of the sprites was based mainly on timing. Sprite locations were not triangulated, and the spatial requirement was that NLDN and/or ELF signatures must have originated from the same thunderstorm that generated the sprites.

Lyons (1996) studied 36 sprites recorded in GPS time stamped images from Yucca Ridge, during a 2 h interval. The sprites occurred above a mesoscale convective system (MCS) over Nebraska on August 6, 1994. Lyons (1996) reported that 94% of sprites were preceded by +CGs registered by the NLDN. Seven sprites were triangulated and the location of the other sprites was estimated based on the location of the parent +CG, which was identified based on the timing.

São Sabbas (1999) analyzed 746 sprites from 7 different nights in 1996, recorded from Yucca Ridge by Utah State University. The sprites occurred above thunderstorms over the central US on July 6, 7, 11, 19, 21, 22 and 24, 1996, and were image using the same system describe in the Section 2. To compensate for the time uncertainty of this system, a selection window with Δt of 360 ms before the sprite and 60 ms (3 fields at 25 fps) afterwards was adopted in identifying the parent +CG. Sprites were not triangulated in this study, so to be considered a possible parent the +CG had to be inside the field of view of the camera. With this approach several +CGs that were not associated with sprites may have been incorrectly tagged as the possible parents of sprites. Nevertheless, only 65 ± 3% of the sprites were
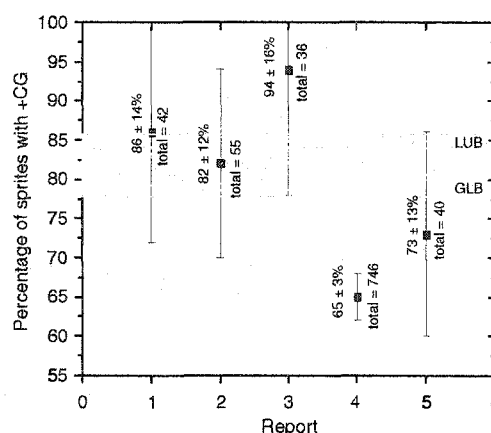

Fig. 6. Comparison between various statistical studies of percentages of sprites associated with +CGs detected by the NLDN. The region between the least upper bound (LUB) and the greatest lower bound (GLB) is highlighted.

associated with a +CG signature registered by the NLDN. The same criteria were used to look for a possible association of sprites with −CGs when there was no +CG. Table 1 summarizes these results.

The definitions of "sprite independent event" utilized for studies 1–3 were not available, in study 4 all "sprite time units" were considered to be "independent events." The statistical uncertainties ("error bars") of these percentages were estimated using $\Delta x = x/(N\sqrt{x})$, where x is the number of events relative to the percentage (x/N) and N is the total number of events, and are included in Table 1. These results, including the estimated uncertainties, are plotted in Fig. 6. The figure also shows the least upper bound (LUB) and the greatest lower bound (GLB) of the uncertainties for studies 1, 2, 3 and 5. When these uncertainties are taken into account, studies 1, 2, 3 and 5 are statistically consistent among themselves within the region bounded by the LUB and GLB. Report number 4, however, is statistically distinct from the other reports, since its error bars do not fall

7

Table 2
Lightning and sprite related data (São Sabbas, 1999)

July, 1996	Percentage of +CGs relative to total	Percentage of −CGs relative to total	Total number of CGs	Number of sprites	Duration of sprite period
6	10.9% (2652)	89.1% (21740)	24392	36	2 h 34 m
7	14.1% (1367)	85.9% (8318)	9685	88	4 h 22 m
11	10.7% (1928)	89.3% (16129)	18057	38	1 h 32 m
19	7.3% (1086)	92.7% (13714)	14800	83	3 h 05 m
21	17.0% (1504)	83.0% (7327)	8831	212	3 h 27 m
22	10.9% (4412)	89.1% (36193)	40605	84	4 h 07 m
24	9.0% (5088)	89.0% (51446)	56534	205	5 h 20 m

within their LUB and GLB. The low percentage (65 ± 3%) of sprites associated with +CGs was obtained using a large time selection window, and a data set on average 17 times larger than the data sets utilized in the other studies. Even adjusting upwards by 10%, to approximately compensate for the 90% detection efficiency of NLDN, 25 ± 2% of sprites remain without +CGs. São Sabbas (1999) suggested that −CGs and intracloud discharges were generating the sprites without +CGs that could not be explained by NLDN detection efficiency.

Table 2 shows the percentage of positive and negative lightning relative to the total lightning (positive + negative) for the sprite producing thunderstorm of July 22, 1996 analyzed here, together with percentages for other nights analyzed by São Sabbas (1999). The table also shows the number of sprites observed and duration of the sprite production period for comparison. All storms had small percentages of +CGs (from 7.3% to 10.9%), showing that the production of a large percentage of +CGs by the thunderstorm is neither a necessary condition for sprite occurrence nor a determining factor for the number of sprites produced.

Fig. 7 shows a relationship between the onset of sprite production and growth in the rate of occurrence of the storm's +CG for all peak current ranges. Of the seven days in 1996 studied by São Sabbas (1999), July 21, 1996, is the only day for which the onset of the sprite occurrence might have been observed, since the observations for this day started before lightning activity. In all other days, lightning activity had already commenced before observations began. On July 21, 1996, sprites were observed to commence after a continuous growth in the occurrence rate of storm's +CGs, for all peak currents ranges. All other days had similar growths and peaks in the +CG occurrence rate of storm's +CG before the beginning of the observation period (not shown).

3.3. Negative sprites and sprites without a CG

Approximately 27 ± 8% of sprites did not have a parent +CG recorded by the NLDN, and 17 ± 7% had neither NLDN nor VLF signatures. Two of the seven sprite events
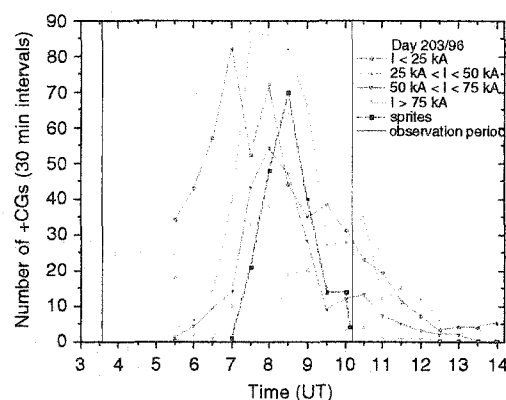

Fig. 7. Time distribution of the number of positive lightning in 30-min intervals, for different peak current ranges, day 203/96 (São Sabbas, 1999). The vertical black line delimitate the observation period. Sprites started to occur at 6:40 UT.

that had neither a NLDN nor VLF +CG signature were preceded by a −CG (Figs. 8a and 9a). Fig. 8 shows three consecutive independent sprite events. The time separation between the first and second event is 50 ms, and between the second and third is 117 ms. The first event (Fig. 8a) was preceded by a negative CG with $\Delta t = 9$ ms. This flash was not registered by the NLDN, but it was registered by the New Mexico Tech VLF system. Due to its small Δt it is very likely that this −CG, in fact, generated the sprite. The second sprite (Fig. 8b), considered as an independent event here (occurred 59 ms from the −CG associated with the first sprite), was not associated with any detected CG, positive or negative.

The third event (Fig. 8c) had both NLDN and VLF +CG signatures preceding it by 17 ms. The +CG had a peak current of 48 kA and occurred ~78 km from the sprite. The discharge had a slow tail in VLF that lasted ~0.5 ms. It was followed, ~4 ms afterwards, by a slow energetic field change, possibly due to the sprite, that lasted ~1 ms (not shown). The "positive sprite" (Fig. 8c) was the brightest of

8   F.T. São Sabbas et al. / Journal of Atmospheric and Solar-Terrestrial Physics ███ (████) ███–███
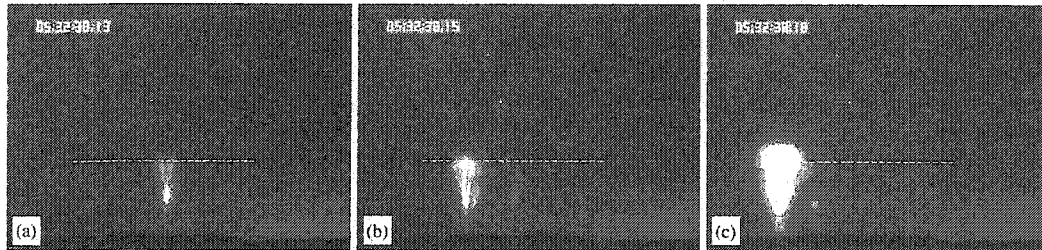

Fig. 8. Three consecutive independent sprite events separated by 50 (a and b) and 117 ms (b and c), respectively. The first sprite (a) was preceded by a $-$CG recorded by the Broad band electric field sensor (no NLDN), $\Delta t = 9$ ms. The second sprite (b) had no CG signature associated with it in either NLDN or VLF, and the third (c) was preceded by 48 kA $+$CG recorded by both systems, $\Delta t = 17$ ms and $\Delta s = 78$ km. The images shown were obtained by UAF.
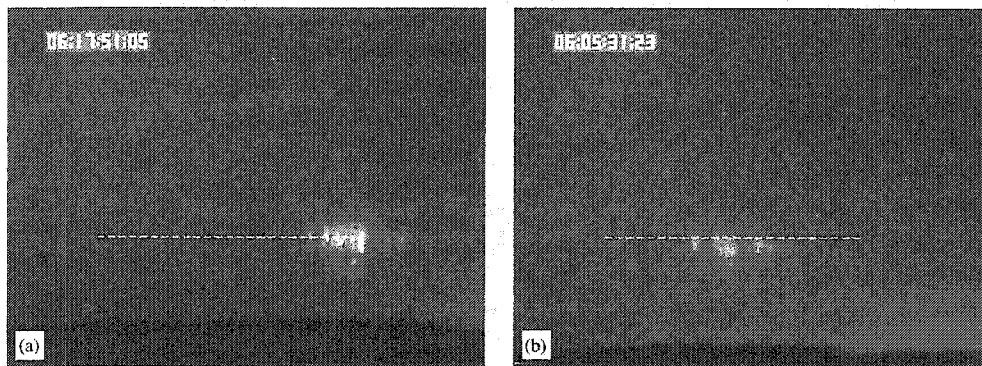

Fig. 9. The first image (a) shows a sprite preceded by a 22 kA $-$ CG recorded by both NLDN and VLF systems, $\Delta t = 146$ ms and $\Delta s = 201$ ms. The second (b) shows a similar type of sprite event that was preceded by a 47 kA $+$CG, $\Delta t = 28$ ms and $\Delta s = 9$ km. The images shown were obtained by UAF.

these three consecutive events, but there were other "positive sprites" that occurred during the night of the study that were much smaller and dimmer than the possible "negative event" (a) displayed in Fig. 8a. The variation of brightness of the sprites with respect to underlying lightning characteristics is not yet well understood.

The second sprite preceded by a $-$CG detected in this study is shown in Fig. 9a, together with a "positive sprite" (Fig. 9b) for comparison of visual characteristics. The $-$CG was recorded by the NLDN and VLF system 146 ms before the sprite, had a peak current of 22 kA and occurred at $\sim$201 km from the event. Because of the large Δt and distance between this sprite and the $-$CG, it is possible that both NLDN and VLF systems missed a $+$CG (or $-$CG) that would have a better association with this event. The "units" of this sprite, shown in Fig. 9a, were slightly brighter and larger than the "units" of the "positive sprite" of Fig. 9b. The sprite in Fig. 9b was preceded by a $+$CG with a Δt equal to 28 ms. The $+$CG peak current was 47 kA and it occurred $\sim$9 km from the sprite.

None of the sprites without $+$CGs had any particular characteristics that would visually distinguish them from the positive sprites. An upward–downward difference in the branch orientation might conceivably be expected for sprites generated by lightning of different polarities. However, we do not expect this difference to appear in a 16.7 ms integration image; it is more likely to show on 1 ms images from high-speed cameras (e.g., Stanley et al., 1999; Stenbaek-Nielsen et al., 2000). Comparatively, the percentage of "bright" and "small" events was about the same for positive and negative sprites.

There are two possible interpretations for the sprites without a $+$CG. The first is that they were preceded by positive strokes undetected by either the NLDN or the VLF systems. An alternate interpretation is that other types of lightning besides $+$CGs, e.g., negative CGs and intracloud discharges, may also generate sprites. This interpretation is supported by the São Sabbas (1999) study, and is not ruled out by Pasko et al. (1997) quasi-electrostatic model, or the Pasko et al. (1998) and Raizer et al. (1998) streamer models. Sprites
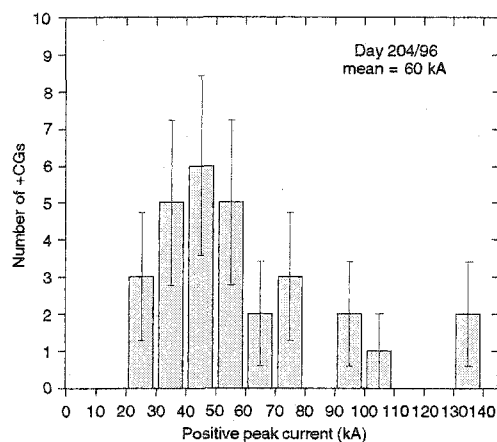
Fig. 10. Peak current distribution of the parent +CG flashes within the sprite's space–time vicinity. The +CGs are binned in intervals of 10 kA. Error bars are the statistical errors.

generated by other types of lightning besides +CGs would represent a smaller portion of the total, such as we may have observed here. Furthermore, according to Dejnakarintra and Park (1974), and Baginski et al. (1988), vertical intracloud discharges that annihilate positive charge at the top of the clouds and negative charges at the bottom can both generate large electric fields in the upper atmosphere, also supporting this interpretation.

3.4. Peak current distribution of parent +CGs

Fig. 10 shows the peak current distribution of the sprite's associated +CG. The distribution exhibits a maximum for peak current between 40 and 50 kA. Five out of the 29 (17 ± 7%) +CG flashes preceding sprites had high peak

currents (> 75 kA). The average peak current of 60 kA in the present study agrees with the 52 kA reported by Boil et al. (1998), and supports results showing that the peak currents of +CGs producing sprites span a large range of values.

Fig. 11a shows that the peak current distribution of sprite's associated +CGs in the 7 storms studied in São Sabbas (1999) also has a maximum around 40–50 kA, and is statistically consistent with the one reported here (Fig. 10). Both distributions are different from the distribution for all +CGs in the 7 storms (Fig. 11b), which peaked at 10–20 kA and had a mean value of 27 kA. This difference in distributions is one of the principal characteristics that appear to distinguish the lightning population associated with sprites from those not associated with sprites. The peak current distribution of the −CG candidates found in the São Sabbas (1999) study and the totality of −CGs of the storm are quite similar to each other; both are centered at 10–20 kA (not shown).

4. Conclusions

We performed a detailed statistical analysis of the space–time relationships between sprites and the associated lightning characteristics. The results of this study can be summarized as follows:

1. A set of 40 sprite events from the Sprites96 campaign was analyzed. Seven of the events (17%) did not have a parent +CG registered by either NLDN or VLF sensors. Images of these events revealed no particular visual characteristics that distinguished them from positive sprites, and such differences are not expected at 16.7 ms integration. Two of the sprites without +CGs were preceded by a −CG, one of them was very likely to be associated with the −CG, which was registered by the VLF system 9 ms before the sprite.
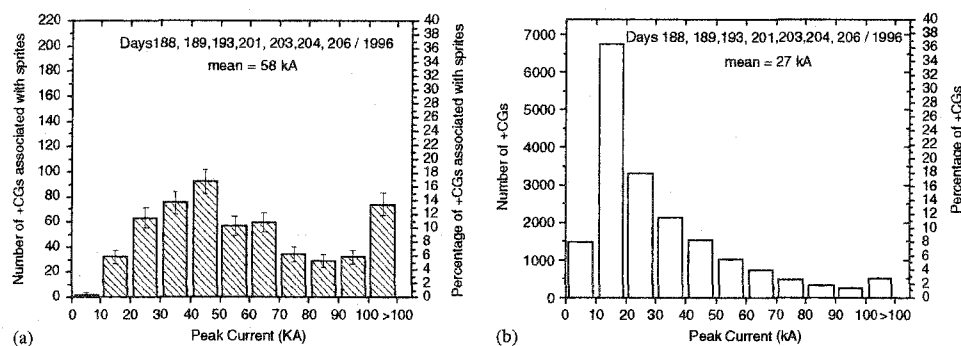

Fig. 11. Percentage distribution of the peak current of +CG associated with sprites (a), and (b) of the totality of +CGs of the storm (São Sabbas 1999). The last column, in both figures, is the percentage of all +CGs with peak current greater than 100 kA.

2. No correlation between the apparent visual size and brightness of sprites, and time delays from the associated +CGs was found. No correlation was found between with the size or brightness of sprites and the time interval or distance from their parent lightning, i.e. smaller/dimmer sprites or sprites further away from the associated +CG did not have longer time delays from the parent +CG then the bulk of the sprite population.

3. The distribution of time intervals between sprites and parent +CGs showed a peak between 10 and 20 ms with a mean of 30 ms (20 ms excluding the outliers). We suggest that this distribution characterizes the time scale for the development of an individual electron avalanche into a streamer between ~70 and 85 km altitude, as given in the Pasko et al. (1998) model. Most sprites occurred within 40 ms from the parent +CGs, suggesting this time interval as upper limit for the characteristic time delay between the +CG flash and the sprites observed during this night.

4. The distribution of the distance between sprites and parent +CGs showed that sprites have the tendency to occur within 50 km lateral displacement from the CG, consistent with results previously reported by Wescott et al. (1998) and Lyons (1996).

5. The peak current distribution of +CGs associated with sprites exhibited a larger mean and standard deviation than the distribution of all positives in the storm. It had a maximum between 40 and 50 kA and a mean of 58 kA, compared to a 10–20 kA maximum and 27 kA mean of the distribution for all positives.

The present work is the first statistical study to use both GPS timing for images and triangulated positions of sprites, where both temporal and spatial criteria are used to select the parent +CG. Additional statistical studies utilizing large data sets (>100 sprites) over numerous storms distributed globally are necessary to arrive at a tightly parameterized definition of "sprite independent event".

References

Armstrong, R.A., Shorter, J.A., Taylor, M.J., Suszcynsky, D.M., Lyons, W.A., Jeong, L.S., 1998. Photometric measurements in the SPRITES '95 & '96 campaigns of nitrogen second positive (399.8 nm) and first negative (427.8 nm) emissions. J. Atmos. Terr. Phys. 60, 787.

Armstrong, R.A., Suszcynsky, D.M., Lyons, W.A., Nelson, T.E., 2000. Multi-color photometric measurements of ionization and energies in sprites. Geophys. Res. Lett. 27, 653–656.

Baginski, M.E., Hale, L.C., Olivero, J.J., 1988. Lightning-related fields in the ionosphere. Geophys. Res. Lett. 15, 764–767.

Barrington-Leigh, C.P., Inan, U.S., Stanley, M., Cummer, S., 1999. Sprite directly triggered by negative lightning. Geophys. Res. Lett. 26, 683–686.

Bell, T.F., Pasko, V.P., Inan, U.S., 1995. Runaway electrons as a source of red sprites in the mesosphere. Geophys. Res. Lett. 22, 2127.

Bell, T.F., Reising, S.C., Inan, U.S., 1998. Intense continuing currents following positive cloud-to-ground lightning associated with red sprites. Geophys. Res. Lett. 25, 1285.

Boccippio, D., Williams, E., Heckman, S., Lyons, W., Baker, I., Boldi, R., 1995. Sprites, ELF transients, and positive ground strokes. Science 269, 1088.

Bucsela, E., Morrill, J., Siefring, C., Heavner, M., Moudry, D., Sentman, D., Wescott, E., Osborne, D., Benesch, W., 1998. Estimating electron energies in sprites from 1NG/2PG intensity ratios. EOS Trans. Am. Geophys. Union 81 (Fall Meeting Suppl., Abstract A42-D04), F175.

Cummer, S.A., Inan, U.S., 1997. Measurement of charge transfer in sprite-producing lightning using ELF radio atmospherics. Geophys. Res. Lett. 24, 1731.

Cummins, K.L., Murphy, M.J., Bardo, E.A., Hiscox, W.L., Pyle, R.B., Pifer, A.E., 1998. A combined TOA/MDF technology upgrade of U.S. National Lightning Detection Network. J. Geophys. Res. 103, 9035.

Dejnakarintra, M., Park, C.G., 1974. Lightning-induced electric fields in the ionosphere. J. Geophys. Res. 79, 1903.

Gerken, E.A., Inan, U.S., Barrington-Leigh, C.P., 2000. Telescopic imaging of sprites. Geophys. Res. Lett. 27.

Hampton, D.L., Heavner, M.J., Wescott, E.M., Sentman, D.D., 1996. Optical spectral characteristics of sprites. Geophys. Res. Lett. 23, 89–92.

Heavner, M.J., Sentman, D.D., Moudry, D.R., Wescott, E.M., Siefring, C.L., Morrill, J.S., Bucsela, E.J., 2000. Sprites, blue jets, and elves: optical evidence of energy transport across the stratopause. In: Siskind, D. (Ed.), Atmospheric Science Across the Stratopause. American Geophysical Union, Washington, DC.

Lyons, W.A., 1996. Sprite observations above the U.S. High Plains in relation to their parent thunderstorm systems. J. Geophys. Res. 101, 29641.

Mende, S.B., Rairden, R.L., Swenson, G.R., Lyons, W.A., 1995. Sprite spectra: N2 1 PG band identification. Geophys. Res. Lett. 22, 2633.

Morrill, J.S., Bucsela, E.J., Pasko, V.P., Berg, S.L., Heavner, M.J., Moudry, D.R., Benesch, W.M., Wescott, E.M., Sentman, D.D., 1998. Time resolve N2 triplet state vibrational populations and emissions associated with red sprites. J. Atmos. Solar-Terr. Phys. 60, 811–830.

Pasko, V.P., Inan, U.S., Bell, T.F., Taranenko, Y.N., 1997. Sprites produced by quasi-electrostatic heating and ionization in the lower ionosphere. J. Geophys. Res. 102, 4529.

Pasko, V.P., Inan, U.S., Bell, T.F., 1998. Spatial structure of sprites. Geophys. Res. Lett. 25, 2123–2126.

Raizer, Yu.P., Milikh, G.M., Shneider, M.N., Novakovski, S.V., 1998. Long streamers in the upper atmosphere above a thundercloud. J. Phys. D 31, 3255–3264.

Roussel-Dupré, R., Gurevich, A., 1996. On runaway breakdown and upward propagating discharges. J. Geophys. Res. 101, 2297–2311.

São Sabbas, F.T., 1999. Estudo da relação entre Sprites e os relâmpagos das tempestades associadas (Study of the relationship between Sprites and lightning from the associated storms). Master dissertation, Instituto Nacional de Pesquisas Espaciais (INPE), São José dos Campos, SP, Brazil, February 1999.

Sentman, D.D., Wescott, E.M., Osborne, D.L., Hampton, D.L., Heavner, M.J., 1995. Preliminary results from the Sprites94 aircraft campaign: 1. Red sprites. Geophys. Res. Lett. 22, 1205.

Siefring, C.L., Morrill, J.S., Sentman, D.D., Moudry, D.R., Wescott, E.M., Heavner, M.J., Osborne, D.L., Bucsela, E.J., 1999. Do sprites sometimes connect to the cloud tops? EOS Trans. AGU 8D (46), F225.

Stanley, M., Krehbiel, P., Brook, M., Moore, C., Rison, W., Abrahams, B., 1999. High speed video of initial sprite development. Geophys. Res. Lett. 26, 3201–3204.

Stanley, M., Brook, M., Krehbiel, P., Cummer, S.A., 2000. Detection of daytime sprites via a unique sprite ELF signature. Geophys. Res. Lett. 27, 871.

Stenbaek-Nielsen, H.C., Moudry, D.R., Wescott, E.M., Sentman, D.D., São Sabbas, F.T., 2000. Sprites and possible mesospheric effects. Geophys. Res. Lett. 27, 3829.

Suszcynsky, D.M., Roussel-Dupré, R.A., Lyons, W.A., Armstrong, R.A., 1998. Blue light imagery and photometry of sprites. J. Atmos. Solar-Terr. Phys. 60, 801.

Taranenko, Y., Roussel-Dupré, R., 1996. High altitude discharges and gamma-ray flashes: a manifestation of runaway air breakdown. Geophys. Res. Lett. 23, 571.

Takahashi, U., Watanabe, Y., Uchida, A., Sera, M., Sato, M., Fukunishi, H., 1998. Energy distributions of electrons exciting sprites and elves inferred from the Fast Array Photometer observations. EOS Trans. Am. Geophys. Union 79, F175.

Wescott, E.M., Sentman, D.D., Heavner, M.J., Hampton, D.L., Lyons, W.A., Nelson, T., 1998. Observations of "Columniform" sprites. J. Atmos. Solar-Terr. Phys. 60, 733–740.

Wescott, E.M., Stenbaek-Nielsen, H.C., Sentman, D.D., Heavner, M.J., São Sabbas, F.T., 2001. Triangulation of sprites, associated halos and their possible relation to causative lightning and micro-meteors. J. Geophys. Res. 106 (A6), 10467–10477.

Dynamical relationship of infrared cloudtop temperatures with occurrence rates of cloud-to-ground lightning and sprites

F. T. São Sabbas and D. D. Sentman

Geophysical Institute, University of Alaska, Fairbanks, Alaska, USA

[1] We correlated cloudtop temperatures obtained from GOES-8 infrared images, lightning data from the National Lightning Detection Network, and triangulated nadir positions of sprites from a 22 July 1996 Mesoscale Convective System (MCS) over Kansas. The maximum sprite production of the MCS occurred during the transition between growth and decay phases of the system, and when the occurrence rate of negative cloud-to-ground (−CG) flash activity maximized. The −CG flash rate was maximum when the overlying cloudtop temperatures T_c were minimum, −69° to −72°C. During the MCS growth phase, the −CG occurrence rate increased smoothly with decreasing T_c, and declined with increasing T_c during the decay phase. By way of contrast, the +CG rate remained associated with approximately constant T_c (−69° and −72°C) during the growth phase, and then also declined with increasing T_c during the decay phase. The sprite-generating +CGs occurred in regions with cloudtop temperatures 2–3°C warmer than the rest of the +CG population. INDEX TERMS: 0320 Atmospheric Composition and Structure: Cloud physics and chemistry; 3324 Meteorology and Atmospheric Dynamics: Lightning; 3329 Meteorology and Atmospheric Dynamics: Mesoscale meteorology; 3360 Meteorology and Atmospheric Dynamics: Remote sensing. Citation: São Sabbas, F. T., and D. D. Sentman, Dynamical relationship of infrared cloudtop temperatures with occurrence rates of cloud-to-ground lightning and sprites, Geophys. Res. Lett., 30(5), 1236, doi:10.1029/2002GL015382, 2003.

1. Introduction

[2] Sprites are optical after-effects induced in the middle and upper atmospheres by lightning discharges, first documented in 1989 [Franz et al., 1990]. Boccippio et al. [1995] were the first to identify that a positive cloud-to-ground lightning (+CG) preceded ∼85% of the sprites using +CG signatures identified by the National Lightning Detection Network (NLDN) and/or "Q-bursts" signatures identified by ELF/VLF sensors. Subsequent observational studies have generally supported those results [Lyons, 1996, Cummer and Inan, 1997; Bell et al., 1998]. São Sabbas [1999], studying 746 sprite events from 7 days from the Sprites96 Campaign, found that only 65% of sprites were preceded by a +CG. About 11% were preceded by a −CG and 24% did not have any CG signature recorded by the NLDN. A detailed study of one of these days, 22 July, 1996, using NLDN and VLF data showed that this percentage could be increased to ∼75%, where the extra 10% would account for

+CGs that NLDN would not have registered [São Sabbas et al., 2003]. About 25% of events remained without preceding +CGs, suggesting that −CGs and intracloud discharges might also produce sprites, a possibility that is not ruled out by current theories [Pasko et al., 1997, 1998, and references therein].

[3] Although most sprite measurements have been performed in the central region of the US, sprites are global phenomena, as was first documented during the space shuttle Mesoscale Lightning Experiment (MLE) [Boeck et al., 1995]. Between 1989 and 1991, 17 sprites were recorded above thunderstorms over Australia, Africa, South Pacific and South America. Aircraft observations over Central and South America [Sentman et al., 1995], ground campaigns in Japan [Fukunishi et al., 2001] Australia [Dowden et al., 1996], more recent aircraft [Taylor et al., 2000] and ground-based observations [Neubert et al., 2001] over Europe and over Asia [Su et al., 2002] have confirmed these results.

[4] In the Midwest US, most sprite observations have been made between May–August, where Mesoscale Convective Complexes (MCC) are somewhat common occurrences [Lyons, 1996]. MCCs are a particular type of MCS. They are meteorological systems with strong convective activity, dimensions between 250 and 2500 km and duration greater than or equal to 6 hr (meso-α scale definition based upon physical characteristics observed in infrared (IR) satellite images [Maddox, 1980], cf. Table 1). MCCs are also common in oceanic and continental tropical regions, especially in the intertropical convergence zone (ITCZ), and over South America [Conforte, 1997]. In South America, the MCCs are, on average, about 60% larger in area and persist over longer intervals than similar systems in the US [Velasco and Fritsch, 1987], thus making this region the most active in the Western Hemisphere. Sprite observations over different regions of the globe, e.g., Peru [Sentman et al., 1995; Moudry et al., 1997], Europe [Neubert et al., 2001; Taylor et al., 2000], and Japan [Fukunishi et al., 2001], reveal that sprites can also be generated over small thunderstorms, suggesting that the type and size of thunderstorms that generate sprites may actually depend on local meteorology.

[5] In the present paper we investigate the cloud-top temperature characteristics of an intense sprite-producing thunderstorm system and the inter-relationships with associated lightning and sprite activity. The meteorological system is classified according to the Maddox [1980] definition. The analysis examines the occurrence rate and location of sprites and lightning with respect to the thunderstorm features and temporal development. The objective of the study is to create a methodology based on satellite

Table 1. MCC definition [adapted from *Maddox*, 1980]

Size	A - Contiguous Cloud shield with $T_{IR} \leq -32°C$, area $\geq 10^5$ km^2
	B - Interior clouds with $T_{IR} \leq -52°C$, area $\geq 5 \times 10^4$ km^2
Initiation	Size definitions A and B are first satisfied
Duration	Size definitions A and B must be met for a period ≥ 6 h
Max. extent	Cloud shield defined in A reaches maximum size
Shape	Eccentricity ≥ 0.7 at time of maximum extent
Termination	Size definitions A and B no longer satisfied

imagery that could be used in studies of global sprite production.

2. Data Set

[6] We used GOES-8 satellite 10–12 μm IR images over the period 0015–1545 UT containing the meteorological system over Kansas that produced the sprites observed on the night of July 22, 1996. Forty events from the set of sprites observed on this night have previously been studied in a detailed report presented by *São Sabbas et al.* [2003]. The sprite positions were triangulated (see *São Sabbas et al.* [2003] for details) and the lightning information used here was provided by the NLDN.

[7] The GOES-8 data were provided by the National Climatic Data Center (NCDC), Asheville, North Carolina. The 10 bit/pixel images had a spatial resolution of approximately 4 km, temperature resolution 0.1 K, and were spaced at 30 min intervals. We isolated the part of the image corresponding to the sprite-producing MCC and environs (Figure 1a) and remapped it to an isometric latitude and longitude grid. The count values were converted to cloudtop temperature (T_c) using the procedures of *Weinreb et al.* [2001]. Figure 1b shows the resulting color-coded temperature map as a function of latitude and longitude (lat/lon) for 0615 UT. On these maps were also plotted the location of +/−CGs detected by the NLDN and triangulated locations of sprites that occurred within +/−15 min of the image, e.g., from 0600–0630 UT in Figure 1.

3. Analysis

[8] We matched the lat/lon of the lightning and triangulated positions of sprites to the lat/lon matrices of the images and identified the pixels with the temperatures of the correspondent cloudtop region. For each image we assembled histograms of lightning flashes and sprites versus temperature. Comparing the histograms with the T_c maps, we find that as the storm grows, compact regions of very cold cloudtops develop and the lightning discharges, −CGs more than +CGs, have the tendency to concentrate on those regions. Not all regions with very cold cloudtops exhibited lightning activity, even though cold cloudtops are strong evidence of vigorous convection. Generally, we expect that charge separation, hence lightning, follows convection, leading to an intensification of the lightning activity associated with cold cloudtops.

[9] The histograms were combined into temperature-time spectrograms (Figure 2) that reveal the evolution of T_c associated with lightning and sprites over the lifetime of the storm. There is some smearing in the histograms from samples obtained near sharp temperature gradients, due to the thunderstorm movement northeastward at a rate of

several tens of km between the 30 min image intervals. This motion corresponded to several pixels in the IR images, but the overall effect is minor.

[10] Figure 2a shows that, throughout the lifetime of the thunderstorm, the −CG occurrence rate increases in association with decreasing T_c during the growing phase, reaches a maximum associated with the coldest T_c ($-72°C \leq T_c \leq -69°C$) that lasts for ~2 h, and then decreases in association with increasing T_c during the decay phase of the storm. The +CG rate (Figure 2b) remains associated with approximately constant T_c ($-72°C \leq T_c \leq -69°C$) during the growth of the thunderstorm and also decreases with increasing T_c during the decay phase. The +CGs produced during the growth phase occur in association with the same T_c range that −CGs are associated with during the −CGs maximum production.

[11] The sprite observation period was 0323–0856 UT, and sprites were recorded from 0428 UT to 0829 UT. Figure 2c shows that during the period of most intense sprite activity, between 0545 UT and 0615 UT, sprites concentrated over regions with $T_c \geq -70°C$, in particular $-65°C \leq T_c \leq$
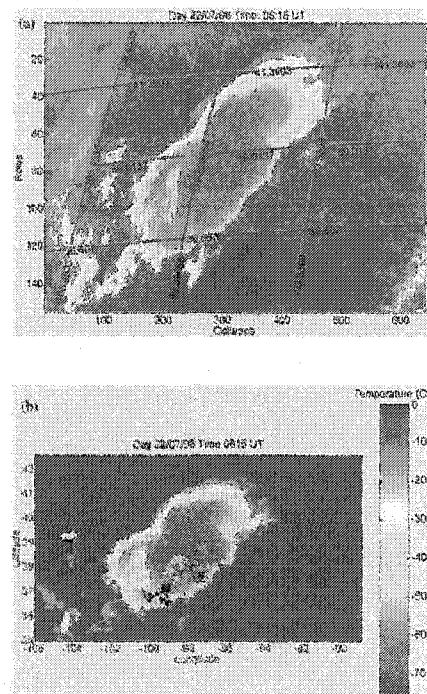

Figure 1. Images of the sprite producing thunderstorm of 22 July, 1996, observed by the GOES-8 satellite at 0615 UT. Panel (a) is the raw data utilized, i.e., the satellite view. Panel (b) is a cloudtop temperature map (T_c) as a function of latitude and longitude. The map also show the location of +CGs (pink crosses), −CGs (black dots), sprites (green circles), +CGs associated with sprites (white circles), and −CGs associated with sprites (white squares). The CGs and sprites occurred within ±15 min of the image time. A similar map showing the association of lightning with cloudtop temperatures have been previously presented by *Lyons et al.* [2000].
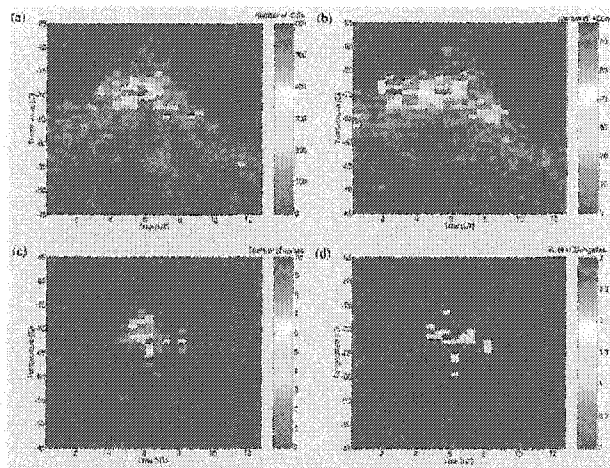
Figure 2. Temporal development of the relationship between GOES-8 IR cloudtop temperatures and the occurrence rate of lightning and sprites throughout the lifetime of the thunderstorm. Each pixel covers 30 min by 1°C, so that each column is the histogram of occurrences vs temperature. The thunderstorm growth phase is 0015–0545 UT. Panel (a) is for −CGs, (b) is for +CGs, (c) is for sprites, and (d) is for sprite producing +CGs.

−63°C (0615 UT). The peak in sprite activity occurred during the period when the −CGs occurrence rate reached a maximum associated with minimum T_c. Even though sprites are predominantly generated by +CGs [*Boccippio et al.*, 1995; *Lyons*, 1996, *Cummer and Inan*, 1997; *Bell et al.*, 1998; *São Sabbas et al.*, 2003], this result shows that the total −CG activity is more tightly correlated with sprite activity than has previously been reported. Whether the total −CG activity plays a role in determining the sprite occurrence rate, or this result reflects a particular characteristic of the specific thunderstorm studied, is presently unknown.

[12] The rate of occurrence of sprite generating +CGs remains associated with approximately constant T_c (Figure 2d), following the behavior of the total +CGs rate (Figure 2b). The difference is that the distribution of the sprite-generating +CGs (2d) is centered between −67° and −69°C, about 2–3°C warmer than for +CGs taken as a whole (2b). The bulk of +CGs of the storm tend to occur in the strong convective regions associated with the coldest cloudtop temperatures, while sprite producing lightning tend to occur in warmer stratiform regions.

[13] The development of the thunderstorm area is shown in the last row of Figure 3 together with the sprite, +CG, −CG and total +/−CG occurrence rates during the lifetime of the thunderstorm. The sprite producing storm is "born" between 0045 and 0115 UT, as a result of the coalescence of two relatively small thunder cells (not shown). At 0115 UT it satisfies Maddox's initiation criteria for MCCs (*cf*. Table 1). The storm grows until 0545 UT when the contiguous cloud-top region with $T \leq -52°C$ reaches the maximum area of $\sim 1.4 \times 10^5$ km², after which the storm starts to decay, even as the total area of the thunderstorm, as defined by the warmer $T_c \leq -32°C$, continues to expand. The maximum extent of the storm $\sim 2.32 \times 10^5$ km² is reached at 0745 UT. The eccentricity of the storm at this point is less than 0.7, so this MCS cannot be classified as an MCC according to the Maddox criteria. The MCS terminates at 1015 UT.

[14] The ~ 9 hr lifetime of the system studied here is lower than the 14.3 hr mean MCCs duration reported by *Goodman and MacGorman* [1986] in a study of 10 MCCs over the Midwest US. During these ~ 9 hr a total of 40,605 cloud-to-ground flashes were produced, of which 10.9% (4,412) were +CGs and 89.1% (36,193) were −CGs. The average flash rate 75.2 min^{-1} was more than 2 times greater than the maximum 32.7 min^{-1} average flash rate reported by *Goodman and MacGorman* [1986].

[15] Figure 3 shows that the maximum production of sprites, from 0545 UT to 0615 UT, occurs at the time of maximum area of the region of $T \leq -52°C$, spanning the transition from growth to decay phases of the MCS. The same behavior also occurs for the −CG (third row) and total (+/−) CG (fourth row) occurrence rates. The +CG rate
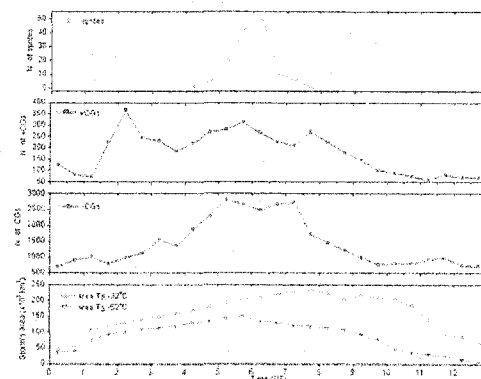

Figure 3. Temporal development of sprite rate (first row), +CG rate (second row), −CG rate (third row) and contiguous area of cloud cover with $T_c \leq -32°C$ and $T_c \leq -52°C$ during the thunderstorm lifetime.

(second row) remains high (>170 flashes/30 min) and exhibits a relative maximum during this period, but its absolute maximum occurs at 0215 UT, approximately 1 hr after merging of the two cells that initiated the MCS. The total +/−CG occurrence rate peaks ~2hr before maximum extent, agreeing with the 2.6 hr reported by *Goodman and MacGorman* [1986]. By the time of maximum extent of the storm (cf. Table 1) the total +/−CG occurrence rate starts to decrease. *Goodman and MacGorman* [1986] suggest that this occurs because the convective precipitation regions are replaced by widespread stratiform precipitation.

4. Summary of Results

[16] The sprite producing system over Kansas on 22 July 1996 was an MCS that originated from the merging of two thunderstorm cells between 0045 UT and 0115 UT. The total lifetime of the system was ~9h. The MCS moved northeastward and reached a maximum extent of ~2.3 × 10^5 km^2 at 0745 UT, approximately 6 hr after its initiation. The maximum sprite and −CG production of the system were simultaneously achieved at the time of maximum contiguous cloud cover of the coldest region with $T_c \leq -52°C$, ~ 2 hr before the system reached its maximum extent. The −CG rate increased during the growth phase of the thunderstorm in association with decreasing T_c, it reached a maximum associated with the coldest T_c ($-72°C \leq T_c \leq -69°C$), and then, in the decay phase of the MCS, it decreased in association with increasing T_c. We suggest that the total −CG activity and dynamical development of the thunderstorm may be more tightly correlated with sprite activity than has previously been reported. The +CG rate remained high during the sprite-recording period, and remained associated with approximately constant T_c ($-72°C \leq T_c \leq -69°C$, same as −CGs) while the system was growing, subsequently decreasing with increasing T_c during the decay phase. Sprite-generating +CGs occurred in regions about 2–3°C warmer than the bulk population of +CGs.

[17] The techniques reported here to correlate sprite occurrence with the spatial and temporal topology of cloud-top temperatures are the initial steps towards developing a robust methodology based on satellite imagery that could be used to study sprite-generating thunderstorms wherever they might occur in the world. The present analysis was for a single storm. To be most useful and to bound the variance of the results, additional studies would need to be made across many thunderstorms and a variety of latitudes, longitudes and seasons. Candidate regions and satellites suitable for such studies include South America (GOES-8; *Velasco and Fritsch* [1987]), equatorial and Southern mid-latitude Africa (Meteosat-7; *Fuellekrug* [2001]) South-, Southeast Asia, and the Malay Archipelago (GMS-5 and InSat; *Sentman and São Sabbas* [2001]).

References

Bell, T. F., S. J. Reising, and U. S. Inan, Intense continuing currents following positive cloud-to-ground lightning associated with red sprites. *Geophys. Res., Lett.*, 25, 1285–1288, 1998.

Boccippio, K. J., E. R. Williams, S. J. Heckman, W. A. Lyons, I. T. Baker, and R. Boldi, Sprites, ELF transients, and positive ground strokes, *Science*, 269, 1088, 1995.

Boeck, W. L., O. H. Vaughan, R. J. Blakeslee, B. Vonnegut, M. Brook, and J. McKune, Observations of lightning in the stratosphere, *J. Geophys. Res.*, 100, 1465, 1995.

Conforte, J. C., "A study of Mesoscale Convective Complexes over South America and Neighboorood" (in Portuguese), Ph.D. Dissertation, National Institute of Space Research (INPE), S. J. dos Campos, Brazil, 1997.

Cummer, S. A., and U. S. Inan, Measurements of charge transfer in Sprite-producing lightning using ELF radio atmospherics, *Geophys. Res., Lett.*, 24, 1731–1734, 1997.

Dowden, R. L., J. B. Brundell, W. A. Lyons, and T. Nelson, Detection and location of sprites by VLF phase scattering of subionospheric transmissions, *Geophys. Res. Let.*, 23, 1741–1744, 1996.

Franz, R. C., R. J. Nemzek, and J. R. Winckler, Television image of a large upward electrical discharge above a thunderstorm system, *Science*, 249, 48–51, 1990.

Fuellekrug, M., Estimation of sprite occurrence densities in central Africa by infrared satellite imagery, *Proceedings of IAGA-IASEI Joint Scientific Assembly*, Hanoi, Vietnam, p. 99, Aug. 2001.

Fukunishi, H., Y. Takahashi, T. Adachi and R. Miyasato, Characteristics of sprites and Elves observed in winter above Japan, *Proceedings of IAGA-IASEI Joint Scientific Assembly*, Hanoi, Vietnam, p. 98, Aug. 2001.

Goodman, S. J., and D. R. MacGorman, Cloud-to-Ground Lightning Activity in Mesoscale Convective Complexes, *Monthly Weather Review*, 114, 2320, 1986.

Lyons, W. A., Sprite observations above the U. S. High Plains in relation to their parent thunderstorm systems, *J. Geophys. Res.*, 101, 29,641, 1996.

Lyons, W. A., R. A. Armstrong, E. R. Williams, and E. A. Bering, The Hundred Year Hunt for the Sprite, *EOS, Trans. AGU.*, 81(33), 373–377, 2000.

Maddox, R. A., Mesoscale convective complexes, *Bull. Am. Meteorol. Soc.*, 61, 1374–1387, Nov. 1980.

Moudry, D. R., M. J. Heavner, D. D. Sentman, and E. M. Wescott, Sprites over small storms, *EOS Trans. Am. Geophys. Union*, 78(46), F83, 1997.

Neubert, T., T. H. Allin, H. Stenbaek-Nielsen, and E. Blanc, Sprites over Europe, *J. Geophys. Res. Lett.*, 28, 3585, 2001.

Pasko, V. P., U. S. Inan, and T. F. Bell, Sprites produced by Quasi-electrostatic heating and ionization in the lower ionosphere", *J. Geophys. Res.*, 102, 4529, 1997.

Pasko, V. P., U. S. Inan, T. F. Bell, and Y. N. Taranenko, Spatial structure of sprites, *Geophys. Res. Lett.*, 25, 2123–2126, 1998.

São Sabbas, F. T., D. D. Sentman, E. M. Wescott, O. Pinto Júnior, O. Mendes Júnior, and M. J. Taylor, Statistical analysis of space-time relationships between sprites and lightning, *J. Atmos. Solar-Terr. Phys.*, in press, 2003.

São Sabbas, F. T., "Estudo da relação entre Sprites e os relâmpagos das tempestades associadas" (Study of the relationship between Sprites and lightning from the associated storms). *Master dissertation, Instituto Nacional de Pesquisas Espaciais (INPE)*, São José dos Campos, SP, Brazil, Feb. 1999.

Sentman, D. D., and F. T. São Sabbas, Comparison of South American and African diurnal signatures in the Schuman resonances with satellite infrared Images", *Proceedings of Vietnam 2001 IAGA-IASPEI Joint Scientific Assembly*, paper G2.01[2624], p. 100, Hanoi, Vietnam, August, 2001.

Sentman, D. D., E. M. Wescott, D. L. Osborne, M. J. Heavner, and D. L. Hampton, The Peru95 Sprites Campaign: Overview, *EOS Trans. AGU*, May 1995.

Su, H. T., R. R. Hsu, A. B. Chen, Y. J. Lee, and L. C. Lee, Observations of sprites over the Asian continent and over oceans around Taiwan, *Geophys. Res. Lett.*, 29, 1–4, 2002.

Taylor, M. J., L. C. Gardner, and C. Siefring, Image measurements during the 1999 Leonids-MAC Airborne Campaign: High-resolution meteor ablation signatures and longitudinal gravity wave study", *2nd Leonids-MAC workshop*, Tel Aviv, April, 2000.

Velasco, I., and J. M. Fritsch, Mesoscale convective complexes in the Americas, *J. Geophys. Res.*, 92, 9591, 1987.

Weinreb, M. P., J. X. Johnson and D. Han, "Conversion of GVAR Infrared Data to Scene Radiance or Temperature", *NOAA NESDIS Office of Satellite Operations*, Boulder, Colorado, Revised, June 2001.

—————————————

D. D. Sentman and F. T. São Sabbas, Geophysical Institute, University of Alaska Fairbanks, Fairbanks, AK 99775-7320, USA. (fssabbas@gi.alaska. edu)